PERSISTENT SCATTERER RADAR INTERFEROMETRY FOR CRUSTAL DEFORMATION STUDIES AND MODELING OF VOLCANIC DEFORMATION

A DISSERTATION
SUBMITTED TO THE DEPARTMENT OF GEOPHYSICS
AND THE COMMITTEE ON GRADUATE STUDIES
OF STANFORD UNIVERSITY
IN PARTIAL FULFILLMENT OF THE REQUIREMENTS
FOR THE DEGREE OF
DOCTOR OF PHILOSOPHY

Andrew John Hooper
May 2006

I certify that I have read this dissertation and that, in my opinion, it is fully adequate in scope and quality as a dissertation for the degree of Doctor of Philosophy.

Paul Segall
(Principal Co-Adviser)

I certify that I have read this dissertation and that, in my opinion, it is fully adequate in scope and quality as a dissertation for the degree of Doctor of Philosophy.

Howard Zebker
(Principal Co-Adviser)

I certify that I have read this dissertation and that, in my opinion, it is fully adequate in scope and quality as a dissertation for the degree of Doctor of Philosophy.

Antony Fraser-Smith

Approved for the University Committee on Graduate Studies.

Abstract

While conventional interferometric synthetic aperture radar (InSAR) is a very effective technique for measuring crustal deformation, almost any interferogram includes large areas where the signals decorrelate and no measurement is possible. Consequently, most InSAR studies to date have focused on areas that are dry and sparsely vegetated. A relatively new analysis technique, permanent scatterer InSAR, overcomes the decorrelation problem by identifying resolution elements whose echo is dominated by a single scatterer in a series of interferograms. This technique has been useful for analysis of urban areas, where angular structures produce efficient reflectors that dominate background scattering. However, man-made structures are absent from most of the Earth's surface. Furthermore, this technique requires, *a priori*, an approximate temporal model for the deformation, whereas characterizing the temporal pattern of deformation is commonly one of the aims of any study.

We have developed a new method of analysis, StaMPS, using spatial correlation of interferogram phase to find a network of stable pixels in all terrains, with or without buildings. Prior knowledge of temporal variations in the deformation rate is not required. We refer to these pixels as persistent scatterers (PS). A key component of our method is the development of two algorithms to unwrap a three-dimensional series of interferograms. We observe temporally-variable deformation, using an initial version of StaMPS, in data acquired over Long Valley caldera in California, for a period when deformation rates varied significantly. The inferred displacements of the PS compare well with ground truth. Using an enhanced version of StaMPS, we detect a period of steady deflation within the Volcán Alcedo caldera in the Galápagos Islands between 1997 and 2001, which we model with a contracting ellipsoidal magma

body. Conventional InSAR has been limited here until now by high rates of temporal decorrelation over much of the volcano. We also detect motion along the inner slopes of the caldera which we interpret as landsliding.

Finally, we analyze geodetic data spanning the 1989 Kilauea south flank earthquake, Hawaii, and find that the depth of the inferred fault plane is consistent with the hypocentral depth, which was previously not clear.

Acknowledgments

First and foremost I would like to thank my advisors, Paul Segall and Howard Zebker, whose advice and mentorship has been tireless, fair and of the highest standard. I am also grateful to Tony Fraser-Smith, Chuck Wicks and George Hilley for useful advice during review meetings and constructive comments that improved this thesis.

Thanks also go to the many colleagues that I have worked with, in particular to office mates Emily Desmarais and Kaj Johnson for their good humor and Sang-Ho Yun for always being on call to answer questions. Other colleagues who have contributed to my education are current and former members of the crustal deformation group, Kyle Anderson, Maurizio Battaglia, Peter Cervelli, Gwyneth Hughes, Pascual Lacroix, Anne Loevenbruck, Zhen Lu, Dörte Mann, Shinichi Miyazaki, Jessica Murray, Ryu Otani and Dan Sinnet, and current and former members of the radar group, Piyush Shanker Agram, Noa Bechor, Leif Harcke, Jörn Hoffman, Sjonni Jónsson, Fayaz Onn, Ana Bertrán Ortiz, Shadi Oveisgharan and Lauren Wye. I am also grateful to colleagues at the German Aerospace Center (DLR) in Oberpfaffenhofen, where I spent two stints of time during my Ph.D., in particular to Bert Kampes for many helpful discussions, and also to Nico Adam and Michael Eineder.

Other members and former members of the Geophysics department who have made my time at Stanford enjoyable are Brad Artman, Naomi Boness, Laura Chiaramonte, Eric Hand, Justin Rubinstein, Dave Shelly and in particular Al Tagliabue with whom I have spent many a long lunch solving the World's problems.

Finally, I thank my parents, Pete and Liz Hooper, for their early guidance and later encouragement, and above all I am grateful to my wife, Julia, who put her own career in medicine on hold to move to California with me, and has been my constant

support.

Radar data used in this thesis were provided by the European Space Agency and MacDonald, Dettwiler and Associates Ltd. Deformation and topographic data were provided by the U. S. Geological Survey and SRTM topographic data were provided by the Jet Propulsion Laboratory (JPL). Focused SAR images were formed using the ROI_PAC software package developed by JPL. Interferometric processing was performed using the Doris software package developed by the Delft Institute for Earth-Oriented Space Research (DEOS), Delft University of Technology. DLR proprietary software was also used for SAR focusing and interferometric processing. I thank Mark Simons and Mike Poland for making data available, and Thóra Árnadóttir, Valerie Cayol, Paul Vincent and Tim Wright for helpful reviews of associated manuscripts. Funding for this research was provided by the Robert and Marvel Kirby Stanford Graduate Fellowship, the Stanford University Geophysics Department and the National Science Foundation through grants EAR-9902875, EAR-0309425 and EAR-0511035.

Contents

List of Tables

List of Figures

List of Abbreviations

1-D	one-dimensional
2-D	two-dimensional
3-D	three-dimensional
DEM	digital elevation model
DLR	German Aerospace Center
EDM	electronic distance meter
Envisat	European Space Agency environmental satellite
ERS-1	European Space Agency Earth remote sensing satellite 1
ERS-2	European Space Agency Earth remote sensing satellite 2
ESA	European Space Agency
FFT	fast Fourier transform
GPS	global positioning system
InSAR	interferometric Synthetic aperture radar
JPL	Jet Propulsion Laboratory
LAMBDA	least-squares ambiguity decorrelation method
LOS	line-of-sight
NASA	National Aeronautics and Space Administration
NP-Hard	non-deterministic polynomial-time hard, relating to problem complexity
PDF	probability density function
PS	persistent scatterer
Radarsat-1	Canadian synthetic aperture radar satellite 1
SAR	synthetic aperture radar
SEASAT	NASA remote sensing satellite

SNR	signal to noise ratio
SRTM	shuttle radar topography mission
StaMPS	Stanford method for persistent scatterers
UTC	coordinated universal time

List of Symbols

A	SAR amplitude
B	interferometer baseline
$B_\perp$	perpendicular component of interferometer baseline
$B_\perp^c$	critical perpendicular component of interferometer baseline
$D_\mathcal{A}$	amplitude dispersion index
e	base of the natural logarithm
F_{DC}	doppler centroid baseline
F_{DC}^c	critical doppler centroid baseline
g_x	signal amplitude
$G(x, y)$	combined low-pass adaptive phase filter response
$H(x, y)$	adaptive phase filter response
j	$\sqrt{-1}$
$K_{\varepsilon,x}$	a constant relating $B_{\perp,x,i}$ to $\Delta\phi_{\varepsilon,x,i}$
$L(x, y)$	5th order Butterworth low-pass filter response
$\mathcal{L}^T$	low-pass filter operator
N	number of interferograms
$n_{R,x,i}$	real component of noise
$n_{I,x,i}$	imaginary component of noise
p_{max}	maximum probability density
$p(\gamma_x)$	probability density function of γ_x for all pixels
$p_{PS}(\gamma_x)$	probability density function of γ_x for PS pixels
$p_R(\gamma_x)$	probability density function of γ_x for random phase pixels
q	allowable fraction of selected pixels that are not PS

r	range distance
T	temporal baseline
T^c	critical temporal baseline
v	sensor velocity
$W\{\cdot\}$	wrapping operator that converts values to modulo 2π
$Z(x, y)$	smoothed intensity of 2-D FFT
α	a weighting parameter
β	a weighting parameter
γ_x	measure of phase noise variability based on coherence
γ^{thresh}	threshold value for γ_x
$\delta_{x,i}$	sum of residual spatially uncorrelated terms
$\delta'_{x,i}$	δ plus residual spatially uncorrelated phase due to look angle error
Δh	error in height above the reference surface
Δr	difference in range distance between "master" and "slave" geometry
$\Delta\theta_x$	error in look angle
$\Delta\theta_x^{nc}$	spatially uncorrelated error in look angle
$\Delta\phi_{\varepsilon,x,i}$	residual component of unwrapped phase due to DEM error
$\Delta\phi_{orb,x,i}$	residual component of unwrapped phase due to orbit error
$\Delta\phi_{\theta,x,i}$	residual component of unwrapped phase due to look angle error
$\Delta_{x_1}^{x_2}$	differencing operator giving value at x_2 minus value at x_1
η	distance of phase center from pixel center in azimuth direction
θ	SAR look angle with respect to nadir
θ_i	local incidence angle
κ	a constant relating $D_{\mathcal{A}}$ to γ^{thresh}
λ	SAR signal wavelength
μ_A	mean amplitude value
ξ	horizontal distance of phase center from pixel center in range direction
π	ratio of a circle's circumference to its diameter

ρ	correlation
σ_A	standard deviation of amplitude values
σ_n	standard deviation of real and imaginary components of noise
σ_ϕ	standard deviation of phase
$\phi_{int,x,i}$	interferometric unwrapped phase for pixel x in interferogram i
$\phi_{atm,x,i}$	atmospheric component of unwrapped phase
$\phi_{def,x,i}$	deformation component of unwrapped phase
$\phi_{n,x,i}$	noise component of unwrapped phase
$\phi_{uw,x,i}$	unwrapped phase $W^{-1}\{W\{\psi_{int} - \Delta\widehat{\phi}_\theta^{nc} - \widehat{\phi}^{m,nc}\}\}$
ϕ^{corr}	spatially correlated phase
ϕ^m	"master" contribution to the phase
ϕ^{nc}	spatially uncorrelated phase
ϕ^s	"slave" contribution to the phase
$\phi'_{n,x,i}$	$\phi_{n,x,i}$ plus residual spatially uncorrelated terms
ϕ_θ	phase dependent on look angle
$\psi_{int,x,i}$	wrapped interferometric phase
$\widetilde{\psi}_{int}$	filtered wrapped interferometric phase
ω	angle between interferometer baseline and horizontal

Chapter 1

Introduction

Reality is merely an illusion, albeit a very persistent one.

ALBERT EINSTEIN

Measurements of crustal deformation have contributed greatly to our understanding of tectonics, earthquakes, volcanism and landslides. Surface deformation measurements are routinely used to constrain the subsurface geometry of active faults and the spatial distribution of coseismic slip. Even more importantly, these data provide our primary means for recording aseismic processes such as afterslip, viscoelastic and poroelastic adjustments and so-called silent earthquakes. Geodetic measurements provide invaluable constraints on the interseismic accumulation of strain that will ultimately be released in large and damaging earthquakes. Most volcanic eruptions are preceded by inflationary doming and stretching of the crust as large volumes of magma migrate from the mantle through the crust. Deformation measurements also play an important role in quantifying the kinematics of active landslides.

Despite the tremendous advances in both the global positioning system (GPS) and interferometric synthetic aperture radar (InSAR) during the last decade, a major limitation in our ability to model these and other crustal processes is the lack of deformation data in many areas. While conventional InSAR is a proven, very effective technique for measuring deformation, almost any interferogram includes large areas where the signals decorrelate and no measurement is possible. Where measurement is possible, overprinting of the deformation signal with signal due to variation in

atmospheric properties is a further issue.

A relatively recent analysis technique, persistent scatterer (PS) InSAR, addresses both the decorrelation and atmospheric problems of conventional InSAR. However, implementations up to now have been limited to applications where there are many bright scatterers, which are usually man-made structures, and where displacement rates vary in a presupposed manner, which is usually assumed to be steady-state or sinusoidal.

We describe in this dissertation a new persistent scatterer analysis method we have developed, known as StaMPS (Stanford Method for Persistent Scatterers), that identifies and extracts the deformation signal even in the abscence of bright scatterers. StaMPS is also applicable in areas undergoing non-steady deformation, with no prior knowledge of the variations in deformation rate. First we present the application of an early version of StaMPS to data acquired over Long Valley volcanic caldera, in order to validate the method against conventional InSAR and ground truth. We then present an improved version of StaMPS as applied to Volcán Alcedo in the Galápagos Archipelago. This volcano is known to be actively deforming from conventional InSAR, but because of decorrelation on the volcano's flanks, it has not been possible until now to constrain the magnitude and spatial pattern of the deformation signal in these areas and the caldera itself. Using StaMPS we detect and quantify a deflationary signal within the caldera. We model the source of this deformation as a deflating ellipsoidal magma body beneath the caldera, accompanied by landsliding on the inner slopes of the caldera. We also analyze deformation on another volcano, Kilauea, located on the Big Island of Hawaii. Specifically we examine deformation associated with an earthquake that occurred on the south flank in 1989. This event predates the regular acquisition of SAR data over Kilauea, hence we use other geodetic data to constrain details of the faulting and rheological structure of the volcano.

1.1 Contributions

There are two main focuses of this dissertation. First, we describe a new persistent scatterer method (StaMPS) that improves our ability to image deformation of

the surface of the Earth using spaceborne radar interferometry. Second, we use displacements measured on volcanoes from StaMPS and other geodetic techniques to learn more about the sources of deformation, in order to answer more fundamental questions about the underlying physical processes. Below we summarize the main contributions of this work:

1. We design and implement a new algorithm to coregister multiple images to one "master" image, including image pairs with very low coherence.

2. We design and implement a new algorithm to identify persistent scatterer pixels in a series of interferograms with or without the presence of man-made structures.

3. We design and implement a new algorithm to identify persistent scatterer pixels in a series of interferograms with no assumed model for how displacement rates vary with time.

4. We develop a framework for approaching the problem of three-dimensional phase unwrapping.

5. We design and implement two algorithms for unwrapping three-dimensional phase data, which are applicable to InSAR time series.

6. We find that the shallow magma chamber geometry beneath Volcán Alcedo is elongate, unlike those previously inferred for other active volcanoes in the Galápagos Archipelago, and is likely undergoing crystallization.

7. We find that there are slow moving landslides on the inner caldera walls of Volcán Alcedo.

8. We find that there is no discrepancy, as has been suggested, between the depth of rupture associated with the 1989 M6.1 Kilauea south flank earthquake determined from geodetic and seismic data.

1.2 Thesis Roadmap

Chapters 3 to 6 of this thesis are written as independent studies based on manuscripts that have already been published in scientific journals, or are in preparation for submission to journals. It is therefore possible to read each chapter independently without the necessity of reading any previous chapters first. For each associated manuscript there are multiple authors, however, the author of this dissertation is the primary researcher and author in each case.

Chapter 2 provides a brief overview of InSAR and existing persistent scatterer InSAR methods.

Chapter 3 is primarily concerned with the development of a new InSAR technique which isolates and extracts the deformation signal from persistent scatterer pixels. We apply the method to data from Long Valley caldera as a test site, and validate the technique by comparing results with both conventional InSAR and ground truth measurements. This chapter is based on material published in *Geophysical Research Letters* in 2004 [*Hooper et al.*, 2004].

Chapter 4 describes an improved version of our persistent scatterer method that can be applied more generally for imaging deformation. We then apply the method to Volcán Alcedo, an actively deforming volcano in the Galápagos Archipelago for which there are no geodetic data other than SAR data. Using both ascending and descending orbit data we map subsidence of the caldera for the period between October 1997 and January 2001. We model this deformation as due to a deflating ellipsoidal magma body, accompanied by landsliding on the inner slopes of the caldera. This chapter will be submitted to the *Journal of Geophysical Research*.

Chapter 5 describes two methods for phase unwrapping, that is, recovering unambiguous phase values from three-dimensional phase data that are known only in modulo 2π radians. This is an important step in our persistent scatterer method, and treating the problem in three dimensions rather than two greatly improves the accuracy of the method. This chapter represents the first publication of a three-dimensional phase unwrapping algorithm that can be applied to InSAR data and will be submitted to the *Journal of the Optical Society of America*.

Chapter 6 is concerned only with the application of other geodetic measurement techniques and not the persistent scatterer method. We reanalyze the 1989 M6.1 earthquake that occured on the south flank of Kilauea volcano in Hawaii, using all the available geodetic data. We also use seismic data to compare and further constrain our models. This chapter was published in *Geophysical Research Letters* in 2002 [*Hooper et al.*, 2002].

Chapter 7 provides a summary of the thesis and suggestions for future work.

Chapter 2

Background

Persistent scatterer radar interferometry is an extension of conventional synthetic aperture radar interferometry (InSAR). In this chapter we review the fundamental principles of InSAR and discuss some of the shortcomings. We then review other persistent scatterer methods and also discuss their limitations.

2.1 Synthetic Aperture Radar Interferometry

Synthetic Aperture Radar (SAR) is an extension of classical radar techniques developed in the first half of the 20th century. Pulse compression techniques and the synthetic aperture concept enable spatial resolutions on the order of meters with relatively small physical antennas. Spaceborne SAR instruments were initially used for the investigation of planetary surfaces with the first Earth orbiting SAR instrument not launched until 1978, aboard the NASA SEASAT satellite. The principle of using spaceborne SARs as interferometers dates to early 1970s [*Richman*, 1971; *Zisk*, 1972] and the first terrestrial InSAR applications were in the late 1980's [e.g., *Zebker and Goldstein*, 1986; *Goldstein and Zebker*, 1987]. However, it was the launch of the ESA satellite ERS-1 in 1991, leading to a large amount of SAR data suitable for InSAR becoming available, that made InSAR widely applicable.

SAR systems operate with a side-looking geometry and illuminate the Earth with a series of microwave pulses. As the spacecraft moves, the illuminated footprint sweeps

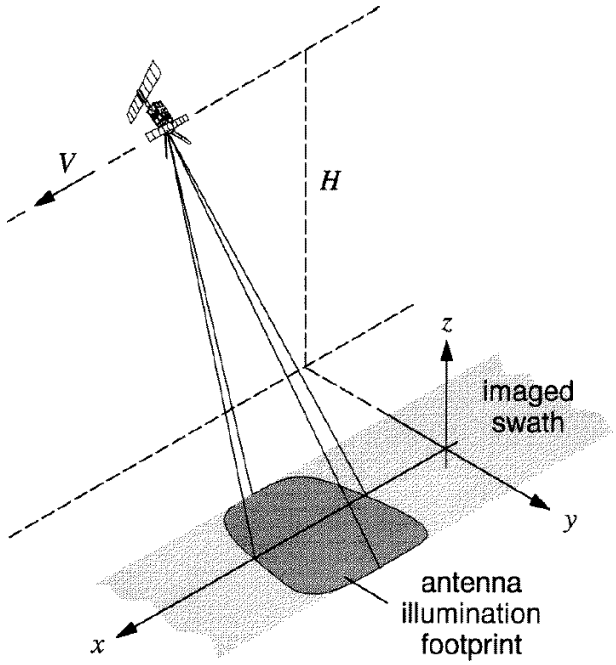

Figure 2-1: SAR Imaging geometry from *Bamler and Hartl* [1998]. Frequently used terms are "along-track" or "azimuth" for x, "ground range" for y and "slant range" for the distance of a particular point from the SAR sensor.

out a swath in the direction of movement (Figure 2-1). Interspersed with pulse transmission, the SAR detects echoes of previous pulses, scattered from the Earth. The raw data collected by the SAR is then focused to form an image. This is achieved in the direction perpendicular to the flight direction (range) through knowledge of the time delay, and in the flight direction (azimuth) through combination of echoes from multiple locations to synthesize a large antenna aperture. In range direction, bandwidth is provided by the nature of the pulse, whereas in azimuth direction, bandwidth is provided by the variation in frequency due to the Doppler effect associated with the movement of the sensor relative to the Earth. There are various algorithms and implementations to carry out image processing, a review of which is provided by *Bamler and Hartl* [1998].

At full resolution, the value for each pixel in the image is related to the scattering properties of a resolvable patch of the Earth. Specifically it is the coherent sum of the echoes from all the individual scatterers within the patch convolved with a

low-pass impulse response function. Each pixel value has both amplitude and phase. Because echoes can add both constructively and destructively, the amplitude values over the image fluctuate around the nominal values for each pixel based on its radar brightness, which is known as the "speckle effect". Pixel phase values for a single image are generally not useful.

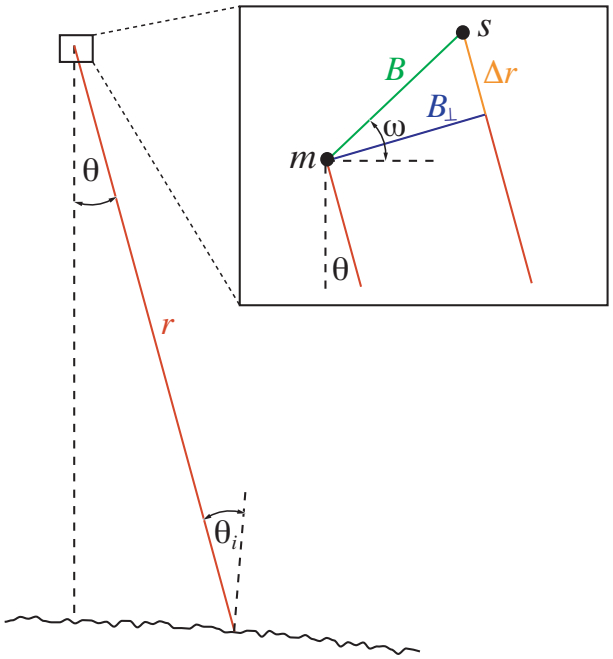

Figure 2-2: Imaging geometry for satellite radar interferometry. The sensor is moving into the plane of the paper, its position at the time of the "master" acquisition marked by m, and at the time of the "slave" acquisition by s. B is the length of the baseline between the sensor positions at the two times, $B_\perp$ refers to the perpendicular component of the baseline, r is the range from the sensor to the Earth's surface, ω is the angle between the baseline vector and the horizontal, θ is the look angle and θ_i is the angle of incidence at the Earth's surface.

If a second image is acquired over the same area, either by a different sensor with similar specifications, or the same sensor at a different time, it can be "interfered" with the first image, which entails simply multiplying by the complex conjugate. Generally, the second image is acquired from a slightly different position so it is first resampled to the same geometrical framework as the first image. The phase of the resulting interferogram is the difference in phase between the two images. Ignoring

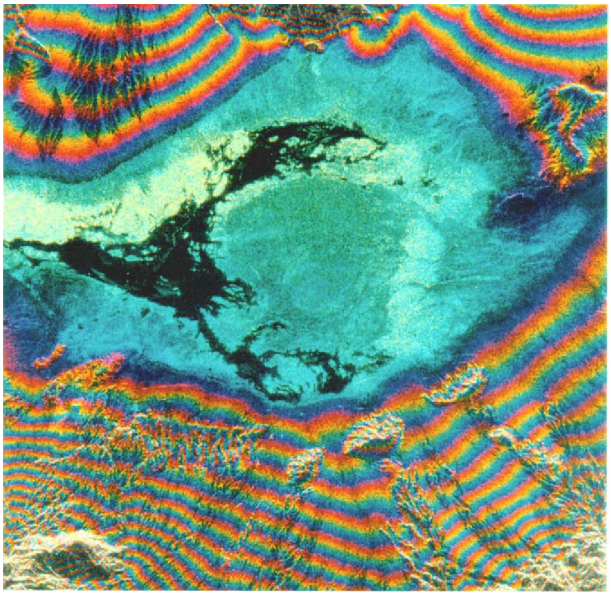

Figure 2-3: Interferogram of Cotton Ball basin, Death Valley [*Li and Goldstein*, 1990]. The color represents the interferogram phase, which is known only modulo 2π and varies with topography. Each color fringe represents approximately 24 m of elevation. The brightness represents the interferogram magnitude.

for now decorrelation effects and any difference in wave propagation speed through the atmosphere, the difference in phase depends only on the change in path length, Δr (Figure 2-2),

$$\phi = -\frac{4\pi}{\lambda}\,\Delta r. \tag{2.1}$$

The minus sign comes in because ϕ is defined as the phase delay, which decreases as Δr increases. If there is no deformation of the Earth's surface between the two acquisitions, Δr depends only on the geometry and it can be shown that

$$\phi \approx \frac{4\pi}{\lambda} B \left(\sqrt{1 - \frac{z^2}{r^2}}\; cos\alpha - \frac{z}{r}\; sin\alpha \right), \tag{2.2}$$

where z is the height of the satellite above the Earth's surface, and depends on the curvature of the Earth and topography [*Rodriguez and Martin*, 1992]. Setting z to the height of a reference ellipsoid for the Earth and subtracting the resultant

phase from the interferogram phase leaves only phase due to topography (Figure 2-3). Thus InSAR provides a means to estimate topography, which was the goal of initial applications [e.g., *Zebker and Goldstein*, 1986; *Gabriel and Goldstein*, 1988]. However, the phase detected by SAR sensors is not absolute phase, but rather phase modulo 2π. Thus it is not possible to calculate absolute height, only relative height between two points in an interferogram. In order to calculate the relative height between all points, the differential phase between all neighboring pixels is integrated over the interferogram, although phase jumps of more than π in magnitude make the solution non-unique. This process, known as "phase unwrapping", is discussed in detail in Chapter 5.

The phase due to topography can also be estimated, either from InSAR or a digital elevation model (DEM), and subtracted from the interferogram phase. If we continue to ignore decorrelation and atmospheric effects, the remaining phase will be due to any deformation of the Earth's surface between the two acquisitions,

$$\phi = -\frac{4\pi}{\lambda}\, u_{LOS} \tag{2.3}$$

where u_{LOS} is the displacement of the Earth's surface in the line-of-sight (LOS) of the satellite. This was first noted by *Gabriel et al.* [1989] and applied by *Massonnet et al.* [1993] and *Zebker et al.* [1994] to image ground displacements associated with the Landers earthquake (Figure 2-4). Over the last decade, although not limited to these applications, InSAR has proven to be a very effective technique for measuring deformation from active volcanism [e.g., *Amelung et al.*, 2000; *Pritchard and Simons*, 2002; *Wicks et al.*, 2006], co- and post-seismic motions [e.g., *Wright et al.*, 2001; *Jónsson et al.*, 2002], and ground subsidence from the withdrawal of groundwater [e.g., *Hoffmann et al.*, 2001]. However, almost any interferogram includes large areas where the signals decorrelate and no measurement is possible. If the surface is vegetated, weathers appreciably or is prone to snow coverage, the scattering properties change with time leading to a loss of interferometric coherence, a phenomenon known as temporal decorrelation [*Li and Goldstein*, 1990; *Zebker and Villasenor*, 1992]. Consequently, most InSAR studies to date have focused on areas that are dry and sparsely

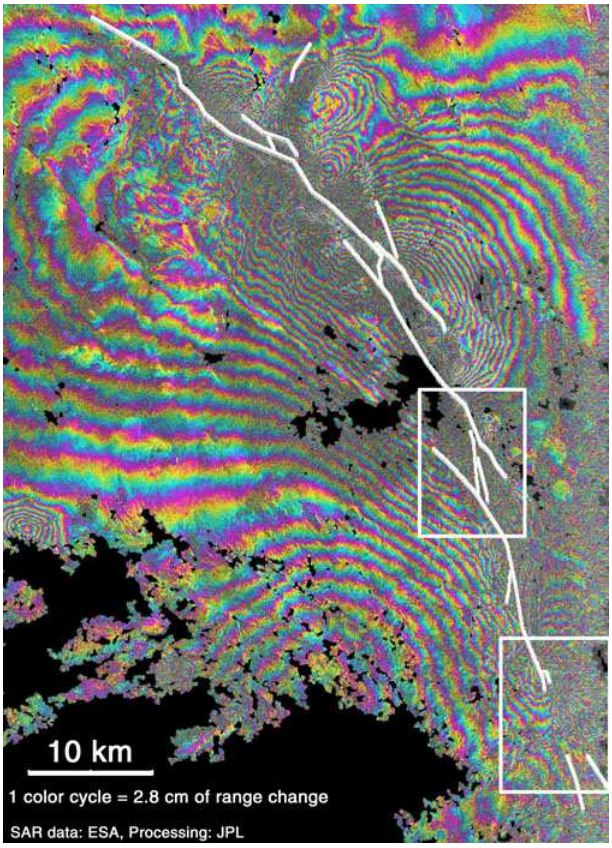

Figure 2-4: Interferogram, produced by JPL, showing line-of-sight displacements associated with the 1992 Landers earthquake.

vegetated, for example, the desert southwest of the U.S., Turkey or Tibet.

Decorrelation also results from variations in imaging geometry. If the perpendicular baseline between the spacecraft position at the two times at which the images are acquired (see Figure 2-2 for definition) is non-zero, the difference in incidence angle alters the coherent sum of wavelets from the many small scattering elements within a resolution cell, so that measurements do not repeat exactly. This phenomenon, referred to as spatial decorrelation [*Zebker and Villasenor*, 1992], increases as the baseline increases. Thus, poor orbit control produces candidate InSAR pairs with excessive baselines that cannot be used to produce interferograms. A corresponding decorrelation results from changes in squint angle, the angle with which the spacecraft

is pointed forward or backward. A change in squint angle alters the SAR Doppler frequency range leading to decorrelation. The squint angle on the ERS-2 and Radarsat-1 satellites has, at times, not been well constrained. Although these decorrelation effects can be reduced by filtering, there are critical values of baseline and squint angle difference beyond which there is complete loss of interferogram coherence [*Zebker and Villasenor*, 1992]. In summary, even if SAR data are regularly acquired, temporal and spatial decorrelation limit the number of possible interferograms and hence temporal resolution.

After decorrelation, the next most significant limitation of conventional InSAR is the variation in the delay of the signal as it propagates through the atmosphere, which leads to an additional phase term that varies over the image [e.g., *Hanssen*, 2001]. Most of the variation in this term over the typical dimensions of an interferogram is due to variation in the distribution of water vapor in the atmosphere. The atmospheric phase term is, locally, correlated in space with the spectral power of the spatial variation in phase delay generally approximating a power law for areas lacking in significant topography. Where there is significant topography, there is further variation that correlates with surface height. An example of an interferogram displaying extreme atmospheric variation is shown in Figure 2-5. Atmospheric phase delay is generally correlated in time on the scale of hours to days. As the time between spacecraft passes is of order one month, the atmospheric signal is effectively decorrelated in time. A common method for reducing atmospheric signal is, therefore, to stack multiple interferograms acquired over time. However, any variation in the spatial or temporal nature of deformation over the period of the stack is then lost.

2.2 Persistent Scatterer InSAR

Persistent Scatterer (PS) InSAR is an extension to the conventional InSAR techniques described above, which addresses the problems of decorrelation and atmospheric delay. The degree of decorrelation within a pixel depends on the distribution of scattering centers on the ground that contribute to that pixel. In a radar image, the reflected wave from a resolution element is the coherent sum of individual wavelets scattered

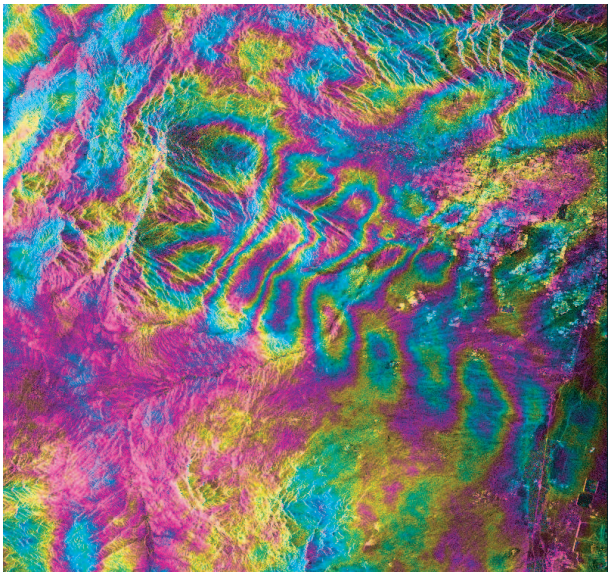

Figure 2-5: Interferogram for Tucson region covering the period Jan 27 to April 6, 1996, from *Hoffmann* [2003]. There was no appreciable deformation during this time period and all the phase variation seen here is due to variation in atmospheric path delay. The image is approximately 50 x 50 km, and each color fringe represents 2.8 cm of relative path delay.

by many discrete scatterers (Figure 2-6a). Constructive and destructive interference of these wavelets gives rise to variation in the phase and amplitude of the pixel with both viewing angle and relative movement of the scatterers. This is illustrated by the plot below the cartoon in Figure 2-6a, showing the phase of the radar echo if the individual scatterers contributing to the pixel move randomly over time, by large distances compared to the radar wavelength. This simulates complete temporal decorrelation, although simulating complete spatial decorrelation would produce the same variation in phase, that is, phase that varies over the full $\pm\pi$ radians range and is effectively random. In contrast, if one of the scatterers contributing to the pixel is much brighter than the others (Figure 2-6b), the largest contributor to the phase is the wavelet from the brighter scatterer and there is little interference from the other scatterers. The signal received for this pixel varies little as the other scatterers move around, and any motion of the scatterer can be readily measured by the phase of the radar echo.

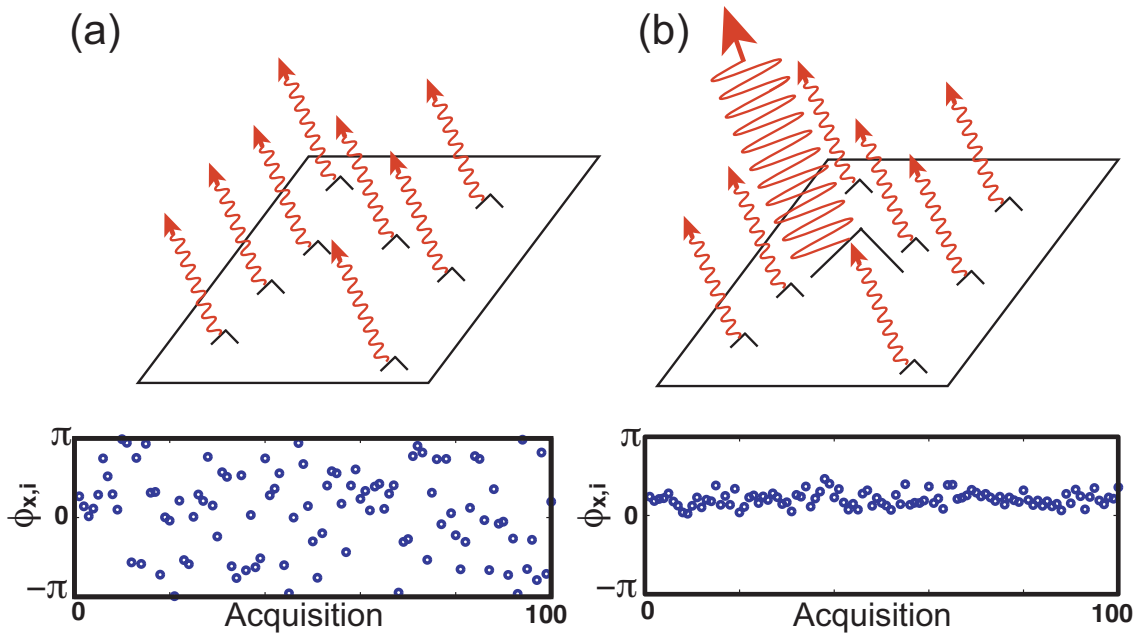

Figure 2-6: Phase simulations for (a) a distributed scatterer pixel and (b) a persistent scatterer pixel. The cartoons above represent the scatterers contributing to the phase of one pixel in an image and the plots below show simulations of the phase for 100 iterations, with the smaller scatterers moving randomly between each iteration. The brighter scatterer in (b) is three times brighter than the sum of the smaller scatterers.

If the phase of a pixel were determined by just one point scatterer, the decorrelation would be reduced to zero and all radar images of the area would form usable interferograms. Although this is rarely the case, there are pixels where one scatterer dominates the echo and which behave somewhat like point scatterers, so that decorrelation is greatly reduced. This is our model for a PS pixel. Physically this might be the corner of a building, a tree trunk dominating contributions from smaller branches and leaves, or a single large rock or facet amidst rubble on a lava flow. One can thus obtain useful data from all image pairs enabling the formation of a series of interferograms, all referenced to the same "master" scene. The atmospheric delay signal can then be estimated and removed by filtering of the resulting phase time series obtained for each of the PS pixels.

An algorithm to exploit PS pixels was first achieved by *Ferretti et al.* [2000, 2001].

They have patented this procedure and refer to it as the "permanent scatterers technique". PS pixels are identified as those pixels whose phase histories match an assumed model of how displacement varies with time. Similar processing algorithms have since been developed by *Crosetto et al.* [2003], *Lyons and Sandwell* [2003], *Werner et al.* [2003] and *Kampes* [2005]. These methods have been very successful for InSAR analysis of radar scenes containing large numbers of man-made structures, which tend to be angular and often produce very efficient reflectors that dominate background scattering. A good example is shown in Figure 2-7, an image of the San Francisco Bay area. Reliable deformation measurements are obtained over the urban regions, including parts of the Hayward fault (HF) in the East Bay. However, almost no permanent scatterers are seen along the San Andreas fault (SAF) on the San Francisco peninsula, and coverage along the Calaveras fault (CF) to the east is spotty, where artificial structures are sparse.

Because these methods use a functional model of temporal displacement to identify PS pixels, approximate knowledge of how the deformation varies with time is required *a priori*. Commonly, deformation is assumed to be steady-state or periodic in nature. However, in deformation studies the temporal nature of the deformation is usually one of the phenomena that we wish to determine. Volcanoes, for example, often deform in a very episodic and non-steady fashion. The temporal pattern of deformation during transient fault slip events, and postseismic deformation is also not known *a priori*. *Hilley et al.* [2004] were able to use the data in Figure 2-7 to track the motion of slow moving landslides in the Berkeley Hills, because the non-steady motion of the permanent scatterers within the landslides is small in magnitude. On the other hand, Figure 2-8 shows an episodic landslide in Italy where no permanent scatterers were detected, despite the presence of many buildings within the sliding area [*Paulo Farina*, pers. comm.]. In this data set, the non-steady nature of the deformation precludes analysis by the *Ferretti et al.* [2001] permanent scatterer method.

We describe in subsequent chapters a new analysis method, denoted StaMPS (Stanford Method for Persistent Scatterers), that we can use to identify and extract the deformation signal from stable pixels in all terrains. We are able to find many stable pixels in non-urban areas where we are unable to do so using the *Ferretti et al.*

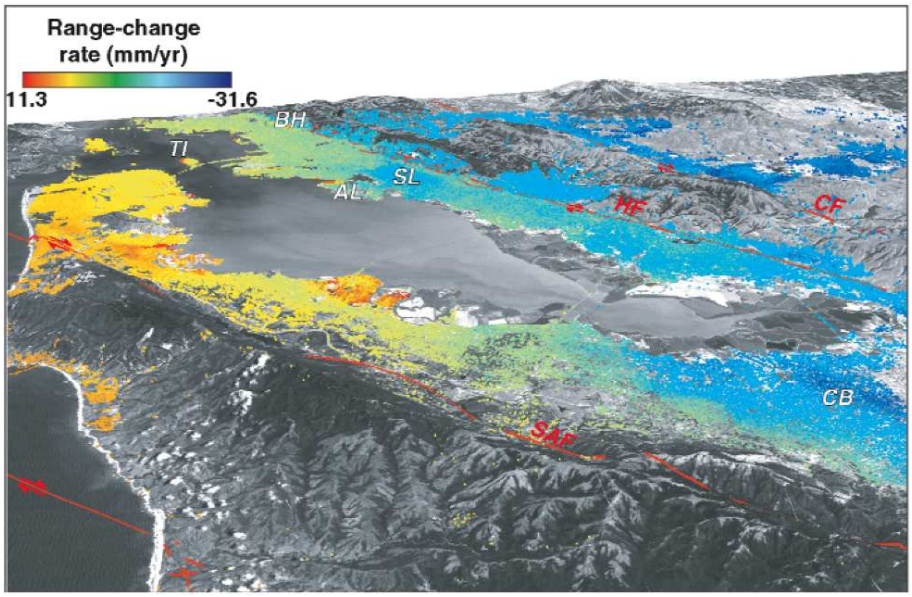

Figure 2-7: "Permanent scatterers" in the San Francisco Bay area from *Ferretti et al.* [2004]. The permanent scatterers are represented by colored points, the color of each point indicating its measured velocity toward or away from the ERS SAR satellite flying toward 193 and looking down from the east at a look angle of 23. The background image is a three-dimensional view of LandSat imagery draped over the topography. SAF, HF and CF denote the locations of the San Andreas, Hayward and Calaveras faults, respectively. CB, SL, AL,TI and BH show locations of the Cupertino and San Leandro basins, Alameda, Treasure Island, and the Berkeley Hills, respectively.

[2001] algorithm. Because the algorithm uses spatial correlation of phase measurements, rather than a functional temporal model, to indentify PS pixels, it is applicable in areas undergoing non-steady deformation with no prior knowledge of the variations in deformation rate. Once PS pixels are identified, the StaMPS algorithm entails a number of further steps to isolate the deformational signal, including a step in which most of the atmospheric signal is estimated and removed.

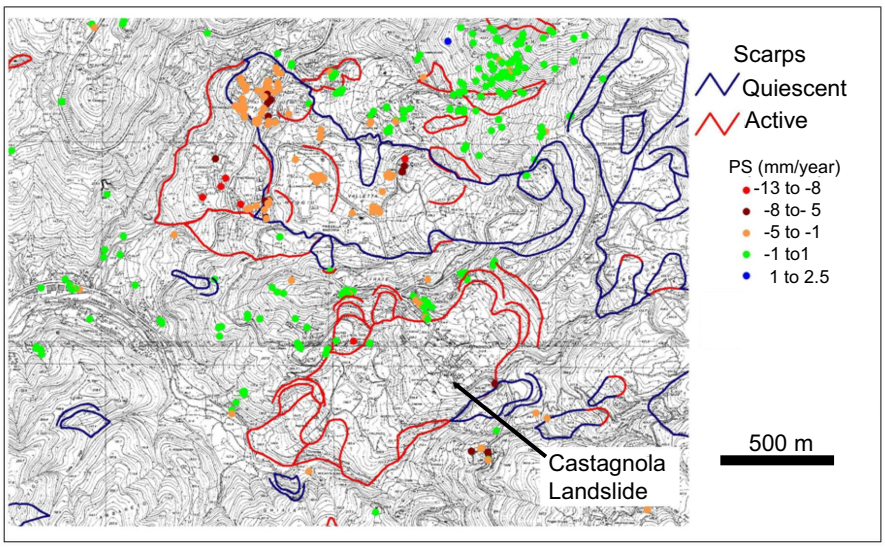

Figure 2-8: "Permanent scatterers" around the Castagnola landslide area [courtesy of Paulo Farina]. No "permanent scatterers" were found within the landslide area itself, despite the presence of many buildings in Castagnola.

Chapter 3

A New Persistent Scatterer InSAR Method Applied to Long Valley Caldera

In this chapter we present a new InSAR persistent scatterer (PS) method for analyzing episodic crustal deformation in non-urban environments, with application to volcanic settings. This work is an early implementation of our algorithm, not the complete Stanford Method for PS (StaMPS) which is described in Chapter 4. The algorithm for identifying PS pixels in a series of interferograms is based primarily on phase characteristics and finds low amplitude pixels with phase stability that are not identified by the existing algorithms. Our method also uses the spatial correlation of the phases rather than a well-defined phase history so that we can observe temporally-variable processes, e.g., volcanic deformation. The algorithm involves removing the residual topographic component of flattened interferogram phase for each PS, and then unwrapping the PS phases both spatially and temporally. Our method finds scatterers with stable phase characteristics, independent of amplitudes associated with man-made objects. Our method is also applicable to areas where conventional InSAR fails due to complete decorrelation of the majority of scatterers, yet a few stable scatterers are present.

3.1 Introduction

A major limitation in our ability to model volcanic processes is the lack of deformation data for most active volcanoes. While conventional InSAR has proven very effective in measuring deformation in regions of good coherence [e.g., *Massonnet et al.*, 1995; *Amelung et al.*, 2000], it is clear from almost any volcano interferogram that there are large areas on most volcanoes where signals decorrelate and no measurement is possible. If the surface is vegetated, weathers appreciably or is prone to snow coverage, the scattering properties change with time and result in temporal decorrelation, i.e. the loss of interferogram coherence with time [*Zebker and Villasenor*, 1992]. Another limitation of existing InSAR methods is the lack of temporal resolution in the data. While to a large extent this limitation is a function of how often SAR data are acquired, there are two other aspects of conventional InSAR that limit the number of scenes from which interferograms can be produced. The first is the distance between the spacecraft tracks at the two times scenes are acquired, known as the perpendicular baseline. A non-zero baseline leads to a difference in incidence angle which alters the scattering phases, a phenomenon referred to as spatial decorrelation [*Zebker and Villasenor*, 1992]. As the baseline increases, spatial decorrelation also increases. A second limitation results from the changes in squint angle, the angle with which the spacecraft is looking forward (or backward). A change in squint angle alters the SAR Doppler frequency and leads to additional decorrelation. Although these non-temporal causes of decorrelation can be reduced somewhat by filtering, there are critical values of baseline and squint angle difference beyond which there is complete loss of interferogram coherence [*Zebker and Villasenor*, 1992].

The degree of decorrelation of radar signals depends on the distribution of scattering centers within a pixel. If the phase of a pixel were determined by just one point scatterer, the decorrelation would be reduced to zero. Although this is never the case for real surfaces, there are pixels which behave somewhat like point scatterers, and for which decorrelation is greatly reduced. Hence, in an interferogram some pixels will exhibit less decorrelation than others. It is possible to avoid many limitations of conventional InSAR by analyzing only pixels which retain some degree of correlation,

which we define as persistent scatterers.

A different approach to processing is required to identify and isolate these pixels. This approach was first realized for InSAR applications by *Ferretti et al.* [2000, 2001], with further enhancements by *Colesanti et al.* [2003b], and is referred to as the Permanent Scatterers Technique™ in their patented procedure. Other persistent scatterer processing systems have since been developed [e.g., *Adam et al.*, 2003; *Crosetto et al.*, 2003; *Lyons and Sandwell*, 2003; *Werner et al.*, 2003]. In these algorithms, an initial set of PS pixels are identified by analysis of their amplitude scintillations in a series of interferograms. This method works best in urban areas where man-made structures increase the likelihood of finding a non-fluctuating scatterer in any given pixel. Persistent scatterers have also been identified in non-urban areas such as Ranafjord in northern Norway [*Dehls et al.*, 2002].

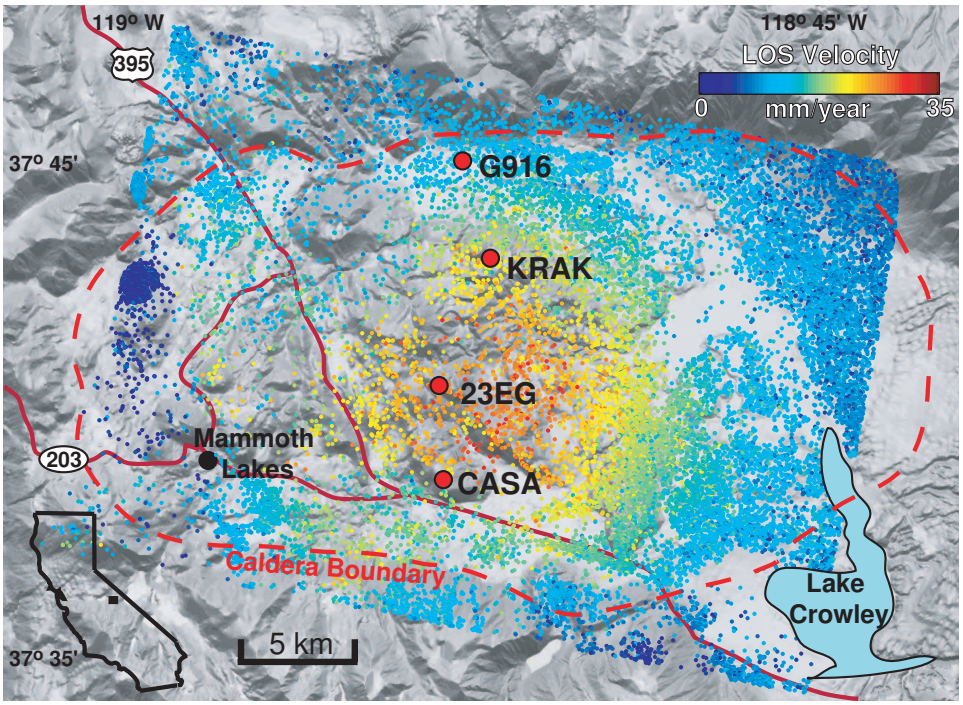

Figure 3-1: Location of Long Valley Caldera in California and the PS identified within the study area superimposed on a shaded relief map. The color of each PS represents the mean velocity in LOS.

While amplitude analysis is reasonably successful in urban areas, the density of PS

pixels identified by amplitude dispersion thresholding in natural terrains is generally too low to obtain any reliable results. Our new method uses phase analysis for identification of PS pixels and is successfully applied to a volcanic area where we failed to find an initial set of PS pixels using amplitude dispersion thresholding, with sufficient density to be reliable.

In order to estimate and remove nuisance terms, PS processing systems to date must simultaneously estimate the deformation for each PS, which requires a model for the deformation with time. In the case of volcanoes, deformation tends to be episodic and not readily parameterized. In contrast our method produces a time series of deformation, with no prior assumptions about the temporal nature of deformation. This is achieved by using the spatially correlated nature of the deformation rather than requiring a known temporal dependence.

3.2 Method

3.2.1 Persistent Scatterer Selection

Because PS are defined by phase stability we select PS candidates on the basis of their phase characteristics. Existing methods for selecting PS candidates rely on thresholding pixel amplitude variability with time, defined as the ratio of the standard deviation of the amplitude over its mean [*Ferretti et al.*, 2001]. For high (> 10) signal to noise ratio (SNR), amplitude dispersion is an accurate proxy for phase standard deviation and thus the method has a high success rate at picking bright PS, e.g., certain man-made structures. However, for low SNR scatterers, the simple relationship between amplitude dispersion and phase stability breaks down and the method is no longer effective.

Our approach is to form interferograms and remove most of the topographic phase signature using a digital elevation model (DEM).

The residual phase, ϕ_{int}, of the xth pixel in the ith topographically corrected

interferogram can be written as the sum of 5 terms,

$$\phi_{int,x,i} = \phi_{def,x,i} + \Delta\phi_{\varepsilon,x,i} + \phi_{atm,x,i} + \Delta\phi_{orb,x,i} + \phi_{n,x,i} \tag{3.1}$$

where ϕ_{def} is the phase change due to movement of the pixel in the satellite line-of-sight (LOS) direction, $\Delta\phi_{\varepsilon}$ is the residual topographic phase due to error in the DEM, ϕ_{atm} is the phase equivalent of the difference in atmospheric retardation between passes, $\Delta\phi_{orb}$ is the residual phase due to orbit inaccuracies and ϕ_n the noise term due to variability in scattering from the pixel, thermal noise and coregistration errors. We define PS as pixels where ϕ_n is small enough that it does not completely obscure the signal.

Variation in the first four terms of Eq. 3.1 can dominate the noise term making it difficult to identify which scatterers are persistent. We assume that ϕ_{def}, ϕ_{atm} and $\Delta\phi_{orb}$ are spatially correlated over distances of a specified length scale, L, and that $\Delta\phi_{\varepsilon}$ and ϕ_n are uncorrelated over the same distance, with a mean of zero. If the position of other PS are already known, averaging the phase of all those within a circular patch centered on pixel x with radius L implies

$$\bar{\phi}_{int,x,i} = \bar{\phi}_{def,x,i} + \bar{\phi}_{atm,x,i} + \Delta\bar{\phi}_{orb,x,i} + \bar{\phi}_{n,x,i} \tag{3.2}$$

where the bar denotes the sample mean of the patch and $\bar{\phi}_n$ is the sample mean of $\phi_n + \Delta\phi_{\varepsilon}$ and is assumed small. Subtracting Eq. 3.2 from Eq. 3.1 leaves

$$\phi_{int,x,i} - \bar{\phi}_{int,x,i} = \Delta\phi_{\varepsilon,x,i} + \phi_{n,x,i} - \bar{\phi}'_{n,x,i} \tag{3.3}$$

where $\bar{\phi}'_n$ is the sum of $\bar{\phi}_n$ plus the differences between the patch mean values and the pixel values of ϕ_{def}, ϕ_{atm} and $\Delta\phi_{orb}$.

The phase error from uncertainty in the DEM is proportional to the perpendicular component of the baseline, $B_{\perp}$, so

$$\Delta\phi_{\varepsilon,x,i} = B_{\perp,x,i} K_{\varepsilon,x} \tag{3.4}$$

where K_ε is a proportionality constant. Substituting this expression into Eq. 3.3 gives

$$\phi_{int,x,i} - \bar{\phi}_{int,x,i} = B_{\perp,x,i}K_{\varepsilon,x} + \phi_{n,x,i} - \bar{\phi}'_{n,x,i}. \tag{3.5}$$

Using all the available interferograms we are able to estimate K_ε for pixel x in a least square sense, as this is the only term that would correlate with baseline.

We define a measure based on the temporal coherence of pixel x as

$$\gamma_x = \frac{1}{N}\left|\sum_{i=1}^{N}\exp\{j(\phi_{int,x,i} - \bar{\phi}_{int,x,i} - \Delta\hat{\phi}_{\varepsilon,x,i})\}\right| \tag{3.6}$$

where N is the number of available interferograms and $\Delta\hat{\phi}_{\varepsilon,x,i}$ is our estimate of $\Delta\phi_{\varepsilon,x,i}$. Assuming $\bar{\phi}'_{n,x,i}$ values are small, γ_x is a measure of the phase stability of the pixel and hence an indicator of whether the pixel is a PS.

Because the algorithm requires PS phases to calculate the patch mean, it can identify PS given that the locations of other PS are already known. As we start with no knowledge of the location of any PS, we use an iterative algorithm to identify PS in all locations simultaneously. For computational reasons, we make an initial selection of PS candidates based on amplitude dispersion with a high threshold value (0.4). Unlike the initial selection in the *Ferretti et al.* [2001] algorithm, the vast majority of those selected are not actually PS. For each PS candidate, we subtract the mean of the other local candidates as in Eq. 3.3, estimate $K_{\varepsilon,x}$ and calculate γ_x. Generally, $\bar{\phi}'_{n,x,i}$ will not be negligible as the signal of the majority of the PS candidates included in the mean phase will be dominated by noise. Statistically, however, pixels with higher γ_x are more likely to be PS. Hence we temporarily reject candidates with low γ_x and recalculate the patch means using only the remaining candidates. We then recalculate γ_x for every candidate. Generally the values of $\bar{\phi}'_{n,x,i}$ will be smaller than before and by iterating a number of times the contribution of $\bar{\phi}'_{n,x,i}$ is gradually reduced so that γ_x becomes dominated by $\phi_{n,x,i}$.

The final step is to select PS based on the calculated values of γ_x. Any pixel with random phase has a finite chance of having high γ_x and therefore we can only select in a probablistic fashion. We therefore find a threshold value γ^{thresh} that maximizes the

number of real PS selected while keeping the fraction of random phase pixels selected (false positives) below a specified value, q. The probability density function (PDF) of γ_x for the data, $p(\gamma_x)$, is a weighted sum of the PDF for the random phase pixels, $p_r(\gamma_x)$, and the PDF for the non-random phase (PS) pixels, $p_{ps}(\gamma_x)$ i.e.,

$$p(\gamma_x) \;=\; (1-\alpha)p_r(\gamma_x) + \alpha p_{ps}(\gamma_x). \tag{3.7}$$

We want to find γ^{thresh} such that

$$\frac{(1-\alpha)\int_{\gamma^{thresh}}^{1} p_r(\gamma_x)\,d\gamma_x}{\int_{\gamma^{thresh}}^{1} p(\gamma_x)\,d\gamma_x} = q \tag{3.8}$$

where $p_r(\gamma_x)$, and α are unknown. $p_r(\gamma_x)$ is simulated by generating pseudo-PS candidates with random phase, estimating $K_{\varepsilon,x}$ for each and calculating γ_x. For low γ_x values (< 0.3), $p_{ps}(\gamma_x) \approx 0$. Assuming then that

$$\int_0^{0.3} p(\gamma_x)\;\; d\gamma_x \;=\; (1\;-\;\alpha)\;\int_0^{0.3} p_r(\gamma_x)\;\; d\gamma_x \tag{3.9}$$

allows a conservative value of α to be estimated and hence we can calculate γ^{thresh}.

Since the risk of false positives increases with increasing amplitude dispersion, we refine the number of PS selected further by calculating γ^{thresh} as a function of amplitude dispersion. For each PS candidate we then use the value of γ^{thresh} which corresponds to the amplitude dispersion of the candidate as the threshold value.

In order to exclude sidelobes we assume that adjacent pixels are dominated by the same scatterer, and discard all but the pixel with the highest γ_x value.

3.2.2 DEM Error Correction

Once the PS have been selected, their phase is corrected for DEM error by subtracting the estimated values of $\Delta\phi_{\varepsilon,x,i}$,

$$\phi_{int,x,i} - \Delta\hat{\phi}_{\varepsilon,x,i} = \phi_{def,x,i} + \phi_{atm,x,i} + \Delta\phi_{orb,x,i} + \Delta\phi'_{\varepsilon,x,i} + \phi_{n,x,i} \tag{3.10}$$

where $\Delta\phi'_{\varepsilon,x,i}$ is the residual DEM error term due to uncertainty in our estimate of $K_{\varepsilon,x}$, including any spatially correlated DEM error. Because the differential error between neighboring PS introduced by this spatially correlated error is small, the effect on unwrapping (see below) is negligible. However, the cumulative effect over larger areas could be significant so this spatially correlated part is estimated and removed as described in Section 3.2.4.

3.2.3 Unwrapping

As long as the density of PS is such that the absolute phase difference between neighboring PS, after correction for estimated DEM error, is generally less than π, the corrected phase values can now be unwrapped. In this analysis the unwrapping problem is in three dimensions (two spatial, as with conventional InSAR, and one temporal). Here, we approach the unwrapping as a series of two-dimensional problems. First, we calculate the temporal phase differences for each PS, and then for each time step we unwrap spatially from a reference PS using an iterative least square method. Integrating in time then gives us an unwrapped phase time series for each PS, with respect to the reference PS. This method is sufficient to map slow deformation over time and a full three-dimensional solution will likely be required if large displacements occur. In Chapter 5 we develop two three-dimensional unwrapping algorithms and apply one of them to the Long Valley data set discussed later in this chapter.

3.2.4 Spatially Correlated Terms

After unwrapping, four error terms remain in Eq. 3.10 which mask ϕ_{def}. Unlike ϕ_{def}, the spatially correlated portion of these terms is assumed to be uncorrelated temporally. Thus, by high-pass filtering the unwrapped data in time then low-pass filtering in space we are able to estimate the spatially correlated error (similar to *Ferretti et al.* [2001]). Subtracting this signal from Eq. 3.10 leaves just ϕ_{def} and spatially uncorrelated error terms that can be modeled as noise.

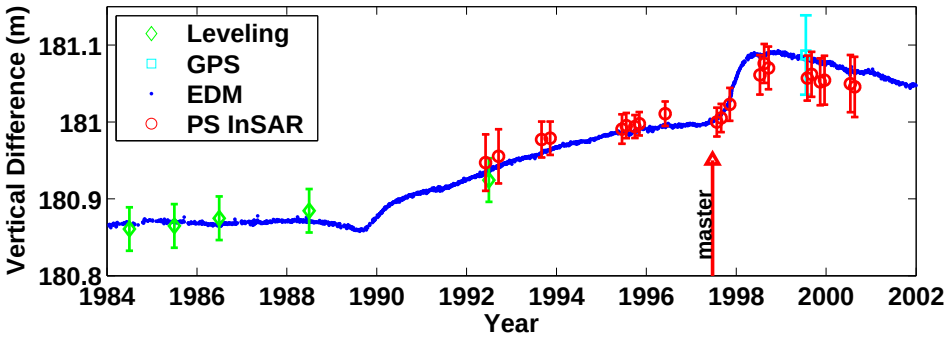

Figure 3-2: Comparison of vertical motion at Long Valley between benchmarks 23EG and G916 (see Figure 3-1) from leveling and GPS to PS (calculated from the mean phase of all PS within 500 m of the benchmarks, assuming that all relative LOS change is due to vertical motion). The error bars represent 68% confidence bounds. Also shown is the scaled line length change between CASA and KRAK as measured by EDM, which is a proxy for vertical motion.

3.3 Application

We applied our method to data acquired over Long Valley Volcanic Caldera in eastern California (see Figure 3-1). This is an area largely devoid of man-made objects and has deformed at an irregular rate since ERS data was first acquired there in 1992 (see Figure 3-2). For short temporal and perpendicular baselines, conventional interferometry works well within the caldera [*Fialko et al.*, 2001], providing a comparison for our new method (see Figure 3-3). The deformation of the caldera is also extensively monitored by other means allowing us to validate the technique. We processed 22 descending scenes acquired by ERS-1 and ERS-2 between 1992 and 2000, and oversampled by a factor of two in range and azimuth to avoid aliasing in an amplitude based registration algorithm. We then selected one scene as the "master" (based primarily on minimization of perpendicular baseline and secondarily on minimization of temporal baseline) and created 21 interferograms from each of the others.

Using amplitude dispersion thresholding [*Ferretti et al.*, 2001] the density of PS indentified over most of our region of interest was < 0.1 km^{-2}, which is too low to provide reliable results. However, with our new algorithm we identified an average 44 km^{-2} with 95% confidence (see Figure 3-1). Figure 3-3 shows a sample comparison of

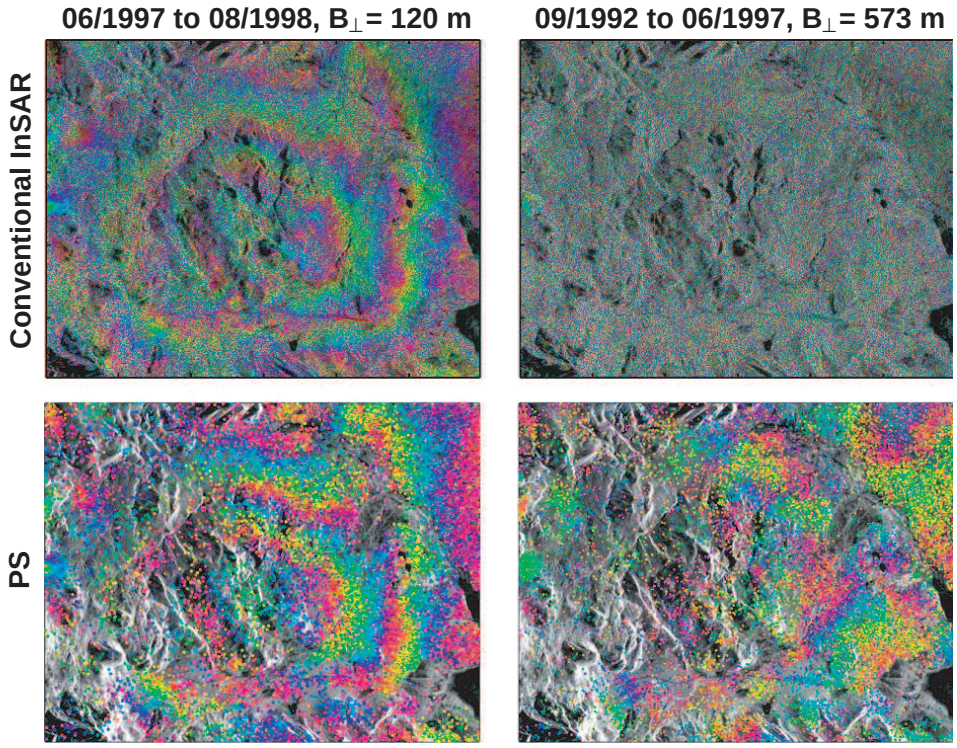

Figure 3-3: Comparison of wrapped multilooked interferograms from conventional InSAR (above) and the wrapped phase of individual PS, corrected for DEM error (below). For the conventional interferograms 4 looks were taken in range and 20 in azimuth.

the wrapped phase from conventional interferometry to the corrected phase of only the selected PS. In the shorter baseline (both perpendicular and temporal) case the results are comparable while in the longer baseline case there is considerably more spatial coherence using the new method.

From the PS phases we calculated a time series of deformation between benchmarks 23EG and G916, assuming that all the detected relative motion was vertical, and compared it to that measured by leveling and GPS, and inferred from electronic distance meter (EDM) measurements (see Figure 3-2). Motion measured by the EDM line between CASA and KRAK is almost parallel to the satellite track and hence not present in our interferograms. However, this horizontal motion across the resurgent dome is almost proportional to the vertical motion of the resurgent dome [*Battaglia*

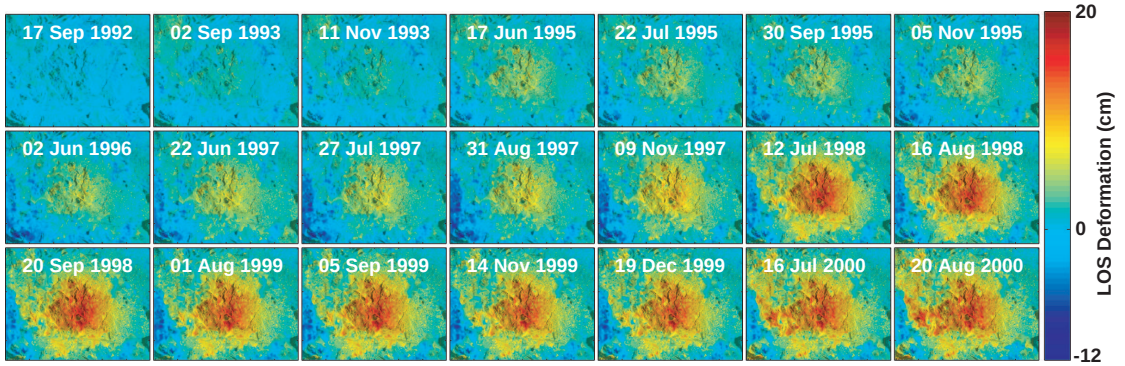

Figure 3-4: Time series of deformation at Long Valley interplolated spatially from the processed PS, referenced temporally to the earliest scene (04-Jun-1992), referenced spatially to the northeast corner and superimposed on the mean amplitude image.

et al., 2003] and, once scaled using less frequent leveling and GPS readings, is therefore a proxy for vertical deformation. PS measurements are indistinguishable from ground truth at 68% confidence. If we relax our unrealistic assumption that all the relative motion is vertical and estimate east-west motion that is proportional to the vertical motion, the fit becomes even better. The time series of deformation for the whole processed region is shown in Figure 3-4.

It is important to understand that except for true point scatterers, being a PS is not a physical characteristic of a pixel, but rather a function of the pixel and the dataset. As true point scatterers are rare even in urban areas, PS picked by any method are only point-like in their observed scattering characteristics. As the longest perpendicular baseline in the Long Valley data is 573 m, it is possible that some of the selected PS are less point-like in their scattering characteristics than would be conventionally termed PS. However, we can state that for at least 95% of the selected pixels, the signal is statistically distinguishable from the noise (our definition of a PS). If we used interferograms with longer baselines, this may no longer be true for the least point-like of the currently selected PS and they would no longer be selected as PS. In other words our method will pick the largest possible set of PS from any given dataset.

3.4 Conclusions

We have presented here a method for identifying and processing PS that i) is applicable to low-amplitude natural targets and ii) requires no prior model of deformation. Using this method, we identified 44 PS km^{-2} in a non-urban volcanic area, for which we failed to get any reliable results using the method of *Ferretti et al.* [2001]. From these PS we were able to extract the temporal and spatial pattern of deformation even where conventional interferograms showed almost complete decorrelation. Although the pattern of temporal deformation is irregular, our method was able to extract it without any prior assumptions about its nature.

While we have demonstrated the effectiveness of this method for the study of volcanic deformation, it is equally applicable to other deformation regimes such as fault slip, landslides and subsidence. Limitations of the method include:

1. The step to estimate the spatially correlated terms depends on the assumed length scale of the correlation, which is fixed. In fact, we expect this length scale to vary both in time and space and so a filter that adapts to the correlation length scales of the data would estimate these terms more accurately.

2. Phase unwrapping is challenging in some areas due to undersampling and noisiness of the data. This leads to artifacts seen in Figure 3-4, where there appears to be a discontinuity in displacement on the western side, for which there is no evidence from other geodetic measurements. Treating the unwrapping problem in three dimensions instead of two would increase the reliability of the result.

3. The method described here does not include the steps for interferogram creation, which differ in some respects from those for standard InSAR.

Chapter 4

An Improved Persistent Scatterer InSAR method for Crustal Deformation Analysis, with Application to Volcán Alcedo, Galápagos

In the previous chapter we introduced a new persistent scatterer (PS) method that uses spatial correlation of interferogram phase to find PS pixels in all terrains, with or without buildings. Prior knowledge of temporal variations in the deformation rate is not required. As discussed at the end of the previous chapter there are limitations to this method. We describe here an improved version of the method, StaMPS, that addresses these limitations and includes other minor adjustments to the method. We apply StaMPS to Volcán Alcedo, where conventional InSAR fails, due to dense vegetation on the upper flanks that causes most pixels to decorrelate with time. We detect two sources of deformation. The first we model as a contracting pipe-like body, which we interpret to be a crystallizing magma chamber. The second is downward and lateral motion on the inner slopes of the caldera, which we interpret as being due to landslides.

4.1 Introduction

Volcán Alcedo is one of six volcanoes located on Isla Isabela in the Galápagos Archipelago (Figure 4-1). Alcedo is unusual in that it is the only active Galápagos volcano known to have erupted rhyolite as well as basalt [*Geist et al.*, 1994]. The last known eruption occurred in late 1993 from the south caldera wall [*Green*, 1994]. Deformation of the caldera was detected by *Amelung et al.* [2000] who carried out InSAR analysis of ERS data acquired over Alcedo between 1992 and 1999. However, they found the coherence to be too low to determine the deformation signal on the volcano flanks and were therefore unable to draw any conclusions about the source of the deformation. No measurements of surface displacement have been made on Alcedo by any other means, and inferred displacements from SAR data are therefore all we can currently use to constrain the movement of subsurface magma and volatiles. Conventional InSAR fails on the upper flanks of Alcedo because a significant amount of vegetation is present and this leads to temporal decorrelation for most pixels in the image.

When a SAR image is formed, even at the highest possible resolution, the value for each pixel remains the coherent sum of the returns from many scatterers on the ground. If these scatterers move with respect to each other between satellite passes, as is expected to be the case when many scatterers are vegetation, the phase of the return will vary in a random manner which leads to decorrelation. If, however, a pixel is dominated by one stable scatterer that is brighter than the background scatterers, the variance in the phase of the echo due to relative movement of the background scatterers will be reduced, and may be small enough to enable extraction of the underlying deformation signal (Figure 2-6). We identified this type of pixel as a persistent scatterer (PS) pixel in Chapter 3. Physically these stable scatterers might be a tree trunk or a single large rock or facet amongst the vegetation.

Methods to identify and isolate these PS pixels in interferograms have been developed by several groups [e.g., *Ferretti et al.*, 2001; *Crosetto et al.*, 2003; *Lyons and Sandwell*, 2003; *Werner et al.*, 2003; *Kampes*, 2005]. All of these methods use a functional model of how deformation varies with time to identify PS pixels, and have been

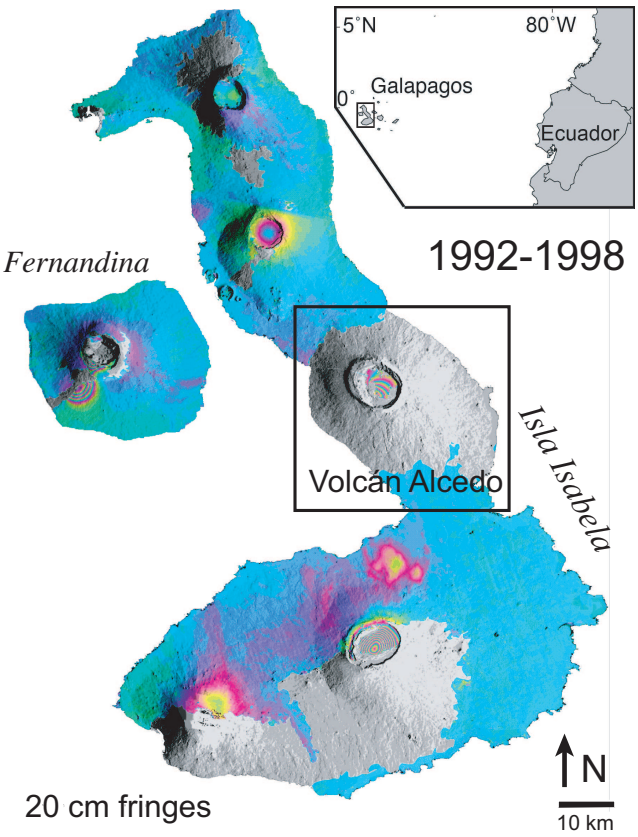

Figure 4-1: Location of Volcán Alcedo on Isla Isabela, Galápagos. The background image from *Amelung et al.* [2000], shows line-of-sight displacement between 1992 and 1998.

very successful in identifying PS pixels in urban areas undergoing primarily steady-state or periodic deformation. In these algorithms an initial set of PS pixels with a high signal to noise ratio (SNR) is identified by analysis of pixel by pixel amplitude variation in a series of interferograms. Approaches include analysis of each pixel alone [e.g., *Ferretti et al.*, 2001] or comparison with surrounding pixels [e.g., *Adam et al.*, 2005]. Once an initial set of amplitude-stable pixels has been identified, each candidate pixel is tested for phase stability by examining its phase differences with nearby candidates. Only a point whose phase history is similar to the assumed model of deformation is deemed stable and not merely the result of random chance. In this manner a network of reference PS is identified that is then used to find additional PS by further phase analysis of all (or a subset of) the remaining pixels.

This approach can fail for two reasons. First, the noise term must generally be small in magnitude because the phase analysis involves phase that is only determined modulo 2π. *Colesanti et al.* [2003b] estimate that the noise must be ≤ 0.6 radians. If the spatial distance between a reference PS and its neighbors is too large, the contribution to the phase from the difference in delay along the ray paths through the atmosphere exceeds this limit, and the pixel cannot be verified as persistent. For common atmospheric conditions, a minimum PS density of 3 to 4 per km^2 is required [*Colesanti et al.*, 2003b]. The initial selection using amplitude variation finds most bright PS, such as those from man-made structures, and therefore works well in urban areas where the density of structures is high. However, in most natural terrains, including the majority of volcanoes, bright scatterers are rare and the density of reference PS is generally too low to form a closely-spaced reference network. We found this to be the case for Long Valley volcanic caldera in Chapter 3, and the same has been reported for the central San Andreas Fault zone [*Johanson and Bürgmann*, 2001].

The second limitation is that an approximate model for the temporal variation in deformation is needed to isolate the deformation signal from atmospheric, topographic and other phase errors. Because the data are wrapped, the phase difference between the model and the actual deformation must be less than π radians in magnitude. As the time dependence of deformation is not usually known a priori, it is usually assumed to be approximately constant in rate, or periodic in nature. If PS can be identified, deviations from the parametric model may be estimated from the residuals [*Ferretti et al.*, 2000; *Colesanti et al.*, 2003b; *Kampes*, 2005]. This assumption is valid, as long as the deviations from the model are small, as in a set of interferograms of the San Francisco Bay Area [*Ferretti et al.*, 2004], where deformation is due primarily to steady strain accumulation on the San Andreas Fault System. In cases where deformation is non-steady, such as most volcanoes and landslides, as well as certain tectonic settings e.g., those dominated by post-seismic deformation, a reliable network of reference PS will not result. A method is required that produces a time series of deformation, with no prior assumptions about its temporal nature.

In Chapter 3 we introduced a PS method to extract the deformation signal from

SAR data acquired over Long Valley caldera, an area that contains few man-made structures and that deformed at variable rates during the time period analyzed. We also applied a variation of this method to the Taupo volcanic zone, New Zealand in *Hole et al.* [2006]. In this chapter, we report on significant improvements to the method which increase the accuracy of the estimated displacements and also make it applicable in areas with widely varying deformation gradients. We first describe in detail our method, StaMPS (Stanford Method for PS), for identifying PS pixels and estimating their displacements. We then apply StaMPS to SAR data acquired over Volcán Alcedo and model the source of the deformation seen in the resulting PS interferograms.

There are four parts to StaMPS, each discussed in detail in subsequent sections:

1. Interferogram Formation. There are aspects of interferogram formation for PS processing that differ to conventional interferogram formation. We summarize all the steps involved, and decribe the differences in detail. We also discuss the error terms associated with the processing.

2. PS Identification. We use both amplitude and phase analysis to determine the PS probability for individual pixels. First we make an initial selection based only on amplitude analysis, then we refine the PS probability using phase analysis in an iterative process. Finally, we estimate the PS probability for those pixels not included in the initial selection.

3. PS Selection. We select PS based on their PS probability, rejecting those that appear to be persistent only in certain interferograms and those that appear to be dominated by scatterers in adjacent PS pixels.

4. Displacement Estimation. Once selected, we isolate the signal due to deformation in the PS pixels. This involves "unwrapping" the phase values and subtracting estimates of the various nuisance terms.

4.2 Interferogram Formation

For PS systems relying on a functional temporal model to select PS, typically at least 25 interferograms are required to obtain reliable results [*Colesanti et al.*, 2003a]. Using StaMPS, however, fewer interferograms are required. We find that 12 interferograms are usually sufficient and, in one case at least, have even been able to identify PS pixels using just four interferograms. The limiting factor is the accuracy in estimation of the look angle error (Eq. 4.23), which is aided by good DEM accuracy and high SNR.

It is possible to use PS analysis on images acquired by sensors with different carrier frequencies, for example, ERS and ENVISAT [e.g., *Adam et al.*, 2005; *Arnaud et al.*, 2004; *Arrigoni et al.*, 2004]. However, the number of PS pixels is reduced as only pixels dominated by the most point-like scatterers remain correlated at different frequencies. Because PS pixels in non-urban terrains tend to be less point-like in their scattering characteristics, we only consider here interferometry between images acquired by sensors with the same carrier frequency to maximize the number of identified PS pixels.

There are several aspects of interferogram formation for StaMPS that differ from conventional InSAR processing, which we describe below with a discussion of the error terms that arise in interferometric processing.

4.2.1 Decorrelation and Choice of "Master" Image

Suppose we form N single-look interferograms from $N + 1$ images, all with respect to one "master" image. We choose as the "master", the image that minimizes the sum decorrelation, i.e., maximizes the sum correlation, of all the interferograms. The correlation is a product of four terms, dependent on temporal baseline (T), spatial perpendicular baseline ($B_\perp$, see Figure 2-2) doppler centroid baseline (F_{DC}) and thermal noise [*Zebker and Villasenor*, 1992]. A simple model for the total correlation,

ρ_{total}, is

$$\begin{aligned} \rho_{total} &= \rho_{temporal} \cdot \rho_{spatial} \cdot \rho_{doppler} \cdot \rho_{thermal} \\ &\approx \left(1 - f\left(\frac{T}{T^c}\right)\right)\left(1 - f\left(\frac{B_\perp}{B_\perp^c}\right)\right)\left(1 - f\left(\frac{F_{DC}}{F_{DC}^c}\right)\right)\rho_{thermal} \qquad (4.1) \\ & \qquad (4.2) \end{aligned}$$

where

$$f(x) = \begin{cases} x, \text{for } x \leq 1 \\ 1, \text{for } x > 1 \end{cases},$$

ρ denotes correlation and superscript c denotes the critical parameter values, i.e., the value beyond which an interferogram exhibits almost complete decorrelation. The critical values are dependent on the dataset, but typical values for ERS data in arid regions are $T^c = 5$ years, $B_\perp^c = 1100$ m and $F_{DC}^c = 1380$ Hz. We choose the "master" that maximizes $\sum_{i=1}^{N} \rho_{total}$, assuming a constant value for $\rho_{thermal}$.

We do not apply any spectral filtering in range or azimuth, which would increase the correlation, as this lowers the resolution. Generally, the higher the resolution, the fewer scatterers will be contained within each resolution cell, and the greater the chance of the cell being dominated by one scatterer. The trade-off is that, except for truly point-like PS pixels, phase values will include decorrelation noise related to perpendicular and Doppler baselines.

Our algorithm for PS identification does not actually require that all interferograms are formed with respect to just one "master", only that all are coregistered to one "master". Although we have not implemented this option in our code, if decorrelation is causing particular problems, combinations of interferograms using multiple "masters" could be chosen to increase the sum correlation.

4.2.2 Coregistration

Some interferograms will have values of temporal, perpendicular and Doppler baselines that are higher than would be commonly chosen for conventional InSAR. This leads to high decorrelation and a corresponding low coherence which make standard

coregistration routines, based on cross-correlation of amplitude, fail. We have, therefore, developed a coregistration algorithm that uses an amplitude based algorithm to estimate offsets between pairs of images where we expect reasonable coherence. The mapping function of the "master" image to each other image is then estimated by weighted least-squares inversion.

For image m, we define a function $f_x^m(x^m, y^m)$ that maps position $x^m \rightarrow x^0$ and $f_y^m(x^m, y^m)$ that maps position $y^m \rightarrow y^0$ where x and y denote range and azimuth position respectively and superscript 0 denotes the "master" image. We parameterize this function as

$$f_x^m(x^m, y^m) = a_{00}^m + a_{10}^m x^m + a_{01}^m y^m + a_{11}^m x^m y^m + ... + a_{pq}^m (x^m)^p (y^m)^q + ... \qquad (4.3)$$

where a_{pq}^m represents the coefficient that is pth-order in x and qth-order in y for mapping image m to the "master" image. Typically we use terms up to 2nd-order. We parameterize $f_y^m(x^m, y^m)$ similarly. For image pair m and n, which form an interferogram with coherence high enough to calculate offsets between the two, we estimate $\Delta\widehat{x}_{m,i}^n$ and $\Delta\widehat{y}_{m,i}^n$ at point i using amplitude cross-correlation of a data subset centered on i, where $\Delta x_{m,i}^n$ maps $x_i^m \rightarrow x_i^n$, i.e., $x_i^n = x_i^m + \Delta x_{m,i}^n$ and $\Delta y_{m,i}^n$ maps $y_i^m \rightarrow y_i^n$. As $\Delta x_{m,i}^n = \Delta x_{m,i}^0 - \Delta x_{n,i}^0$ we can simultaneously estimate the coefficients of function $f_x^m(x^m, y^m)$ for all m by inverting the following linear system of equations,

$$\begin{bmatrix} \cdot \\ \Delta\widehat{x}_{m,i}^n \\ \Delta\widehat{x}_{m,i+1}^n \\ \cdot \end{bmatrix} = \begin{bmatrix} \cdots & \cdot & \cdot & \cdot & \cdots & \cdot & \cdot & \cdot & \cdots \\ \cdots & 1 & x_i^m & y_i^m & \cdots & -1 & -x_i^n & -y_i^n & \cdots \\ \cdots & 1 & x_{i+1}^m & y_{i+1}^m & \cdots & -1 & -x_{i+1}^n & -y_{i+1}^n & \cdots \\ \cdots & \cdot & \cdot & \cdot & \cdots & \cdot & \cdot & \cdot & \cdots \end{bmatrix} \begin{bmatrix} \cdot \\ a_{00}^m \\ a_{10}^m \\ a_{01}^m \\ \cdot \\ \cdot \\ a_{00}^n \\ a_{10}^n \\ a_{01}^n \\ \cdot \end{bmatrix}. \qquad (4.4)$$

We use weighted least squares inversion, with the weighting for each estimate being $1/\sigma_{\Delta\widehat{x}}$ where $\sigma_{\Delta\widehat{x}}$ is the standard deviation of the estimate $\Delta\widehat{x}$. We use the formula derived by [*Bamler*, 2000] relating $\sigma_{\Delta\widehat{x}}$ to the coherence of the cross correlation, γ, to estimate $\sigma_{\Delta\widehat{x}}$,

$$\sigma_{\Delta\widehat{x}} = \sqrt{\frac{3}{2N}}\frac{\sqrt{1-\gamma^2}}{\pi\gamma} osf^{3/2} \tag{4.5}$$

where N is the number of samples in the estimation window and osf is the oversampling factor of the data. We find the coefficients of $f_y^m(x^m, y^m)$ similarly.

In order to resample from image m into the "master" coordinate system, the functions we require are actually the inverse functions, $g_x^m(x^0, y^0)$ and $g_y^m(x^0, y^0)$ that map position $x^0 \rightarrow x^m$ and $y^0 \rightarrow y^m$ respectively. We obtain these functions by synthesizing a grid of values of x^m and y^m for each image, calculating $\Delta x_{m,i}^0$ and $\Delta y_{m,i}^0$ from $f_x^m(x^m, y^m)$ and $f_y^m(x^m, y^m)$, and inverting these values to get the coefficients of $g_x^m(x^0, y^0)$, b_{pq}^m, by inverting the following system of linear equations,

$$\begin{bmatrix} \cdot \\ -\Delta\widehat{x}_{m,i}^0 \\ -\Delta\widehat{x}_{m,i+1}^0 \\ \cdot \end{bmatrix} = \begin{bmatrix} \cdots & \cdot & \cdot & \cdot & \cdot & \cdots \\ \cdots & 1 & x_i^0 & y_i^0 & x_i^0 y_i^0 & \cdots \\ \cdots & 1 & x_{i+1}^0 & y_{i+1}^0 & x_{i+1}^0 y_{i+1}^0 & \cdots \\ \cdots & \cdot & \cdot & \cdot & \cdot & \cdots \end{bmatrix} \begin{bmatrix} \cdot \\ \cdot \\ b_{00}^m \\ b_{10}^m \\ b_{01}^m \\ b_{11}^m \\ \cdot \\ \cdot \end{bmatrix}. \tag{4.6}$$

where $x_i^0 = x_i^m + \Delta x_{m,1}^0$ and $y_i^0 = y_i^m + \Delta y_{m,1}^0$. We find $g_y^m(x^0, y^0)$ similarly.

Once the coefficients of $g_x^m(x^m, y^m)$ and $g_y^m(x^0, y^0)$ are estimated we resample each image to the "master" coordinate system, using a 12 point raised cosine interpolation kernel, and form a raw interferogram by differencing the phase of each image to the phase of the "master".

4.2.3 Geometric Phase Correction

To account for the interferometric phase due to the curvature of the Earth's surface, the raw interferograms are first "flattened". "Flattening" involves correcting for the phase of each pixel as if the scattering surface were lying on a reference ellipsoid. Next, the phase due to the deviation of the real surface from the reference ellipsoid is estimated by transforming a digital elevation model (DEM) into the radar coordinate system, and removed from each pixel. Two error terms arise in this processing, look angle error and squint angle error. In the case of pixels with many distributed scatterers, the usual model for conventional interferometry, the look angle error is due almost entirely to error in the DEM, and is commonly referred to as DEM error. However, for PS pixels, there is also a contribution due to any deviation in the range position of the dominant scatterer from the center of the ground patch that is resolved by the pixel, which has the effect of shifting the phase center for the pixel. In conventional InSAR, squint angle error is commonly avoided by processing both images to a common squint angle. However, this lowers azimuthal resolution, which, as discussed in Section 4.2.1, we wish to maximize for PS pixels.

Look Angle Error

The phase estimated in these two steps, ϕ_θ, is proportional to the change in range, Δr, between the "master" and "slave" geometry,

$$\phi_\theta = -\frac{4\pi}{\lambda}\Delta r \tag{4.7}$$

where λ is the radar wavelength. The minus sign comes from the definition of the phase measured at the sensor being phase delay. From the geometry (Figure 2-2),

$$(r+\Delta r)^2 = r^2 + B^2 - 2rBcos\left(\frac{\pi}{2} - \theta + \omega\right) = r^2 + B^2 - 2rBsin(\theta - \omega) \tag{4.8}$$

where r is the range in the master geometry, B is the baseline length between the "slave" and "master" sensor position, θ is the look angle in the "master" geometry and ω is the angle between the baseline vector and the horizontal. Differentiating

and using Eq. 4.7 gives

$$\frac{\partial \phi_\theta}{\partial \theta} = \frac{4\pi}{\lambda} \frac{B cos(\theta - \omega) r}{(r + \Delta r)}. \tag{4.9}$$

Typically $\Delta r \ll r$ so this simplifies to

$$\frac{\partial \phi_\theta}{\partial \theta} \approx \frac{4\pi}{\lambda} B cos(\theta - \omega). \tag{4.10}$$

Ignoring any errors in $Bcos(\theta - \omega)$ which are included in an orbit error term (Eq. 4.15), the error, $\Delta\phi_\theta$, in our estimate of $\widehat{\phi}_\theta$ depends only on $\Delta\theta$, the error in our knowledge of θ,

$$\Delta\phi_\theta \approx \frac{4\pi}{\lambda} B cos(\theta - \omega) \Delta\theta = \frac{4\pi}{\lambda} B_\perp(\theta) \Delta\theta. \tag{4.11}$$

for small $\Delta\theta$. Here $B_\perp(\theta)$ is the perpendicular component of the baseline. From the geometry, $\Delta\theta$ is obviously dependent on the accuracy of the estimated height above the reference surface (Figure 2-2), but is also dependent on any difference in the position of the phase center within the pixel from that assumed in the "flattening" step. Specifically

$$\Delta\theta = \frac{\Delta h \ sin(\theta_i) + \xi \ cos(\theta_i)}{r} \tag{4.12}$$

where Δh is the error in height, ξ is the horizontal distance of the phase center from the middle of the pixel in range direction, and θ_i is the incidence angle. Thus, even if the DEM were 100% accurate, there could still be an error in θ due to both the lateral offset of the phase center itself and any variation in height due to this offset. Hence we refer to this term as the look angle error term, rather than the DEM error term as it is often referred to. In the case that we consider here, where carrier frequency does not vary between passes, the DEM error is indistinguishable from the error due to phase center uncertainty. With varying carrier frequency, separation of the two errors would be possible [*Colesanti et al.*, 2003b; *Kampes*, 2005]. The benefit would be more accurate positioning of the PS, although for most deformation studies, the positional accuracy of several meters that is already obtained is sufficient. The above-mentioned limitation of using varying carrier frequencies, that only the most point-like pixels remain persistent, would however apply.

As the look angle error term is estimated later in the PS processing, the accuracy

of the DEM is not usually important, although higher accuracy reduces the ambiguity in this estimation step, and thus is important in the case where only a few (< 12) interferograms are available.

Squint Angle Error

There is a similar error term due to the difference in squint angle between passes. SAR azimuth focusing assumes that the phase center of the pixel is in the center. The additional phase introduced if the phase center deviates from the pixel center in azimuth direction, by an amount η, cancels when the squint angle is the same for both the "master" and "slave" acquisition. When the squint angles differ an error term, $\Delta\phi_\vartheta$, arises where

$$\Delta\phi_\vartheta = \frac{2\pi}{v} F_{DC} \eta \tag{4.13}$$

where v is the sensor velocity (see *Kampes* [2005] for a derivation). In the data sets we have processed to this point, F_{DC}, the doppler baseline, is generally small and $\Delta\phi_\vartheta$ is expected to be less than 0.2 radians. Furthermore, F_{DC} is somewhat correlated with time. As deformation is also correlated with time, there is a danger that the phase due to deformation, which is often much larger, leaking into any estimate for $\Delta\phi_\vartheta$. We therefore do not attempt to estimate this term and, instead, treat it as noise.

4.2.4 Geocoding

Finally, we estimate the position of every pixel in a geocoded reference frame using the orbital parameters and the DEM. Theoretically, our estimates of position could be improved using various parameters estimated during processing, but for the purposes of most deformation modeling, positional accuracy to within several meters is usually sufficient.

4.3 PS Identification

We use a combination of amplitude and phase analysis to estimate the PS probability for each pixel in the series of interferograms we have formed. Initially, we analyze the

amplitude to select PS candidates. We then estimate the PS probability of each candidate pixel through phase analysis, which we successively refine in a series of iterations. Finally we include an optional phase analysis step to estimate the PS probability of the pixels that were not included in the initial amplitude-based selection.

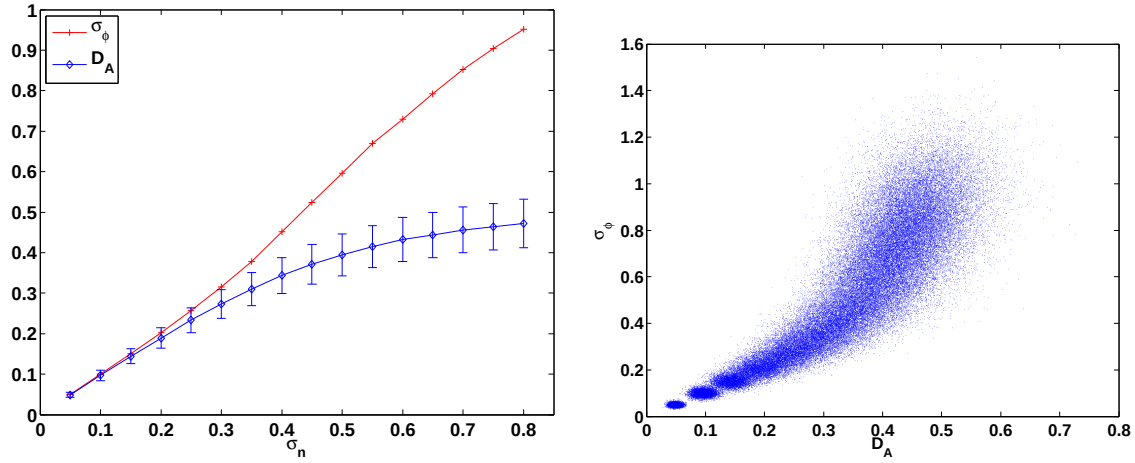

(a) (b)

Figure 4-2: Amplitude dispersion numerical simulation results. The signal model is $z_i = g + n_i$ $(i = 1, \cdots, 34)$. The value of g is fixed to 1 while the standard deviation, σ_n, of both the real and imaginary components of the noise, n_i, is incremented from 0.05 to 0.8. For each value of σ_n, we calculate 5000 estimates of $\widehat{\sigma}_\phi$ and $\widehat{D}_\mathcal{A}$. In (a) the mean values of $\widehat{\sigma}_\phi$ and $\widehat{D}_\mathcal{A}$ are plotted for each value of σ_n, as in *Ferretti et al.* [2001], with error bars for $\widehat{D}_\mathcal{A}$ representing one standard deviation. In (b) $\widehat{\sigma}_\phi$ and $\widehat{D}_\mathcal{A}$ are plotted as a scatterplot, for all values of σ_n.

4.3.1 Amplitude Analysis

Although it is the phase stability of a pixel that defines a PS, there are various nuisance terms included in the phase that make analysis of phase stability complex. However, these nuisance terms tend to have little effect on the amplitude of the return. As there is a statistical relationship between amplitude stability and phase stability, consideration of amplitude is useful both to reduce the number of pixels for phase analysis, and to better estimate the probability of a pixel being a PS, as discussed in Section 4.4.

This amplitude dispersion index, $D_{\mathcal{A}}$, is defined by *Ferretti et al.* [2001] as

$$D_{\mathcal{A}} \equiv \frac{\sigma_{\mathcal{A}}}{\mu_{\mathcal{A}}} \tag{4.14}$$

where $\sigma_{\mathcal{A}}$ and $\mu_{\mathcal{A}}$ are respectively the standard deviation and the mean of a series of amplitude values. *Ferretti et al.* [2001] show that for a constant signal and high signal to noise ratio (SNR), $D_{\mathcal{A}} \approx \sigma_{\phi}$, where σ_{ϕ} is the phase standard deviation. They plot the relationship using simulation, which we have repeated in Figure. 4-2. The model consists of a constant signal of amplitude 1, with additive noise selected from a complex circular Gaussian distribution with a characteristic standard deviation, σ_n, for both the real and imaginary components. This figure shows that, given 34 images, $\widehat{D}_{\mathcal{A}}$ is a reasonable proxy for σ_{ϕ}, for low values of σ_{ϕ}.

However, this figure might lead one to conclude that $\widehat{D}_{\mathcal{A}}$ is generally a better proxy for $\widehat{\sigma}_{\phi}$ than it really is, for two reasons. Firstly, although the error bars show the variability of $\widehat{D}_{\mathcal{A}}$ given a value of σ_n, it is the variability of σ_n given $\widehat{D}_{\mathcal{A}}$ that is required. Although this variability depends on the chosen distribution of σ_n, which is arbitrary here, we can get an idea of the variability of σ_n for any given value of $\widehat{D}_{\mathcal{A}}$ from the figure. For instance, given this simulated distribution of σ_n, at 68% confidence, $D_{\mathcal{A}} = 0.3$ indicates a range for σ_n of about 0.28 to 0.4. Secondly, error bars are not plotted for $\widehat{\sigma}_{\phi}$. Considering this error, the range of σ_n implies a range for $\widehat{\sigma}_{\phi}$ of about 0.25 to 0.54. Thus, even for a relatively small value of $\widehat{D}_{\mathcal{A}} = 0.3$, the variability in $\widehat{\sigma}_{\phi}$, that is phase stability, is rather large. An alternative way to view the relationship between $\widehat{D}_{\mathcal{A}}$ and $\widehat{\sigma}_{\phi}$ is by plotting the same data in a scatter plot as in Figure 4-2b, where the variability of $\widehat{\sigma}_{\phi}$ for any given value $D_{\mathcal{A}}$ is immediately apparent. It is also apparent that, although $D_{\mathcal{A}}$ tends to the theoretical limit for the Rayleigh distribution of $\sqrt{(4-\pi)/\pi} \simeq 0.523$, as SNR tends to zero [*Ferretti et al.*, 2001], estimated values of $\widehat{D}_{\mathcal{A}}$ from finite samples can be somewhat greater.

The actual distribution of $\widehat{D}_{\mathcal{A}}$ for any given data set depends on the real distribution of the noise in the data. In order to estimate sample noise distributions, we apply the model of signal plus circular Gaussian noise to real data. We simulate a distribution of $\widehat{D}_{\mathcal{A}}$ for a range of SNR values, and solve for the weighted sum of

individual SNR distributions that best fits the distribution of $\widehat{D}_{\mathcal{A}}$ in the data. We use a non-negative least-squares algorithm to determine the best-fitting weighting. We model data in this way for two examples, the first for 15 images acquired over Volcán Alcedo and the second for 24 images acquired over Mount St. Helens in Washington State. Initially we tried fitting the data for all values of $D_{\mathcal{A}}$, but found for higher values that the model always systematically underfit the data, so we only attempt to fit values of $\widehat{D}_{\mathcal{A}} < 0.5$ (Figure 4-3). The systematic misfit of the data implies that the model does not exactly reflect reality. This was also the conclusion of *Kampes* [2005] who analyzed data acquired over Berlin and found the mean value of $\widehat{D}_{\mathcal{A}}$ to be 0.56. As the maximum theoretical mean value of $\widehat{D}_{\mathcal{A}}$ is 0.523, it is clearly impossible to explain this distribution as the sum of distributions for different SNRs. The underlying assumption of this model is that any pixel can be characterized by fixed SNR in time. As we expect the SNR for some pixels to vary with time, it is not surprising that the model is unable to fit the data distribution exactly. However, for lower values of $\widehat{D}_{\mathcal{A}}$ the model appears feasible.

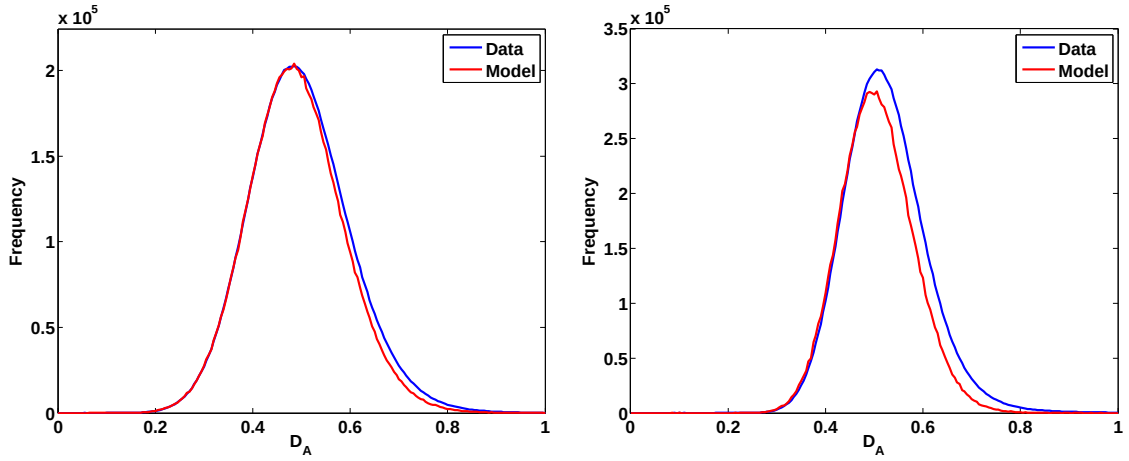

(a) Volcán Alcedo (b) Mount St. Helens

Figure 4-3: Distribution of amplitude dispersion values for two different data sets. Also plotted are the distributions predicted from the best-fitting model noise standard deviation distributions.

Given our model distributions of SNR, we can also estimate the distribution of σ_{ϕ}, as shown in Figure 4-4. If we take $\sigma_{\phi} \leq 0.6$ as indicative of phase stability [*Colesanti*

et al., 2003b], model values of σ_ϕ for the Mount St. Helens data set indicate that there are no stable scatterers at all, according to this definition of phase stability. For the Alcedo data set, the model values indicate that even choosing pixels with $D_\mathcal{A} < 0.25$ does not necessarily imply good phase stability. This is due to the low number of images in this case.

The phase analysis step of PS methods that rely on a functional model of temporal deformation to identify PS pixels requires an initial selection of pixels as PS candidates. These candidates should provide spatial coverage of at least 3 to 4 candidates/km^2 [*Colesanti et al.*, 2003b] and most of the candidates must be stable [*Kampes*, 2005]. Figure 4-5 shows, for the Alcedo data set, the percentage of area that meets the minimum candidate density requirement and the percentage of candidates that have good phase stability, for any chosen $D_\mathcal{A}$ threshold. If using $\widehat{D}_\mathcal{A}$ to pick the candidates, the density requirement pushes the $\widehat{D}_\mathcal{A}$ threshold value up and the stability requirement pushes it down. Hence, there is no value that satisfies both requirements for the Alcedo data set.

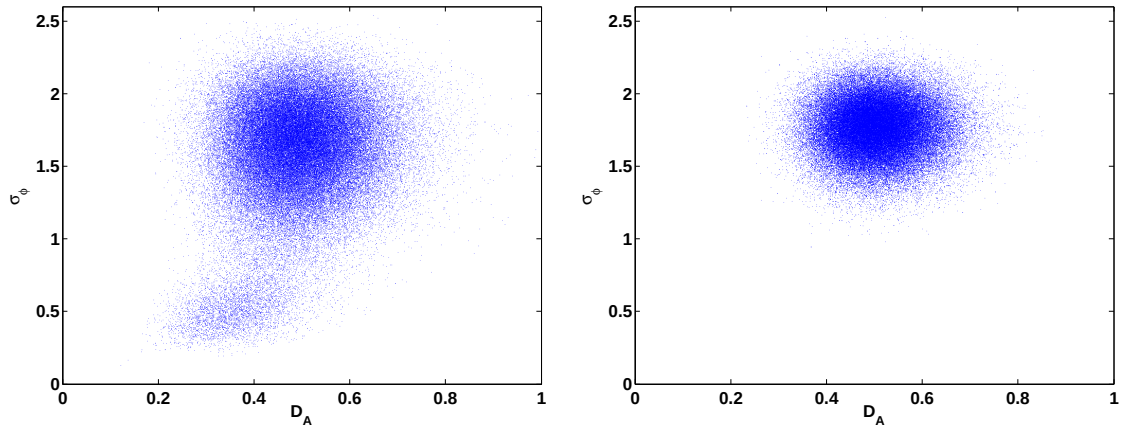

(a) Volcán Alcedo (b) Mount St. Helens

Figure 4-4: Scatter plots of amplitude dispersion vs. phase standard deviation for model distributions of noise standard deviation. The amplitude dispersion distributions predicted from the model distributions are shown in Figure 4-3.

The phase analysis step in StaMPS does not require that most PS candidates are in fact PS, so we are free to set $\widehat{D}_\mathcal{A}$ as high as we like. Our criterion for phase stability is also more relaxed than $\sigma_\phi \leq 0.6$, as we expect PS pixels in rural areas

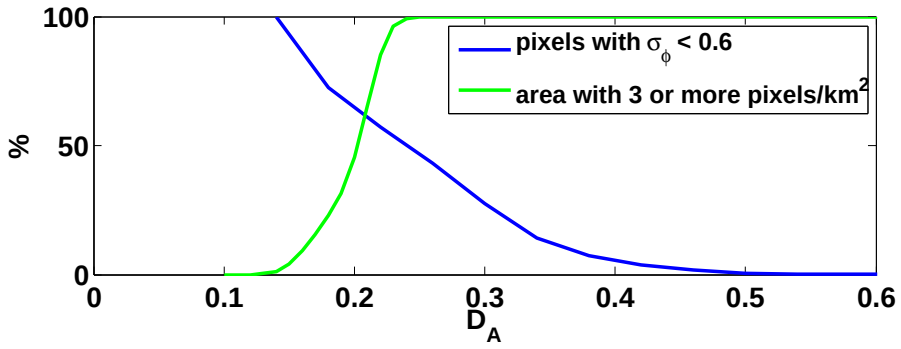

Figure 4-5: Percentage of high phase stability pixels ($\sigma_\phi \leq 0.6$) for different threshold values of $D_\mathcal{A}$, given our model distributions of noise standard deviation for data acquired over Volcán Alcedo.

to have lower SNR than those in urban areas. Our only requirement is that the signal be distinguishable from the noise, and on this basis we find PS even in the Mount St. Helens data set. In theory, we could run the phase analysis step with no $D_\mathcal{A}$ thresholding at all, but in practice computational times are greatly improved by thresholding. Typically we find that thresholding on $\widehat{D}_\mathcal{A} \leq 0.4$ reduces the data by an order of magnitude and includes most of the PS. There is an optional later step, described in Section 4.3.4, in which pixels above this threshold are also analyzed for phase stability.

4.3.2 Phase Analysis

Having selected a subset of pixels as PS candidates, we use phase analysis to estimate the PS probability for each of them. The wrapped phase, $\psi_{int,x,i}$, of the xth pixel in the ith "flattened" and topographically corrected interferogram can be written as the wrapped sum of 5 terms,

$$\psi_{int,x,i} = W\{\phi_{def,x,i} + \phi_{atm,x,i} + \Delta\phi_{orb,x,i} + \Delta\phi_{\theta,x,i} + \phi_{n,x,i}\} \tag{4.15}$$

where $\phi_{def,x,i}$ is the phase change due to movement of the pixel in the satellite line-of-sight (LOS) direction, $\Delta\phi_{\theta,x,i}$ is the residual phase due to look angle error, $\phi_{atm,x,i}$ is the phase due to the difference in atmospheric retardation between passes, $\Delta\phi_{orb,x,i}$

is the residual phase due to orbit inaccuracies, $\phi_{n,x,i}$ is a noise term due to variability in scattering, thermal noise, coregistration errors and uncertainty in the position of the phase center in azimuth and $W\{\cdot\}$ is the wrapping operator. The pixels we seek as PS are those where $|\phi_{n,x,i}|$ is small enough that it does not completely obscure the signal. As the phase is wrapped this must certainly generally be $< \pi$, but in order to correctly estimate the integer ambiguity in the number of wraps when estimating the spatially uncorrelated look angle error, $\Delta\theta_x^{nc}$ in Eq. 4.23, it must be even smaller in practice.

Variation in the first four terms of Eq. 4.15 dominates the noise term, making it difficult to identify which scatterers are persistent directly from the wrapped phase. Hence we estimate these four terms and subtract them, giving an estimate for $\widehat{\phi}_{n,x,i}$ which we can then assess statistically. We do this iteratively, refining our estimates each time, and generally find convergence after only a few iterations.

For crustal deformation studies, the deformation signal we are interested in is that due to deformation of the Earth's surface, which is correlated spatially. There could also be signal associated with the isolated movement of individual bright scatterers, but we are not interested in these movements and they can be considered noise. Variation in atmospheric retardation between passes is due mainly to variation in the total electron content (TEC) of the ionsphere and water vapor content of the troposphere. Both of these quantities are correlated spatially. Orbital errors are also correlated spatially in azimuth, and interferometric processing leads to spatial correlation of the residual orbit error term also in range. Finally, DEM error tends to be partly spatially correlated and this maps into the look angle error. Hence, estimating the spatially correlated part of $\psi_{int,x,i}$ provides an estimate for the first three terms plus part of the fourth term in Eq. 4.15. In Chapter 3 we achieved this by calculating the mean of surrounding pixels that are judged most likely to be PS. The number of pixels included in the mean is reduced with each iteration as confidence in ruling out pixels as PS increases. This method is, in effect, a crude low-pass filter implemented in the spatial domain and relies on knowing the length scale of the spatial correlation. While this method works fine in Long Valley, where the limiting factor on distance of spatial correlation is the atmospheric term, in areas with steeper

deformation gradients the deformation term can become the limiting factor, altering the length scale of correlation. A better approach is to apply a band-pass filtering method that adapts to any phase gradient present in the data itself. We implement this as an adaptive phase filter, applied in the frequency domain. Each pixel is first weighted by setting the amplitude in all interferograms to an estimate of the SNR for the pixel, which in the first iteration we estimate as $1/\widehat{D}_{\mathcal{A}}$. To enable use of the two-dimensional fast Fourier transform (2-D FFT) the complex phase is transformed to a grid with spacing over which little variation in phase is expected (typically 40 to 100 m) and a grid size of typically 32 x 32 or 64 x 64 cells, depending on over what distance we expect pixels to remain spatially correlated. Where multiple pixels fall in the same grid cell, their complex values are summed.

In subsequent iterations we can use the amplitude and our estimate of $\widehat{\phi}_{n,x,i}$ to estimate SNR. Figure 4-6 shows the relationship between signal, noise, amplitude and phase noise for a single pixel in a single image. Assuming that the amplitude of the signal, g_x, remains constant and that real and imaginary parts of the noise, $n_{R,x,i}$ and $n_{I,x,i}$ respectively, are characterized by a single Gaussian distribution, with zero mean and standard deviation $\sigma_{n,x}$, the SNR $= g_x/\sigma_{n,x}$. Our estimate of $\widehat{g}_x$ is simply

$$\widehat{g}_x = \frac{1}{N}\sum_{i=1}^{N} A_{x,i} cos\phi_{n,x,i} \tag{4.16}$$

which follows from the fact that $g_{x,i} = A_{x,i} cos\phi_{n,x,i} - n_{\|,x,i}$ where $n_{\|,x,i}$ is the signal parallel component of noise, the mean of which is zero. Our estimate for $\widehat{\sigma}^2_{n,x}$ is given by

$$\widehat{\sigma}^2_{n,x} = \frac{\sum_{i=1}^{N}(n^2_{I,x,i} + n^2_{R,x,i})}{2N} = \frac{\sum_{i=1}^{N}(A^2_{x,i} sin^2\phi_{n,x,i} + (A_{x,i} cos\phi_{n,x,i} - g_x)^2)}{2N}. \tag{4.17}$$

Substituting for g_x with $\widehat{g}_x$ gives

$$\widehat{\sigma}^2_{n,x} = \frac{1}{2}\left[\frac{\sum_{i=1}^{N} A^2_{x,i}}{N} - \left(\frac{\sum_{i=1}^{N} A_{x,i} cos\phi_{n,x,i}}{N}\right)^2\right]. \tag{4.18}$$

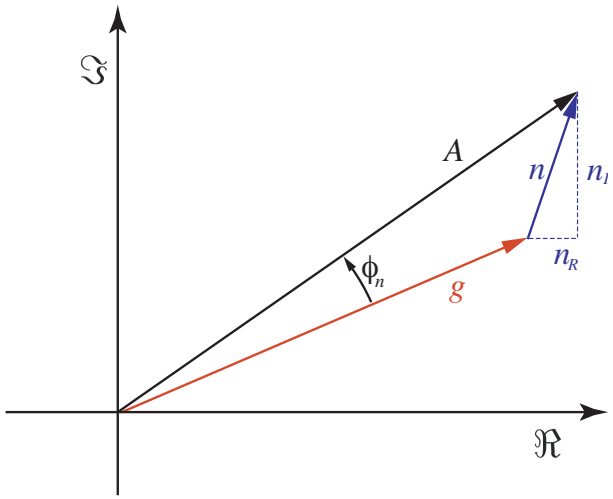

Figure 4-6: Model for pixel amplitude, A. The signal is assumed to have constant amplitude, g. The real and imaginary components of the noise, n_R and n_I, are characterized by the same Gaussian distribution.

We experimented with other weight selection methods. For example, we can weight each pixel based on the probability that it is persistent. Empirically we find that setting the amplitude to $1/[P(x \in PS)]^2$, where $P(x \in PS)$ is the probability that the pixel is a PS (see Section 4.3.3), often gives better results than weighting with the SNR, i.e., more PS pixels are found.

The adaptive part of the filter determines the pass band based on the dominant frequencies present in the phase of the pixels themselves. The response is calculated as

$$H(x, y) = |Z(x, y)| \tag{4.19}$$

where Z is the smoothed intensity of the 2-D FFT [*Goldstein and Werner*, 1998]. We smooth the intensity by convolution with a 7 x 7 pixel Gaussian window. We combine the adaptive phase filter response, $H(x, y)$, with a narrow low-pass filter response, $L(x, y)$, to form the new filter response,

$$G(x, y) = L(x, y) + \beta \left(\frac{H(x, y)}{\bar{H}(x, y)} - 1 \right)^{\alpha} \tag{4.20}$$

where $L(x, y)$ is a 5th order Butterworth filter, with a typical cutoff wavelength of

800 m, and $\bar{H}(x,y)$ is the median value of $H(x,y)$. α and β are adjustable weighting parameters, typical values being 1 and 0.3 respectively.

The filtered phase value, $\widetilde{\psi}_{int,x,i}$, is a wrapped estimate of the spatially correlated parts of each of the terms on the RHS of Eq. 4.15, so subtracting $\widetilde{\psi}_{int,x,i}$ from $\psi_{int,x,i}$ and re-wrapping gives

$$W\{\psi_{int,x,i} - \widetilde{\psi}_{int,x,i}\} = W\{\phi^{nc}_{def,x,i} + \phi^{nc}_{atm,x,i} + \Delta\phi^{nc}_{orb,x,i} + \Delta\phi^{nc}_{\theta,x,i} + \phi^{nc}_{n,x,i}\} \quad (4.21)$$

where ϕ^{nc} denotes the non-spatially correlated part of ϕ. We expect $\phi^{nc}_{def,x,i}$, $\phi^{nc}_{atm,x,i}$ and $\Delta\phi^{nc}_{orb,x,i}$ to be small as most of their power lies at longer wavelengths, so replacing their sum with $\delta_{x,i}$ in Eq. 4.21 gives

$$W\{\psi_{int,x,i} - \widetilde{\psi}_{int,x,i}\} = W\{\Delta\phi^{nc}_{\theta,x,i} + \phi^{nc}_{n,x,i} + \delta_{x,i}\}. \quad (4.22)$$

Eq. 4.11 describes an approximate linear relationship between $\Delta\phi_{\theta,x,i}$ and $\Delta\theta_x$. As long as $\Delta\phi^{nc}_{\theta,x,i}$ contains approximately the same frequency components for all i, it follows that the same approximate relationship holds between $\Delta\phi^{nc}_{\theta,x,i}$ and $\Delta\theta^{nc}_x$. Substituting for $\Delta\phi^{nc}_{\theta,x,i}$ in Eq. 4.22 gives

$$W\{\psi_{int,x,i} - \widetilde{\psi}_{int,x,i}\} \approx W\left\{\frac{4\pi}{\lambda}B_{\perp,x,i}\Delta\theta^{nc}_x + \phi^{nc}_{n,x,i} + \delta_{x,i}\right\}. \quad (4.23)$$

Becasue $B_{\perp,x,i}$ is not expected to be correlated with $\phi^{nc}_{n,x,i}$ or $\delta_{x,i}$, we can estimate $\Delta\widehat{\theta}^{nc}_x$ in a least-squares sense. The contribution from the "master" image to $\phi^{nc}_{n,x,i} + \delta_{x,i}$ will be present in every interferogram, causing a constant offset, $\phi^{m,nc}_x$, that we must also resolve in our least-squares inversion. Since the phase is wrapped, the inversion is not linear and so we implement the inversion as a rough search of parameter space, followed by a linear inversion to estimate the best-fitting model in the region of the rough estimate. We typically limit the rough search to values of $\Delta\widehat{\theta}^{nc}$ equivalent to ± 10 m of height error and in increments such that the range of $\Delta\widehat{\phi}^{nc}_{\theta,x}$ increases by $\pi/4$ (Figure 4-7). The inversion could also be implemented using the least-squares

ambiguity decorrelation (LAMBDA) method, initially developed for fast GPS double-difference integer ambiguity estimation [*Teunissen*, 1995] and adapted for InSAR data by *Kampes* [2005]. However, we find that as implemented, this is not a time limiting step.

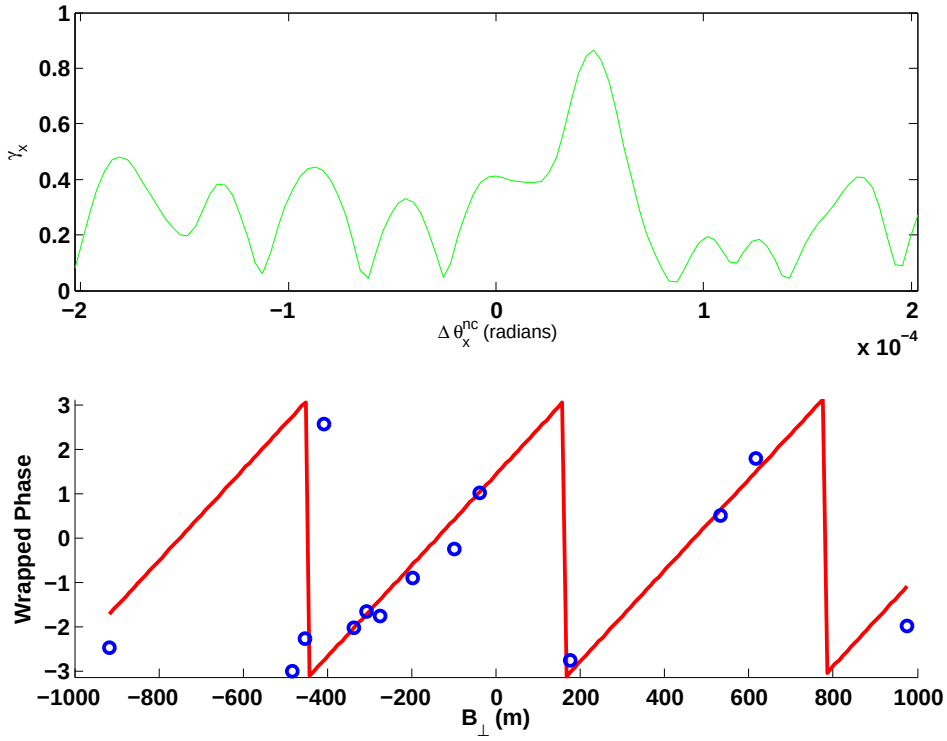

Figure 4-7: An example parameter space search for look angle error, $\Delta\theta_x^{nc}$, for a PS pixel in the Alcedo descending orbit data set (see Section 4.6). The plot above shows the goodness of fit for trial values of $\Delta\theta_x^{nc}$. The plot below shows a comparison between the data (blue circles) and phase values predicted by the value of $\Delta\theta_x^{nc}$ with maximum γ_x (red line).

From our estimate for $\Delta\widehat{\theta}_x^{nc}$ we derive $\Delta\widehat{\phi}_{\theta,x,i}^{nc}$ which we subtract from Eq. 4.22 to give

$$W\{\psi_{int,x,i} - \widetilde{\psi}_{int,x,i} - \Delta\widehat{\phi}_{\theta,x,i}^{nc}\} = W\{\phi_{n,x,i}^{nc} + \delta'_{x,i}\} \tag{4.24}$$

where $\delta'_{x,i} = \delta_{x,i} + \Delta\phi_{\theta,x,i}^{nc} - \Delta\widehat{\phi}_{\theta,x,i}^{nc}$.

We define a measure of the variation of this residual phase for a pixel as

$$\gamma_x = \frac{1}{N}\left|\sum_{i=1}^{N}\exp\{j(\psi_{int,x,i} - \widetilde{\psi}_{int,x,i} - \Delta\widehat{\phi}^{nc}_{\theta,x,i})\}\right| \tag{4.25}$$

where N is the number of interferograms and j is $\sqrt{-1}$. Assuming that $\phi_{n,x,i} \approx \phi^{nc}_{n,x,i}$ and $\delta_{x,i} \approx 0$, γ_x is a measure of the phase noise level and an indicator of whether the pixel is a PS. The measure γ_x is similar to the magnitude of coherence, except amplitude is not included as we want to give every image equal weight. A pixel that is bright in one image and dark with random phase in all other images would have high coherence if amplitude were included whereas in reality it would not be a good PS.

4.3.3 PS Probability

In general we expect a correlation between γ_x and the probability that pixel x is a PS. By binning and normalizing the values of γ_x we can estimate the probability density of γ_x, $p(\gamma_x)$. We treat our population of pixels as the union of two populations, one containing only PS pixels and the other containing only non-PS pixels, $p(\gamma_x)$ is, then, a weighted sum of the probability density for the PS pixels, $p_{PS}(\gamma_x)$, and the probability density for the non-PS pixels, $p_R(\gamma_x)$ (see Figure 4-8), i.e.,

$$p(\gamma_x) = \alpha p_{PS}(\gamma_x) + (1-\alpha)p_R(\gamma_x) \tag{4.26}$$

where $0 \leq \alpha \leq 1$. In order to derive $p_R(\gamma_x)$, we simulate 10^6 pseudo-pixels with random phase, i.e., $W\{\psi_{x,i} - \widetilde{\psi}_{x,i}\} = exp(jR)$, where R is a random variable in the interval $[-\pi, \pi]$, and follow the steps described above to arrive at a value of γ_x for each pseudo-pixel. We bin these values and normalize the distribution to obtain an estimate for $p_R(\gamma_x)$. For low values of γ_x, i.e., < 0.3, $p_{PS}(\gamma_x) \approx 0$ which implies

$$\int_0^{0.3} p(\gamma_x)\, d\gamma_x = (1-\alpha)\int_0^{0.3} p_R(\gamma_x)\, d\gamma_x. \tag{4.27}$$

We use the data to evaluate the integral on the left-hand side and the simulation to evaluate the integral on the right- hand side. Thus we are able to estimate a conservative value of α. For pixel x, the probability that it is a PS is

$$P(x \in PS) = 1 - \frac{(1-\alpha)p_R(\gamma_x)}{p(\gamma_x)}. \tag{4.28}$$

In practice, due to the presence of noise, the function $p_R(\gamma_x)/p(\gamma_x)$ may not be monotonically decreasing as expected, so we smooth it first by convolution with a 7 point Gaussian window.

4.3.4 Pixels With High Amplitude Dispersion

We expect that some pixels with high $\widehat{D}_{\mathcal{A}}$, which were rejected by our initial thresholding described in Section 4.3.1, will have stable phase, although the proportion will be small (see Figure 4-5). Once the low-$D_{\mathcal{A}}$ pixels have been processed, we include an optional step to process the high-$D_{\mathcal{A}}$ pixels, using the filtered phase of the low-$D_{\mathcal{A}}$ pixels to calculate $\widetilde{\psi}_{int,x,i}$, and proceeding from Eq. 4.21 to calculate γ_x. We then use the thresholding function already calculated in Section 4.4 to select PS from these high-$D_{\mathcal{A}}$ pixels.

4.4 PS Selection

Once we have converged on estimates for the PS probability of each pixel, we select those most likely to be PS, with a threshold determined by the fraction of false positives we deem acceptable. We also seek to identify pixels that persist only in certain interferograms and those that are dominated by scatterers in adjacent PS pixels, and reject them.

After every iteration we calculate the root-mean-square change in γ_x. Once this falls below some threshold, we assume convergence of our solution. We find empirically that a threshold of $3x10^{-2}$ suffices. We then select pixels based on the PS probability. As there is a correlation between amplitude variance and phase stability (see Section 4.3.1), we can calculate the probability more accurately by considering

the amplitude dispersion of the pixels, $\widehat{D}_{\mathcal{A},x}$, as well as γ_x. We bin the pixels by $\widehat{D}_{\mathcal{A},x}$, ensuring there are at least 10^4 pixels in every bin, resulting in a number of data probability distributions, $p(\gamma_x, \widehat{D}_{\mathcal{A},x})$. For each distribution, $p(\gamma_x, \widehat{D}_{\mathcal{A},x})$, we estimate $\alpha(\widehat{D}_{\mathcal{A},x})$ as decribed in Section 4.3.3. If only pixels with γ_x above a threshold value, $\gamma^{thresh}(\widehat{D}_{\mathcal{A},x})$, are selected, the number of those pixels that are non-PS pixels is given by

$$(1 - \alpha(\widehat{D}_{\mathcal{A},x})) \int_{\gamma^{thresh}}^{1} p_R(\gamma_x)\, d\gamma_x \tag{4.29}$$

We choose $\gamma^{thresh}(\widehat{D}_{\mathcal{A},x})$ such that the fraction of non-PS pixels to the total number of chosen pixels is acceptable for our particular application, i.e.,

$$\frac{(1 - \alpha(\widehat{D}_{\mathcal{A},x})) \int_{\gamma^{thresh}}^{1} p_R(\gamma_x)\, d\gamma_x}{\int_{\gamma^{thresh}}^{1} p(\gamma_x, \widehat{D}_{\mathcal{A},x})\, d\gamma_x} = q, \tag{4.30}$$

where q is the maximum fraction of all the selected pixels that we will accept being non-PS pixels (false positives). As indicated in Figure 4-2, we generally expect γ_x, which is a measure of the phase stability, to decrease with increasing $\widehat{D}_{\mathcal{A},x}$. This implies that as $\widehat{D}_{\mathcal{A},x}$ increases, $p(\gamma_x, \widehat{D}_{\mathcal{A},x})$ will skew more to lower values of γ_x. The net effect on $\gamma^{thresh}(\widehat{D}_{\mathcal{A},x})$ is to increase with increasing $\widehat{D}_{\mathcal{A}}$. Empirically we find that the relationship is approximately linear, i.e. $\gamma^{thresh} = \kappa \widehat{D}_{\mathcal{A}}$ where κ is a constant. We find the best-fitting κ by least-squares inversion and select pixels for which $\gamma_x > \kappa \widehat{D}_{\mathcal{A},x}$ as our PS.

4.4.1 Partially Persistent Scatterers

The stability of a pixel may change during the period covered by the data set, for example, if a dominant scatterer is added or removed. Therefore, a pixel may display a period of good phase stability, preceded and/or followed by a period of low stability. A more subtle issue arises when the scattering characteristics of a dominant scatterer are altered, but the scatterer remains dominant. The pixel would then have two periods of phase stability, although one of the periods would be decorrelated with respect to the "master" image. In both cases the pixel may still be identified if its

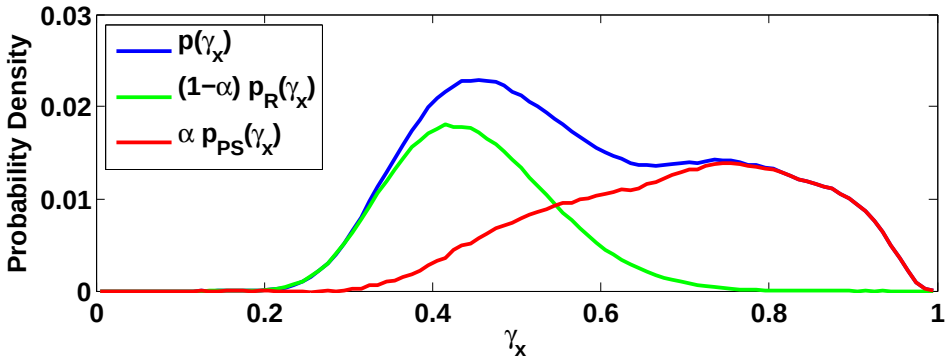

Figure 4-8: An example probability density for γ_x, shown in blue, for a given range of $\widehat{D}_{\mathcal{A},x}$. The probability density is the sum of two scaled probability densities, that for PS pixels, shown in red, and that for non-PS pixels, shown in green.

mean variance is small enough, but in some images the phase will be dominated by noise. Furthermore, if the phase characteristics of whole areas of an image change between two passes, e.g., if a field is plowed or there is a new lava flow, the signal of all PS selected in that area will be dominated by noise in some of the images.

It would be possible to keep these pixels only for those images where they provide useful deformation signal, and reject them for all other images. However, the three-dimensional phase unwrapping algorithms that we have developed and describe in Chapter 5 require pixels that persist through all images. We expect to relax this requirement in future phase unwrapping algorithms. To avoid picking these pixels, we include an optional step to estimate the variance of γ_x for each pixel using the bootstrap percentile method [*Efron and Tibshirani*, 1986] with 1000 iterations, and drop pixels with standard deviation over a defined threshold, a typical value being 0.1.

4.4.2 Multiple Pixel PS

A Scatterer that is bright can dominate pixels other than the pixel corresponding to its physical location. The error in look angle and squint angle due to the offset of the pixel from the physical location usually results in these pixels not being selected as PS. However, the slight oversampling of the resolution cells can cause pixels immediately

adjacent to the PS pixel to be dominated by the same scatterer where the error may be sufficiently small that the pixel appears stable. To avoid picking these pixels, we assume that adjacent pixels selected as PS are due to the same dominant scatterer. As we expect the pixel that corresponds to the physical location to have the highest SNR, for groups of adjacent stable pixels we select as the PS only the pixel with the highest value of γ_x.

4.5 Displacement Estimation

Once we have selected our PS, we discard all other pixels and return to the original wrapped interferogram phase, $\psi_{int,x,i}$ (Eq. 4.15). Now, the phase must be unwrapped and other nuisance terms estimated in order to retrieve the phase due to deformation, $\phi_{def,x,i}$.

4.5.1 Phase Unwrapping

The subject of phase unwrapping is discussed in detail in Chapter 5. Here we describe only how we manipulate the wrapped interferogram phase to provide a data set that is more optimal for unwrapping.

If no assumptions are to be made about the underlying phase signal, accurate unwrapping is only possible when the absolute difference in phase between neighboring PS is generally less than π. For the spatially correlated part of the signal, this will be true as long as the spatial sampling of the signal by the PS is sufficiently dense. Even when the sampling density is high enough, the contribution to the absolute difference in phase between neighboring PS can still be greater than π due to the non-spatially correlated part of the signal. The most significant contribution to this part is the non-spatially correlated part of the look angle error, $\Delta\phi_\theta^{nc}$, for which we already have an estimate. We also have an estimate for the contribution of the "master" to the non-spatially correlated part of the signal, $\widehat{\phi}_x^{m,nc}$. We therefore subtract our estimates for these two terms before unwrapping, yielding

$$W\{\psi_{int,x,i} - \Delta\widehat{\phi}_{\theta,x,i}^{nc} - \widehat{\phi}_x^{m,nc}\} = W\{\phi_{def,x,i} + \phi_{atm,x,i} + \Delta\phi_{orb,x,i} + \Delta\phi_{\theta,x,i}^{corr} + \Delta\phi_{n,x,i}\} \quad (4.31)$$

where $\Delta\phi^{corr}_{\theta,x,i}$ is the correlated part of $\Delta\phi_{\theta,x,i}$ and $\Delta\phi_{n,x,i}$ is the residual spatially uncorrelated noise term, $\phi_{n,x,i} - \widehat{\phi}^{m,nc}_{x}$.

One strategy for unwrapping this phase is to unwrap spatially the phase difference between each neighboring (in time) pair of interferograms, as done in Chapter 3. However, as we actually have three dimensions of phase data, two in space and one in time, more reliable results can generally be obtained using one of the three-dimensional unwrapping algorithms described in Chapter 5. Whichever algorithm is chosen, the results of unwrapping can be summarized as

$$\phi_{uw,x,i} = \phi_{def,x,i} + \phi_{atm,x,i} + \Delta\phi_{orb,x,i} + \Delta\phi^{corr}_{\theta,x,i} + \Delta\phi_{n,x,i} + 2k_{x,i}\pi \tag{4.32}$$

where $\phi_{uw,x,i}$ is the unwrapped value of $W\{\psi_{int,x,i} - \Delta\widehat{\phi}^{nc}_{\theta,x,i} - \widehat{\phi}^{m,nc}_{x}\}$ and $k_{x,i}$ is the remaining unknown integer ambiguity. If the unwrapping was generally accurate, $k_{x,i}$ will be the same integer for most x in any given interferogram i.

4.5.2 Spatially Correlated Nuisance Terms

After unwrapping, several terms remain in Eq. 4.32 that mask $\phi_{def,x,i}$. The spatially uncorrelated part of these nuisance terms can be modeled as noise in any subsequent deformation modeling, but the spatially correlated parts can bias the results, so we seek to estimate and subtract them. We separate the spatially correlated part of the nuisance terms into the part that is correlated in time and the part that is expected not to be. The former consists of the master contributions to $\phi_{atm,x,i}$ and $\Delta\phi_{orb,x,i}$, which are present in every interferogram, and the latter consists of the remaining spatially correlated terms. We estimate both parts separately using a combination of temporal and spatial filtering as described below.

In order to estimate the "master" contributions to the spatially correlated phase we low-pass filter in time. Because of the $2k_{x,i}\pi$ term, absolute values of $\phi_{uw,x,i}$ are essentially decorrelated in time and we are not able to apply a temporal filter directly. However, $k_{x,i}$ is identical for most neighboring PS pixels, so we calculate the phase differences between neighboring PS. In most cases this cancels the $2k_{x,i}\pi$ term, and we can filter these instead. We first form a spatial network connecting all the PS

using Delaunay triangulation. In each interferogram we difference $\phi_{uw,x,i}$ between PS, clockwise, around each triangle. For each PS pair, we low-pass filter the differenced phase in time by convolution with a Gaussian function. The width of the Gaussian is chosen to be less than the time over which deformation rate is expected to vary, in order to preserve the deformation phase.

$$\mathcal{L}^T\{\Delta_{x_1}^{x_2}\phi_{uw,i}\} \approx \Delta_{x_1}^{x_2}\phi_{def,i} - \Delta_{x_1}^{x_2}\phi_{atm}^m - \Delta_{x_1}^{x_2}\Delta\phi_{orb}^m \tag{4.33}$$

where $\mathcal{L}^T\{\cdot\}$ is the low-pass filter operator, $\Delta_{x_1}^{x_2}$ is the phase differencing operator between x_2 and x_1 and superscript m indicates the "master" contribution to these terms. Evaluating $\mathcal{L}^T\{\Delta_{x_1}^{x_2}\phi_{uw,i}\}$ at the "master" time, when $\phi_{def,x} = 0$ for all x, therefore gives an estimate for $\Delta_{x_1}^{x_2}\widehat{\phi}_{atm}^m + \Delta_{x_1}^{x_2}\Delta\widehat{\phi}_{orb}^m$. The estimate, $\widehat{\phi}_{atm,x}^m + \Delta\widehat{\phi}_{orb,x}^m$ with respect to an arbitrary reference PS is retrieved by least-squares inversion.

In order to estimate the "slave" contributions to the spatially correlated phase, which are expected not to be temporally correlated, we high-pass filter in time. We achieve this by subtracting $\mathcal{L}^T\{\Delta_{x_1}^{x_2}\phi_{uw,i}\}$ from $\Delta_{x_1}^{x_2}\phi_{uw,i}$ giving

$$\Delta_{x_1}^{x_2}\phi_{uw,i} - \mathcal{L}^T\{\Delta_{x_1}^{x_2}\phi_{uw,i}\} \approx \Delta_{x_1}^{x_2}\phi_{atm,i}^s + \Delta_{x_1}^{x_2}\Delta\phi_{orb,i}^s + \Delta_{x_1}^{x_2}\Delta\phi_{\theta,i}^{corr} + \Delta_{x_1}^{x_2}\Delta\phi_{n,i} \tag{4.34}$$

where superscript s indicates the "slave" contribution to these terms. For each interferogram the high-pass filtered signal for each PS, with respect to an arbitrary reference PS, is retrieved from $\Delta_{x_1}^{x_2}\phi_{uw,i} - \mathcal{L}^T\{\Delta_{x_1}^{x_2}\phi_{uw,i}\}$ by least-squares inversion,

$$[\Delta_{x_1}^{x_2}]^{-1}\{\Delta_{x_1}^{x_2}\phi_{uw,i} - \mathcal{L}^T\{\Delta_{x_1}^{x_2}\phi_{uw,i}\}\} \approx \phi_{atm,x,i}^s + \Delta\phi_{orb,x,i}^s + \Delta\phi_{\theta,x,i}^{corr} + \Delta\phi_{n,x,i} \tag{4.35}$$

where $[\Delta_{x_1}^{x_2}]^{-1}$ is the inverse phase differencing operator. We then low-pass filter this phase spatially, for each interferogram, by convolution with a two-dimensional Gaussian function. We wish to include all of the signal except for that localized to individual PS pixels, so we set the width of the Gaussian to be narrow, typically 50 m . The output from the convolution provides our estimate of $\widehat{\phi}_{atm,x,i}^s + \Delta\widehat{\phi}_{orb,x,i}^s + \Delta\widehat{\phi}_{\theta,x,i}^{corr}$.

Rearranging Eq. 4.32 and substituting in the terms estimated in this section gives

$$\phi_{def,x,i} \approx \phi_{uw,x,i} + \widehat{\phi}^{m}_{atm,x} - \widehat{\phi}^{s}_{atm,x,i} + \Delta\widehat{\phi}^{m}_{orb,x} - \Delta\widehat{\phi}^{s}_{orb,x,i} - \Delta\widehat{\phi}^{corr}_{\theta,x,i} - \Delta\phi_{n,x,i} - 2k_{x,i}\pi \quad (4.36)$$

In practice it is possible that the spatially correlated nuisance terms may also be correlated temporally, in which case they will not be correctly estimated by the procedure above. For the atmospheric term, this may be the case in regions where tropospheric moisture content is seasonally variable, such as in coastal areas where fog is more prevalent at certain times of the year. Further processing is required if this is suspected to be the case. For the orbit error term, we have found with Radarsat-1 data that values can be large and, apparently by chance, correlated in time. If this appears to be the case, we estimate phase ramps in interferograms where the orbit error term is visible, and remove them, before estimating the other spatially correlated terms.

4.6 Application to Volcán Alcedo

We analyzed ERS-1 and ERS-2 data acquired over Volcan Alcedo between June 1992 and January 2001 (see Tables 4.1 and 4.2), using StaMPS. We processed 15 descending track images and 14 ascending track images, giving a total of 27 interferograms referenced to February 2000 in the descending case and January 2000 in the ascending case (Figure 4-9). We use Shuttle Radar Topography Mission (SRTM) 3-arc second data as the reference DEM. The specific parameters we used in the processing are detailed in Table 4.3. The broad distribution of PS pixels is similar in both the descending and ascending cases, although the positions of individual PS pixels are not necessarily identical (Figures 4-10 and 4-11). In the ascending data, the distribution of perpendicular baselines, $B_{\perp}$, falls into two distinct clusters separated by 707 m. Coregistration between the two clusters is challenging, leading to more error in $\phi_{n,x,i}$ from misregistration than in the descending case. The Doppler centroid baseline is also generally larger in the ascending case, leading to a greater noise contribution from background scatterers. Note also that more long wavelength atmospheric signal

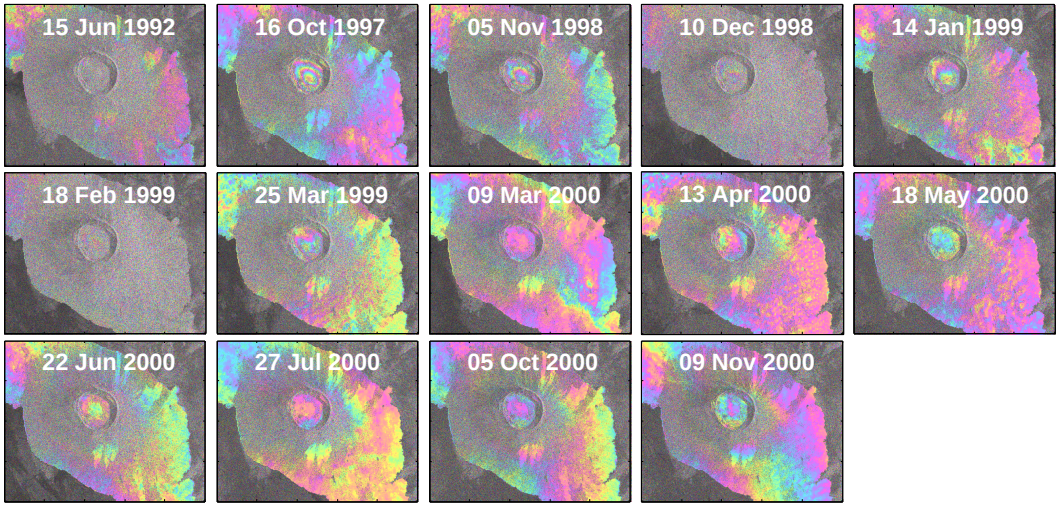

(a) Descending Orbit

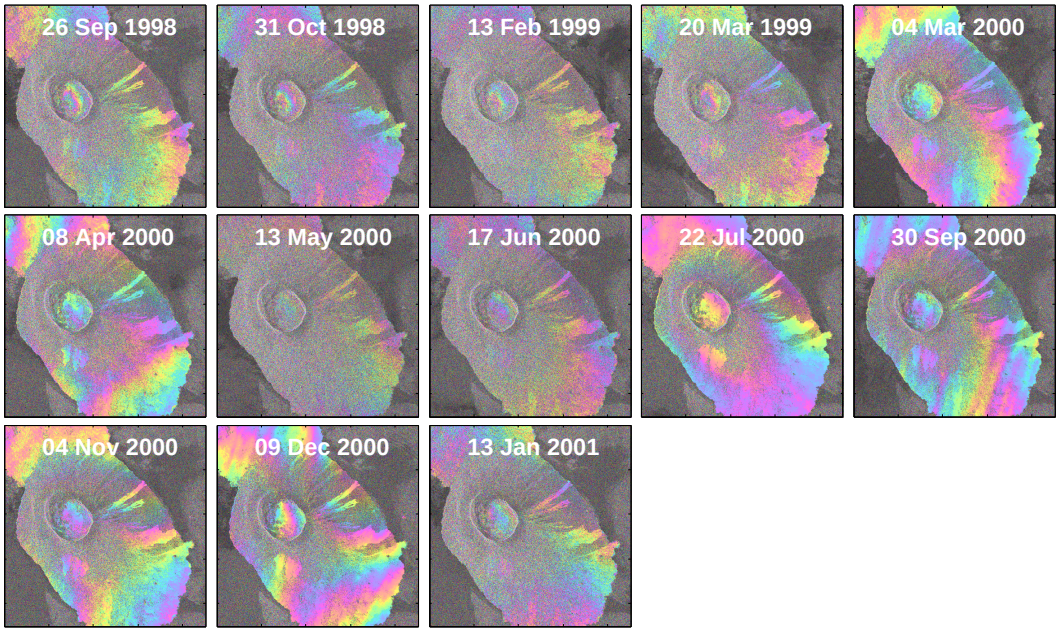

(b) Ascending Orbit

Figure 4-9: Wrapped interferograms from descending and ascending orbit data acquired over Alcedo, with 4 looks taken in range and 20 in azimuth. The "master" acquisition date is 03 Feb 2000 for the descending interferograms and 29 Jan 200 for the ascending interferograms. Each color fringe represents 2.8 cm of displacmemt in the LOS.

is present in the ascending data than the descending data, presumably related to the difference in acquisition time which is 10.45 pm, local time, for the ascending orbit as opposed to 10.23 am for the descending orbit.

Orbit	Date	Sensor	$B_\perp$ [m]	f_{DC} [Hz]
4794	1992-06-15	ERS-1	616	-301.24
13020	1997-10-16	ERS-2	176	-677.10
18531	1998-11-05	ERS-2	533	-574.81
19032	1998-12-10	ERS-2	-917	-633.35
19533	1999-01-14	ERS-2	-484	-574.48
20034	1999-02-18	ERS-2	976	-447.77
20535	1999-03-25	ERS-2	-407	-472.20
25044	2000-02-03	ERS-2	0	-551.03
25545	2000-03-09	ERS-2	-198	-421.53
26046	2000-04-13	ERS-2	-274	-684.07
26547	2000-05-18	ERS-2	-308	-594.90
27048	2000-06-22	ERS-2	-453	-746.82
27549	2000-07-27	ERS-2	-39	-667.34
28551	2000-10-05	ERS-2	-337	-883.46
29052	2000-11-09	ERS-2	-99	-908.65

Table 4.1: Descending orbit data processed for Alcedo (track 140, frame 3620). $B_\perp$ is relative to the master acquisition, 2000-02-03.

A period of asymmetric deformation occured within the caldera between June 1992 and October 1997 which is visible in the interferogram of *Amelung et al.* [2000]. Although this event is clear in the wrapped phase of the PS pixels in an interferogram covering this time period (Figure 4-12), the spatial sampling of the PS is not high enough everywhere to unwrap the signal associated with this event. The spatial pattern of the wrapped phase is, however, consistent with a trapdoor faulting event similar to those that have occurred on Sierra Negra [*Amelung et al.*, 2000; *Chadwick et al.*, 2006], another volcano also located on Isla Isabela. In the case of Alcedo the fault appears to be located in the southwest of the caldera, striking approximately northwest-southeast. For all subsequent acquisitions, which cover the period October 1997 to January 2001, we are able to extract and unwrap the deformation signal (Figures 4-10 and 4-11).

Orbit	Date	Sensor	$B_\perp$ [m]	f_{DC} [Hz]
17951	1998-09-26	ERS-2	-650	29.46
18452	1998-10-31	ERS-2	-707	-92.33
19955	1999-02-13	ERS-2	-854	-71.67
20456	1999-03-20	ERS-2	-707	-25.25
24965	2000-01-29	ERS-2	0	25.39
25466	2000-03-04	ERS-2	298	-184.15
25967	2000-04-08	ERS-2	387	-193.15
26468	2000-05-13	ERS-2	-900	592.97
26969	2000-06-17	ERS-2	-733	500.57
27470	2000-07-22	ERS-2	33	274.85
28472	2000-09-30	ERS-2	122	517.95
28973	2000-11-04	ERS-2	370	143.69
29474	2000-12-09	ERS-2	57	446.37
29975	2001-01-13	ERS-2	-726	-176.83

Table 4.2: Ascending orbit data processed for Alcedo (track 61, frame 7176). $B_\perp$ is relative to the master acquisition, 2000-01-29.

4.6.1 Modeling

Our results show a dominant deflation signal for the entire 1997 to 2001 period, largely confined within the caldera. The rate of deflation appears to be approximately constant over this time period, and can be observed in the change in maximum LOS displacement in the descending data (Figure 4-13a). There is also a discontinuity in the displacement rates following the trend of a break in topography on the west side of the caldera. The rate of deformation to the west of this discontinuity also appears be approximately constant as observed in the change in LOS displacement between the west side and east side of the caldera in the ascending data (Figure 4-13b). Both modes of deformation appear to be constant in rate, and we calculate the mean displacement rates for both the descending and ascending data. For the descending data we are able to reference the rates to the mean signal at the coasts (Figure 4-14a), which we assume to be moving at plate velocity. For the ascending data, unwrapping between the caldera and the coast is unreliable due to the higher phase noise. Therefore, we analyze only the data within the caldera and reference the rates to the east side of the caldera (Figure 4-14b).

Parameter	Value
DEM	SRTM 3-arc second
Maximum DEM Error	10
Combined phase filter grid cell size	40 m
Combined phase filter grid size	64 x 64
Combined phase filter low-pass filter cutoff	800 m
Combined phase filter α	1
Combined phase filter β	0.3
Allowable fraction of non-PS selected as PS	1%
Partial PS pixels rejected?	No
Spatially correlated filtering time window	180 days
Spatially correlated filtering minimum wavelength	50 m
Unwrapping algorithm	pseudo-3-D (Chapter 5)
Unwrapping grid cell size	100 m
Unwrapping α	8

Table 4.3: Parameters used in the StaMPS processing of Alcedo data.

PS on the west side of the caldera that seem most affected by the second mode of deformation are located on the inner slope of the caldera (see topography in Figure 4-14b). Relative to the displacement expected from the deflationary signal alone, in the ascending data, PS on the slopes are moving away from the satellite and, in the descending data, they are moving toward the satellite. This implies a horizontal component of deformation. Given that there is a sharp change in displacement moving from the slopes to the caldera floor, we interpret this mode of deformation as landsliding.

The similarity between Alcedo and Sierra Negra, in terms of evidence of trapdoor faulting, might lead us to assume similar geometries for their shallow magma chambers. Deformation on Sierra Negra between September 1998 and March 1999 can be fit well by an inflating sill-like body situated entirely within the caldera boundaries and about 2 km below the surface [*Amelung et al.*, 2000; *Jónsson*, 2002; *Yun et al.*, 2006]. However, at Alcedo, the offset in the position of maximum LOS displacement rate on the caldera floor between ascending and descending geometries (Figure 4-14) indicates that there is significant horizontal displacement, more consistent with a three-dimensional source than a sill-like body. The asymmetry of the deformation

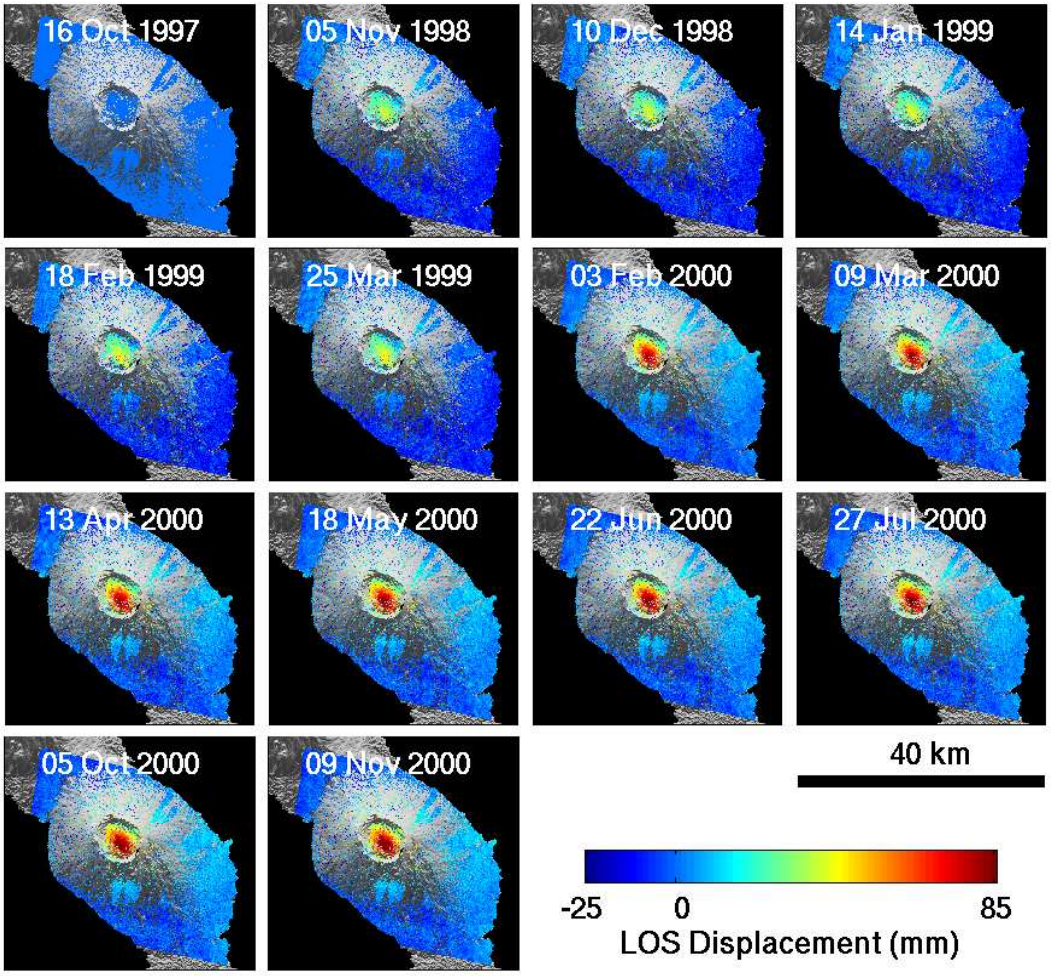

Figure 4-10: Descending orbit PS interferograms for Alcedo, plotted on SRTM topography displayed in shaded relief. The data have been unwrapped and spatially correlated errors have been estimated and subtracted. The data are re-referenced to 16 Oct 1997. Displacements are given relative to PS pixels in the southeast.

pattern suggests that the source is not radially symmetrical, so we model it with a contracting, finite ellipsoid [*Yang et al.*, 1988]. Here, we use only the displacement rates of PS pixels located on the caldera floor, to avoid the second mode of deformation biasing our results. The caldera is essentially flat and we approximate it with a halfspace. We assume a shear modulus of 30 GPa, with no significant change in rheology to the depth of the deformation source, and also assume that the volcano deforms as a Poisson solid.

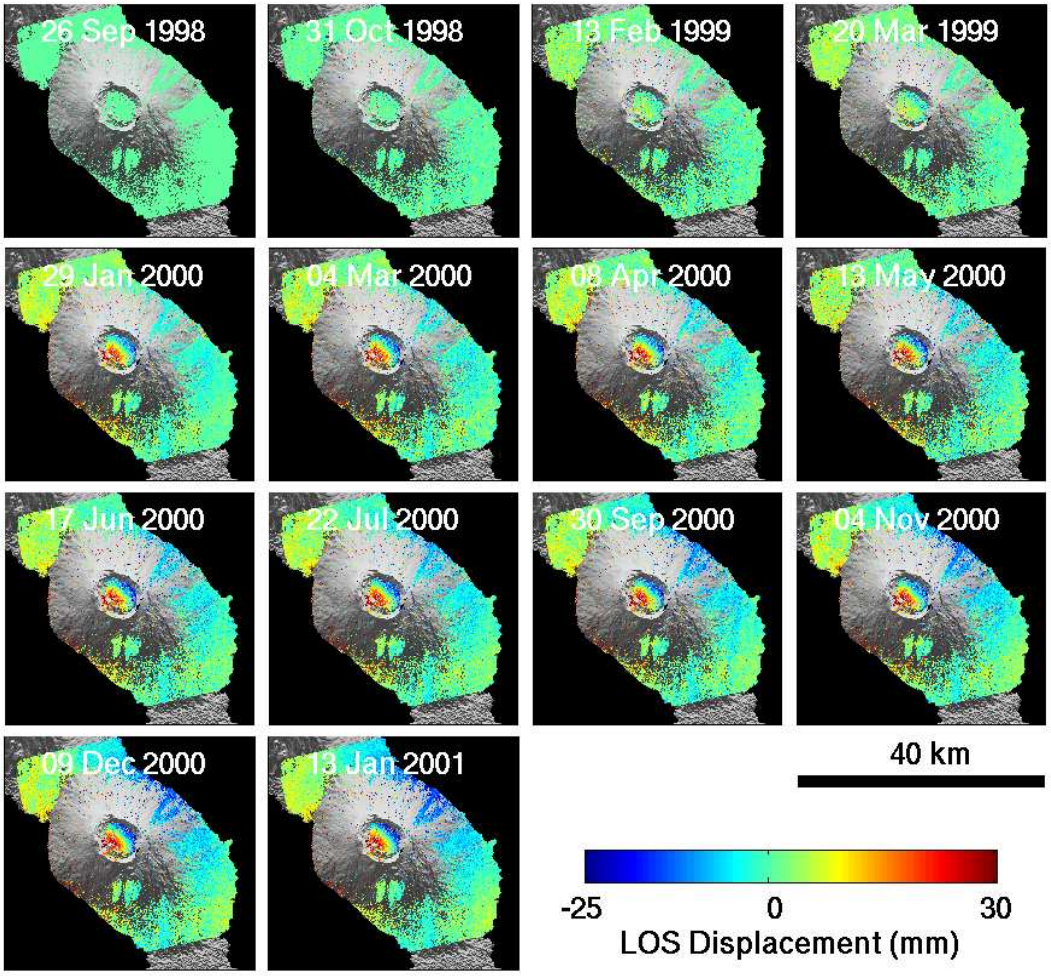

Figure 4-11: Ascending orbit PS interferograms for Alcedo, plotted on SRTM topography displayed in shaded relief. The data have been unwrapped and spatially correlated errors have been estimated and subtracted. The data are re-referenced to 26 Sep 1998. Displacements are given relative to PS pixels in the southeast.

Using both descending and ascending LOS displacement rates, Markov Chain Monte Carlo sampling enables us to find the posterior probability distribution of the model parameters [*Mosegaard and Tarantola*, 1995]. We assume zero displacement at the coasts in the descending data. For the ascending data we estimate an additional displacement offset for the entire caldera. We assume that the probability density of the displacement rates approximates a multivariate Gaussian distribution. Several randomly chosen marginal distributions of the data, estimated using the percentile

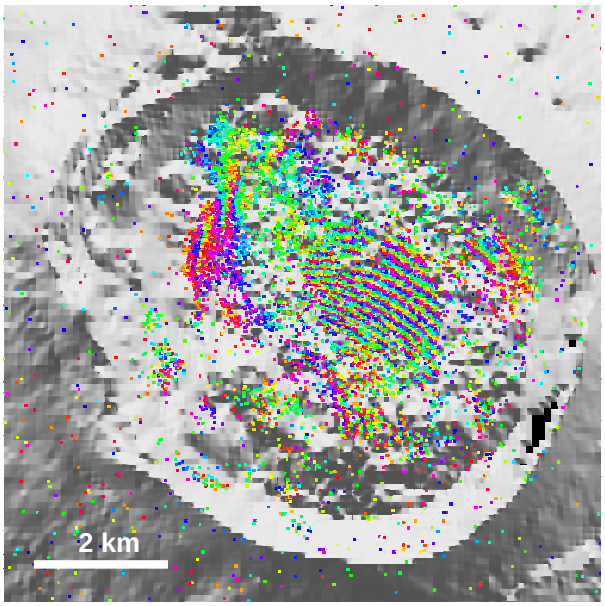

Figure 4-12: Wrapped PS interferogram for Alcedo caldera covering the period 15 Jun 1992 to 05 Nov 1998. The background image is SRTM topography in shaded relief. Each color fringe represents 2.8 cm of displacement in the LOS and the southern end of the fringes is moving toward the satellite with respect to the northern end.

bootstrap method of *Efron and Tibshirani* [1986], suggest this to be a reasonable assumption (Figure 4-15). We reduce the data to a manageable size for computing purposes by sampling both descending and ascending data sets to a 90 m grid. As before, we combine displacement rates for PS pixels within the same grid cell by taking the weighted mean, using $1/\widehat{\sigma}_{rate,x}$ as the weight for each pixel, where $\widehat{\sigma}^2_{rate,x}$ is the estimated variance of the displacement rate distribution for pixel x. We estimate this distribution for each PS using the percentile bootstrap method [*Efron and Tibshirani*, 1986] to recalculate displacement rate 1000 times. The position we assign to each grid cell is the weighted mean position of all PS within the cell.

The variance-covariance of our reduced data sets also follows from the percentile bootstrap method. The probability density function for each reduced data set is given by

$$P(x) = \frac{exp\left\{-\frac{1}{2}(\boldsymbol{x}-\boldsymbol{\mu})^T\boldsymbol{\Sigma}^{-1}(\boldsymbol{x}-\boldsymbol{\mu})\right\}}{\sqrt{(2\pi)^n|\boldsymbol{\Sigma}|}} \tag{4.37}$$

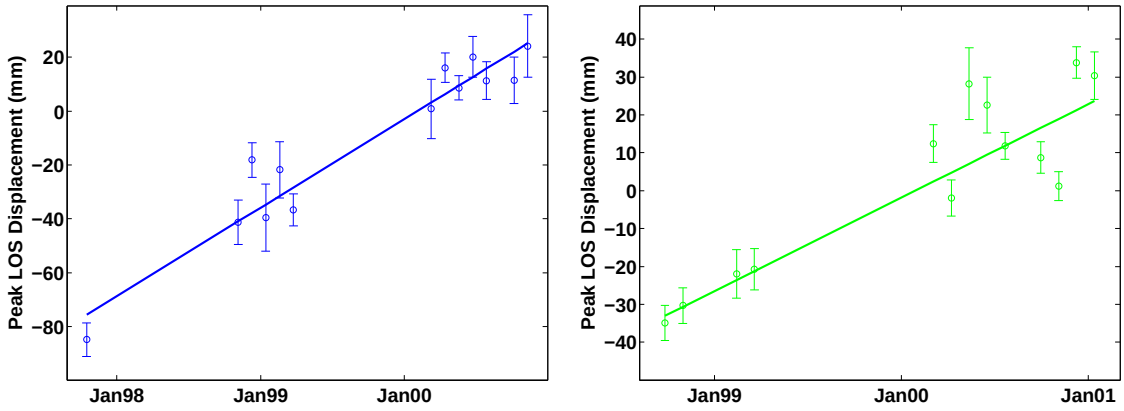

(a) Descending Orbit

(b) Ascending Orbit

Figure 4-13: Maximum LOS displacements on Alcedo. For each PS interferogram the mean LOS displacement of the region of maximum displacement is plotted. For the descending case the displacements are relative to PS pixels near the coasts and for the ascending case the displacements are relative to PS pixels on the east side of the caldera. Error bars represent one standard deviation. The displacements are calculated before spatially correlated terms are subtracted, to avoid any bias caused by temporal smoothing. This causes extra scatter, however, which is not included in the estimate of the standard deviation. Also plotted is the best-fitting constant LOS displacement rate in each case.

where $\boldsymbol{x}$ is the data vector, $\boldsymbol{\mu}$ is the mean vector, $\boldsymbol{\Sigma}$ is the variance-covariance matrix and superscript T denotes the transpose. In order to make $\boldsymbol{\Sigma}$ non-singular, we increase the diagonal variance terms by 10%. This broadens the marginal probability density function for each grid cell by 10%, which we expect to broaden the posterior model distribution by a negligible amount.

4.6.2 Results

The best-fitting model is shown in Figure 4-16, together with the LOS displacements predicted by this model, and the residual difference between these and the data. Although only rates for PS pixels on the floor of the caldera are used in the inversion, the predicted rates are shown for all PS pixels. Residual displacements for PS pixels located on the inner slopes of the caldera are assumed to be due to landsliding. The root-mean-square residual value for the PS pixels used in the inversion is 1.9 mm

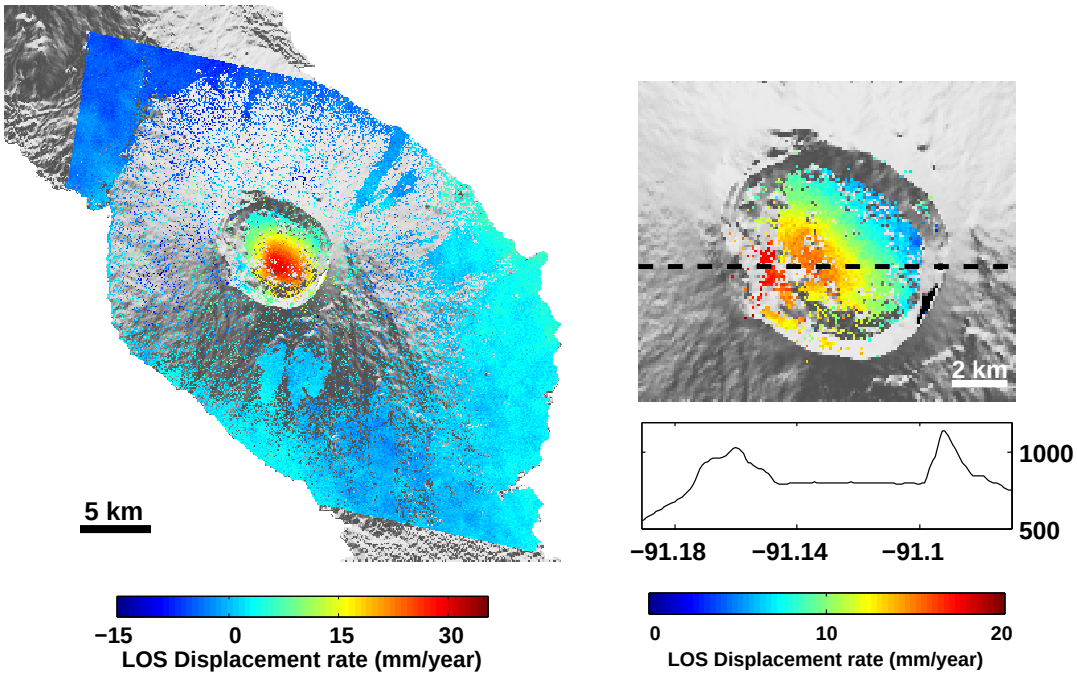

(a) Descending Orbit (b) Ascending Orbit

Figure 4-14: Mean LOS displacement rates on Alcedo between October 1997 and January 2001. For descending orbit data, the rates are referenced to PS on the coasts. For ascending orbit data, the rates are referenced to PS on east side of the caldera. Also shown is the SRTM elevation, in meters, for an east-west transect through the caldera.

yr^{-1}.

We plot marginal probability densities for all the model parameters, except position, in Figure 4-17. The depth of the source is well constrained, lying between 2.21 and 2.26 km below sea level at 95% confidence, with the best fit at 2.24 km. This is based on our assumption of constant shear modulus, however. If the shear modulus actually increases with depth, as is usually the case, we might expect the depth range to be somewhat deeper. Although the semi-major axis of the ellipsoid is well constrained, between 2.5 and 2.7 km at 95% confidence, the aspect ratio is less well constrained. The best-fitting model (shown in Figure 4-16) is very prolate, with an aspect ratio of 25.5, but an aspect ratio of 5.7 would also fit the data at 95% confidence. The volume decrease is well constrained, between 1.25 and 1.30 x 10^6 m^3 at 95% confidence, with a clear trade-off with both the depth and semi-minor axis of

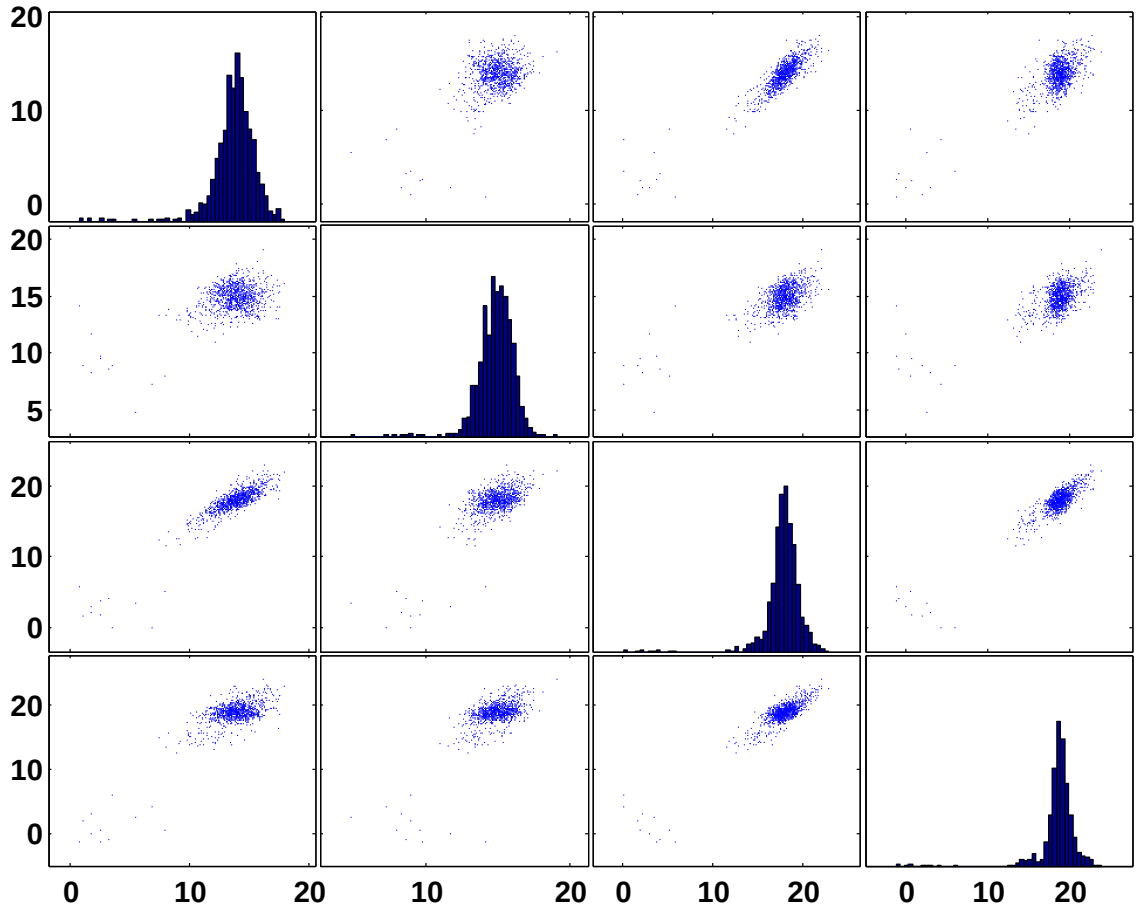

Figure 4-15: Marginal probability distributions of LOS displacement rate, in mm/year, for four randomly chosen PS pixels. The histograms show the distributions for each individual PS pixel, and the scatter plots show the distributions for each pair of PS pixels.

the ellipsoid source. The strike of the ellipsoid lies between 127° and 128° and the dip is sub-horizontal, dipping upwards between 1.3 and 4.7° at 95% confidence.

The residual displacements after subtraction of the deflationary source can be resolved into eastwards and subvertical components. For the PS pixels lying within the circles marked on the residual plots in Figure 4-16, the eastward component is between 6.5 and 6.7 mm/year and the subvertical component is between 2.3 and 2.7 mm/year downwards. This corresponds to an eastward dip of between 19.4° and 21.9° for the motion.

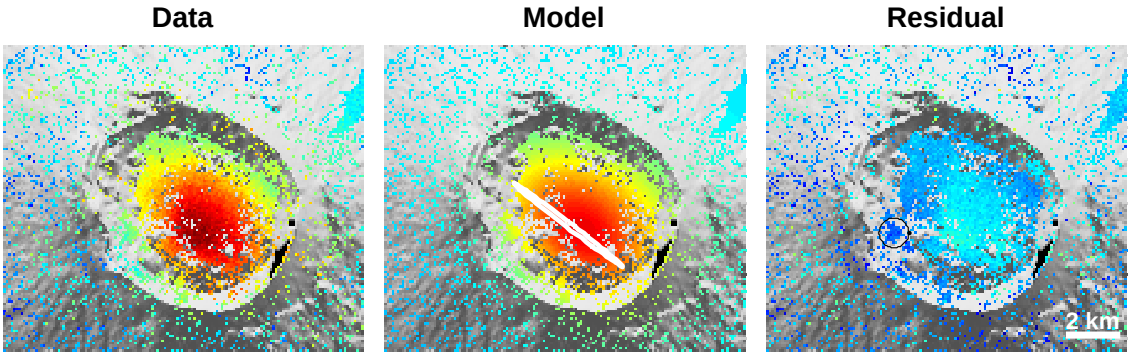

(a) Descending Orbit

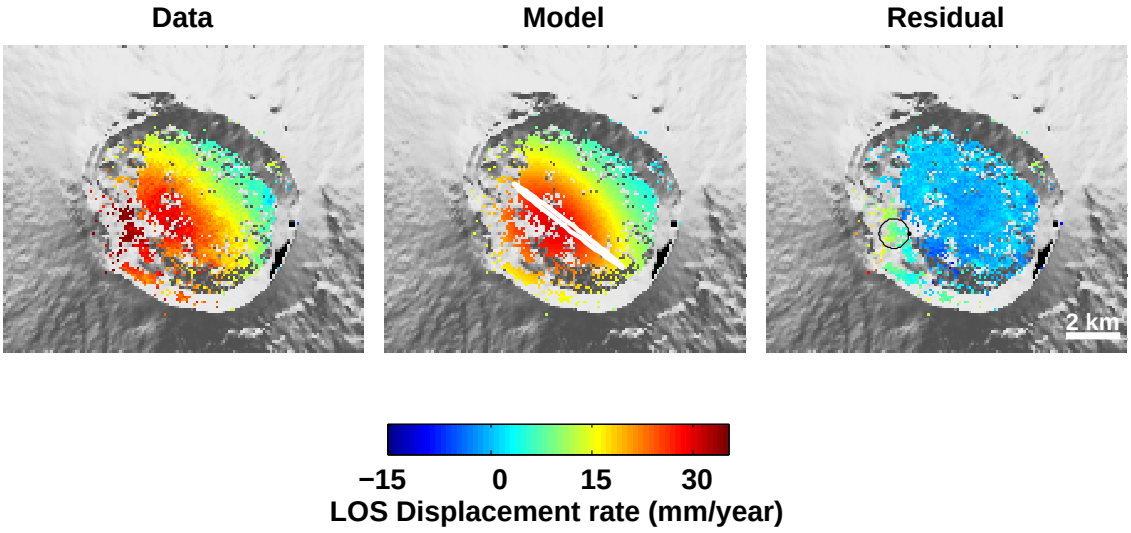

(b) Ascending Orbit

Figure 4-16: Best-fitting model for PS on the caldera floor. The LOS displacement rates of PS pixels are shown, together with the displacement rates predicted by the best-fitting model, and the residual between the two. The ellipse overlaying the predicted displacement rates is the surface projection of the best-fitting ellipsoid deflationary source. The circle overlaying the ascending data marks the location of the PS used for landslide analysis in Section 4.6.2.

4.7 Geophysical Interpretation

Using the Stanford method for persistent scatterers (StaMPS) we are able to extract the deformation signal from SAR data acquired over Volcán Alcedo between 1997 and 2001. The signal we find implies deflation of a subhorizontal, prolate ellipsoidal

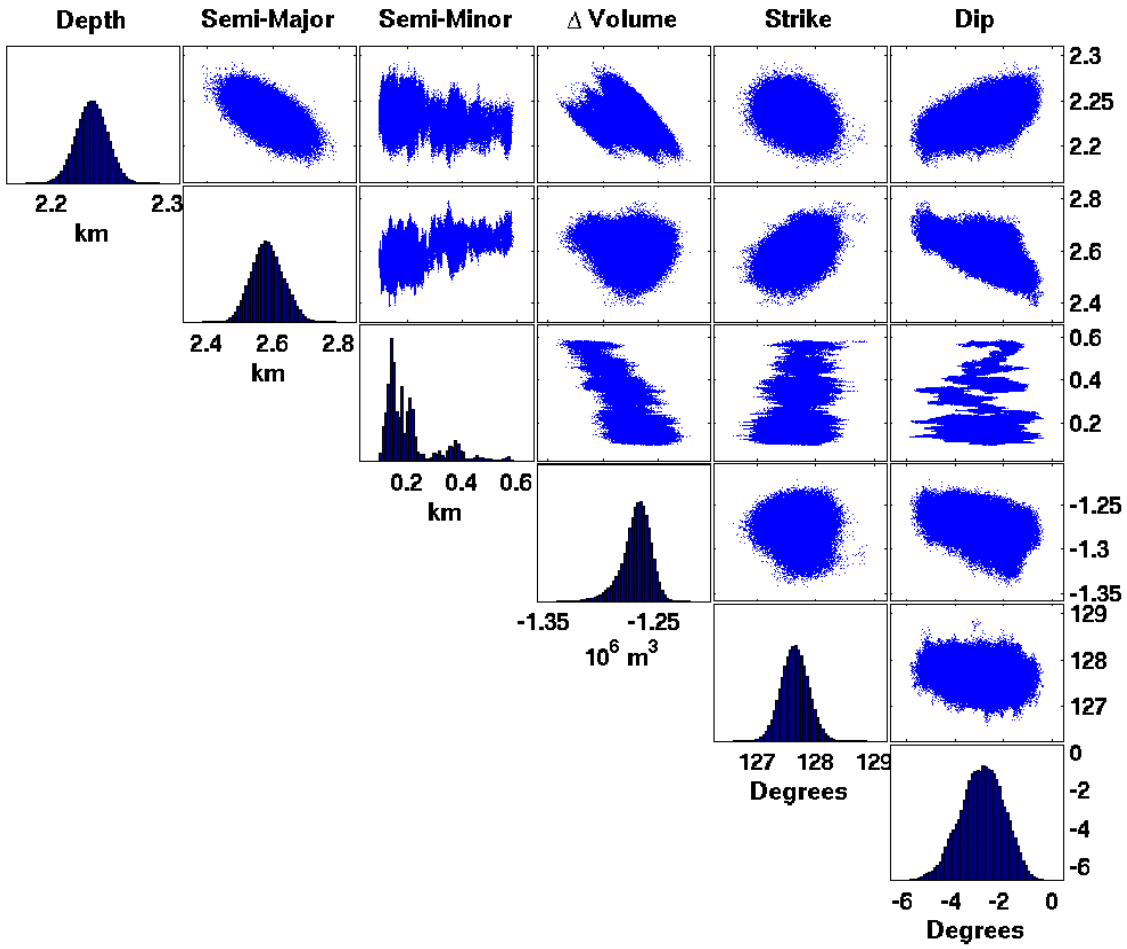

Figure 4-17: Marginal posterior probability distributions for some of the ellipsoidal source model parameters. The histograms show the distributions for individual parameters and the scatter plots show distributions between each pair of parameters.

source, extended in the direction of the long axis of Isla Isabela. We also detect displacements on the inner slopes of the west side of the caldera that are consistent with landslides.

Although the data are reasonably well fit by an ellipsoidal source, in all likelihood, the geometry is more complex in reality. However, it appears that the source of the deflation is not equidimensional, and that the longest axis runs subparallel with the long axis of Isla Isabela in the region of Alcedo. If we assume that the source represents a pre-existing magma chamber, the shape and orientation of the chamber imply that

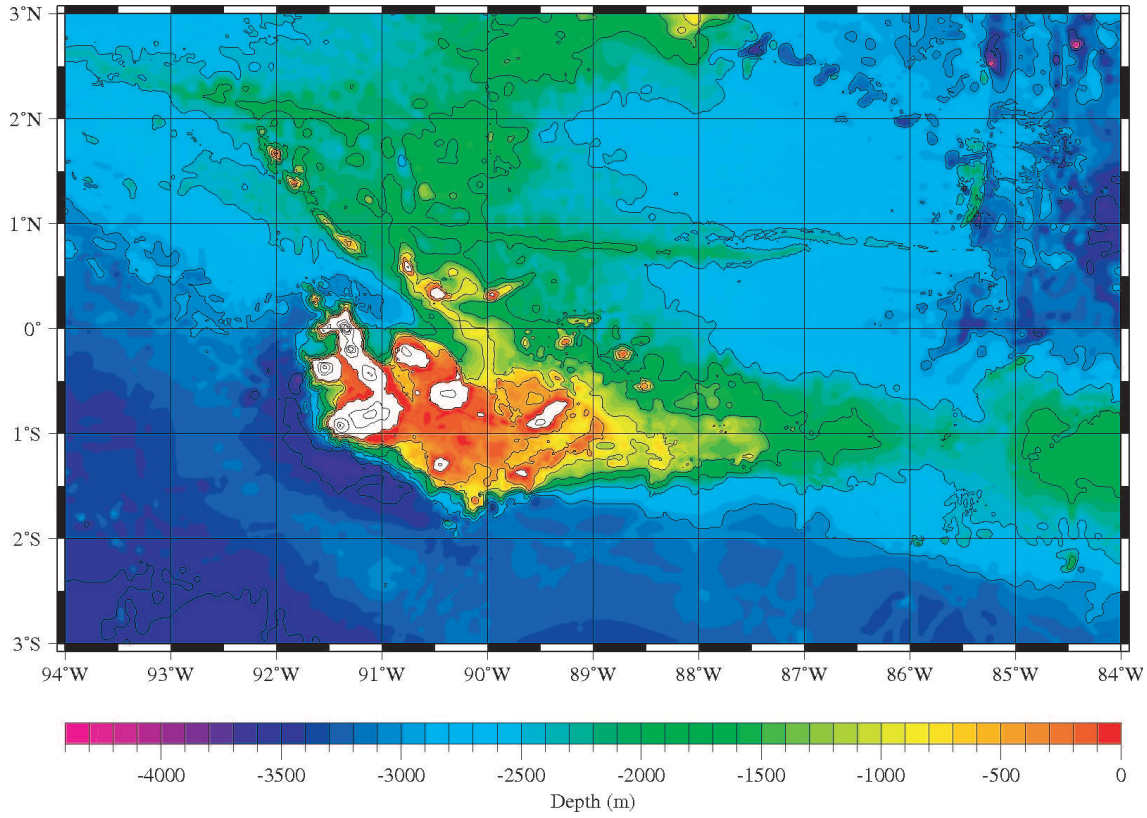

Figure 4-18: Bathymetry of the Galápagos region, compiled by William Chadwick, Oregon State University.

the axis of least compressive stress runs approximately southwest-northeast. The bathymetry of the region (Figure 4-18) shows a raised platform on all sides of Alcedo except to the northeast, where the depth drops rapidly from 500 m to 2500 m within 10 km. Thus we might expect the least resistance to intrusion to be oriented towards the northeast.

There was no known eruption during this period, so the most likely causes of the deflation are contraction due to crystallization and cooling, and the loss of volatiles from the source area. Crystallization of magma emplaced at 3 km beneath the Krafla central volcano in Iceland was estimated to result in a reduction in volume of $\sim 9\%$ [*Sigmundsson et al.*, 1997]. If we assume a similar value for magma emplaced beneath Alcedo, between 0.6 and 10% of the magma would need to crystallize per year, to give the model distribution of volume reduction at 95% confidence. Cooling of the

solidified magma could also contribute further to the volume reduction, with up to 2% contraction being the estimated value for solidified Krafla magma. Loss of volatiles from the magma chamber would reduce the pressure, also leading to a reduction in volume, but the pressure decrease required to produce the surface displacements would be between 23 and 370 MPa $yr^{-}1$ at 95% confidence. This range is too high to be plausibly produced by the loss of volatiles alone.

The local eastward slope dip for the PS pixels circled in Figure 4-16 is 15.7°. Our estimate of the dip of the landsliding motion is somewhat steeper, which suggests that there is additional vertical settling. Given that the displacement rates we measure are those of the dominant scatterers within each pixel, which are most likely the larger boulders in this case, additional settling of these scatterers is possible.

Chapter 5

Phase Unwrapping in Three Dimensions with Application to InSAR Time Series

Chapters 3 and 4 describe a new InSAR method to identify persistent scatterer (PS) pixels and extract the surface deformation from these pixels. A key step in extracting the deformation signal is accurate phase unwrapping, that is, recovering the unambiguous phase values from the phase known only modulo 2π. The problem of phase unwrapping in two dimensions, as applied to conventional InSAR, has been much studied in the last two decades, and in Chapter 3 we unwrapped PS data by solving a series of two-dimensional (2-D) problems. However, PS data sets are in fact three-dimensional (3-D), the third dimension being that of time, and unwrapping accuracy is improved by treating the problem as 3-D.

The 3-D phase unwrapping problem has to date received little attention. We develop here a theoretical framework for three-dimensional phase unwrapping and formulate the problem for the general case. We have not, as yet, developed an algorithm to find the solution for the general case, but we describe here an algorithm we implemented to find the solution in some cases. We also describe a pseudo-3-D algorithm implementation that can be applied to the general case. This algorithm is less accurate than the fully 3-D algorithm for the subset of cases where our current 3-D algorithm is applicable. However, as it is applicable in the general case, it is still useful.

We show that both algorithms give more accurate results than repeated application of a two-dimensional algorithm. We demonstrate the algorithms on a well-sampled case, PS time series acquired over Lost Hills in California, and show that both methods are reliable and robust. The pseudo-3-D algorithm outperforms the 3-D algorithm on a less well-sampled case, PS time series acquired over Long Valley caldera in California, as verified by agreement with ground truth. We note that the pseudo-3-D algorithm described here was also used to unwrap the data in Chapter 4.

5.1 Introduction

Phase unwrapping is the process of recovering unambiguous phase values from phase data that are only known modulo 2π radians (wrapped data). Data of this form are found in many applications, but the advent in the early 1990s of Synthetic Aperture Radar Interferometry (InSAR), in particular, spurred interest in developing reliable two-dimensional (2-D) phase unwrapping algorithms [e.g., *Goldstein et al.*, 1988; *Ghiglia and Romero*, 1996; *Costantini*, 1998; *Zebker and Lu*, 1998; *Chen and Zebker*, 2001]. Recent exciting areas of development within InSAR include persistent scatterer processing [e.g. Chapters 3 and 4; *Ferretti et al.*, 2001; *Kampes*, 2005] and the processing of multiple conventional interferograms simultaneously [e.g., *Berardino et al.*, 2002; *Schmidt and Bürgmann*, 2003]. Both of these applications provide three-dimensional (3-D) wrapped phase data, the third dimension being that of time. Treating the unwrapping problem as one 3-D problem as opposed to a series of 2-D problems leads to an improvement in the accuracy of the solution in a similar way to which 2-D unwrapping provides an improvement over one-dimensional (1-D) unwrapping.

The true phase difference between two neighboring data points for which only wrapped phase values are known has an ambiguity that is an integer number of 2π radians. For unwrapping purposes it is usually assumed that the sampling rate is high enough over most of the data set that aliasing is avoided, i.e., the true absolute phase difference between two neighboring data points is generally less than π radians. One way to view the unwrapping problem is as a problem of integration of the phase

difference between neighboring data points, with one proviso: only certain integration paths may be taken. Specifically, we should not allow integration paths between two adjacent points when the absolute difference between the two is greater than π, a condition referred to as a phase discontinuity in the rest of this chapter. Given the position of the phase discontinuities the problem is then easily solved, as long as the data sampling is dense enough that there are no disconnected regions, i.e., regions with no allowable paths connecting them. However, we do not generally know *a priori* where the phase discontinuities occur and the major goal of most unwrapping algorithms is, therefore, to best determine their positions.

In a 1-D problem, any phase discontinuity will cause a regional disconnect. Furthermore, the only mechanism by which we can estimate the position of the phase discontinuities is by making assumptions about the functional form of the phase variation. Moving from one dimension to two dimensions is helpful in two respects: First, there are more potential paths to choose from, increasing the effective sampling, which in turn decreases the chances of disconnected regions. Second, we are provided with clues as to the position of the phase discontinuities by the presence of residues in the data. A residue, or phase singularity, is a point around which integrating the phase gradient does not return zero [*Goldstein et al.*, 1988]. We might expect, therefore, similar benefits when moving from two dimensions to three and, indeed, this is the case. The effective sampling is again increased, decreasing the chance of disconnected regions, and we are provided with further clues as to the positions of phase discontinuities because residues, which are isolated points in two dimensions, form loops in three dimensions [*Huntley*, 2001], thus providing *a-priori* information on which residues are connected to which other residues by phase discontinuities.

It is commonly accepted that to unwrap 2-D data, the problem is best approached as a single 2-D problem rather than as a series of 1-D problems [*Goldstein et al.*, 1988]. Similarly, with 3-D data, such as a series of interferograms with two spatial dimensions and one temporal, a good approach is to treat the problem as a single 3-D problem rather than as a series of 2-D problems. While branch-cut unwrapping algorithms have been developed by *Huntley* [2001] and *Cusack and Papadakis* [2002] that take advantage of the third dimension, their algorithms are limited in extent

and not directly applicable to InSAR data. Here, we discuss a theoretical framework for 3-D unwrapping and describe a new 3-D unwrapping algorithm that is applicable in certain cases. We also describe a pseudo-3-D algorithm that is more generally applicable.

5.2 Theory of 3-D Unwrapping

In 2-D phase data, neighboring phase discontinuities link to form networks, which resemble tree-like structures [*Goldstein et al.*, 1988]. Residues occur at points along the discontinuity network when the total phase skipped by phase discontinuities around a point changes, including most points where the discontinuity branches and at discontinuity termini. Often, one or more residues lies outside the sampled region, and the discontinuity will appear to terminate at a boundary of the sampled region.

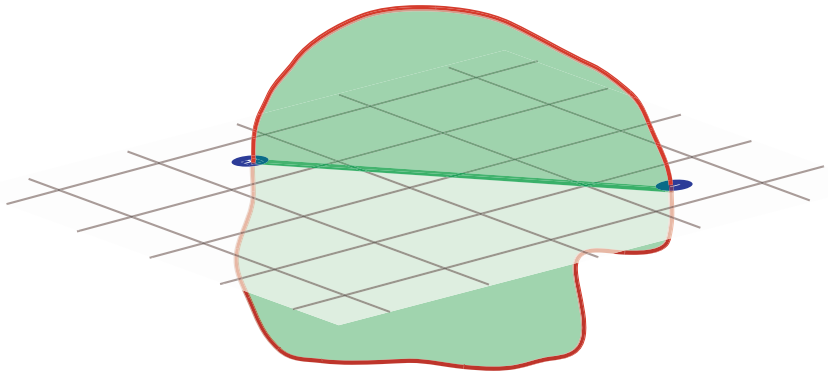

Figure 5-1: A simple phase discontinuity surface, shown in green, intersecting a 2-D data set. The surface is bounded by a residue loop shown in red. Where the surface intersects the 2-D data set results in a discontinuity line, shown in dark green, which is bounded at either end by residues, shown in blue, arising from the intersection of the residue loop with the data set.

In three dimensions, neighboring phase discontinuities link to form surfaces (see Fig 5-1). Any 2-D slice through a discontinuity surface will result in a discontinuity network bounded by residues at the termini, from 2-D theory. This implies that a discontinuity surface must be bounded at all edges by residues. As an edge of any surface forms a loop, these residues must also form loops. Furthermore, it can be

shown that any residue in fact forms a loop in 3-D space [*Huntley*, 2001], including residues within phase discontinuity surfaces. Wherever a residue loop intersects a 2-D data array is detectable. Again, as in two dimensions, part of a residue loop may lie outside the sampled volume, and the discontinuity surface will appear to terminate at a volume boundary.

There is a special type of phase discontinuity in 2-D space that produces no residues, which is a closed loop (not to be confused with a residue loop in 3-D space). This occurs when, due to undersampling, an entire region is isolated from the rest of the data by a phase discontinuity. In this case it is not possible to unwrap reliably in two dimensions without making assumptions about the functional form of the phase variation. The equivalent in 3-D space is a closed surface, which has no edges. In this case it is not possible to unwrap reliably in three dimensions without making assumptions about the functional form.

5.2.1 Single-Cycle Discontinuity Surfaces

Single-cycle discontinuity surfaces are those where the discontinuity is always a single phase cycle. In this case, residue loops occur at all edges and branches of the surface and never within the surface. The simplest surface is an open surface bounded by one edge only (Figure 5-1). Provided it cuts the edge, any 2-D slice intersecting the surface will result in a discontinuity line connecting a positive residue to a negative residue, which is the simplest possible network in 2-D. Just as discontinuity networks in 2-D can branch, so can discontinuity surfaces in 3-D. A single-cycle 2-D branch point will result in a residue as in Figure 5-2(a), Similarly a single-cycle 3-D branch line will result in a residue line, which will connect with an edge to complete a residue loop e.g., Figure 5-2(b). Branching surfaces can therefore be considered as multiple, touching, simple surfaces. A surface can also be bounded by multiple edges e.g., a cylinder or catenoid. These surfaces naturally contain 2-D closed-loop discontinuities, i.e., they are a result of undersampling in 2-D.

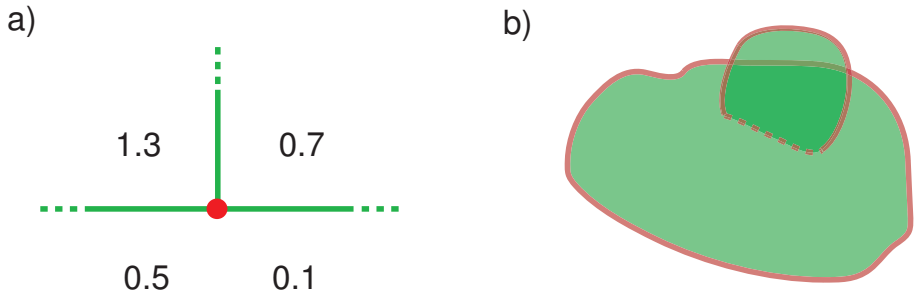

Figure 5-2: A single-cycle branch in (a) 2-D and (b) 3-D. The numbers in (a) represent unwrapped phase values in cycles, the green lines represent single-cycle discontinuities and the red dot represents a residue at the branch point. In (b), the green surfaces represent single-cycle discontinuity surfaces and the red lines represent residue loops, the dashed part being the branch line.

5.2.2 Multiple-Cycle Discontinuity Surfaces

Multiple-cycle discontinuity surfaces are those that include phase discontinuities greater than one cycle. These occur in areas that are locally undersampled or where true discontinuities occur in the data, e.g., due to layover in a topographic interferogram or a surface-breaking fault in a deformation interferogram. The relationship between multiple-cycle discontinuity surfaces and residue loops is more complex. Residue loops still occur at all edges, but not necessarily at all branches, and also occur internally on the surface (see Figure 5-3).

5.2.3 Mimimum L^p-norm Framework

A framework was provided by *Ghiglia and Romero* [1996] that unifies many of the unwrapping approaches in 2-D. Phase unwrapping is set up as an optimization problem within this framework. The goal is to find the solution that minimizes an objective function of the form

$$\sum_{i,j} w_{i,j}^{(x)} \left| \Delta\phi_{i,j}^{(x)} - \Delta\psi_{i,j}^{(x)} \right|^p + \sum_{i,j} w_{i,j}^{(y)} \left| \Delta\phi_{i,j}^{(y)} - \Delta\psi_{i,j}^{(y)} \right|^p \tag{5.1}$$

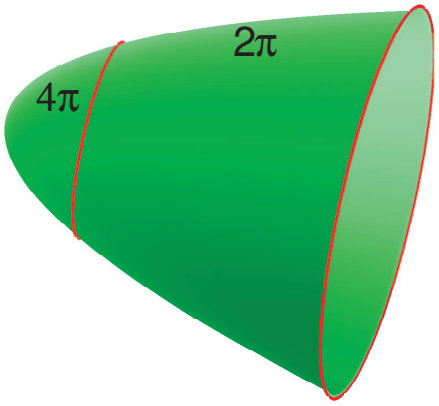

Figure 5-3: A multiple-cycle discontinuity surface (in green). The red loops represent residue loops, the right loop bounding the edge of the surface and the left loop separating the 2π phase discontinuity region of the surface from the 4π discontinuity region.

where $\Delta\phi^{(x)}$ and $\Delta\psi^{(x)}$ are the x direction components of the unwrapped and wrapped phase differences respectively, $\Delta\phi^{(y)}$ and $\Delta\psi^{(y)}$ are the equivalent y direction components, and w are user-defined weights. The summations are carried out in both x and y directions over all i and j respectively. This is referred to as an L^p-norm objective function by *Chen* [2001], although, strictly speaking, to meet the condition of positive scalability the sum must be raised to the power of $1/p$ and p must be greater than or equal to 1. For continuity however, we follow the convention of *Chen* [2001] in referring to the solution that minimizes the above function as an L^p-norm solution for $p \geq 0$, and note that for $p \geq 1$, the solution that minimizes this objective function also minimizes the L^p-norm. This framework can be extended to 3-D as

$$\begin{aligned} minimize \quad & \left\{ \left(\sum_{i,j,k} w^{(x)}_{i,j,k} \left| \Delta\phi^{(x)}_{i,j,k} - \Delta\psi^{(x)}_{i,j,k} \right|^p + \sum_{i,j,k} w^{(y)}_{i,j,k} \left| \Delta\phi^{(y)}_{i,j,k} - \Delta\psi^{(y)}_{i,j,k} \right|^p \right. \right. \\ & \left. \left. + \sum_{i,j,k} w^{(z)}_{i,j,k} \left| \Delta\phi^{(z)}_{i,j,k} - \Delta\psi^{(z)}_{i,j,k} \right|^p \right)^{1/p} \right\} \end{aligned} \tag{5.2}$$

where $\Delta\phi^{(z)}$ and $\Delta\psi^{(z)}$ are the phase difference components in the third dimension, and the summations are extended to the z direction over all k. The objective function is an L^p-norm for $p \geq 1$, but for convenience we also refer to the solution for $p = 0$ as the L^0-norm solution.

An additional constraint is that of congruence, so that the unwrapped phase values differ from the wrapped phase values only by integer multiples of 2π. Typically in 2-D, algorithms based on minimization of L^0- and L^1-norms enforce congruence, while L^2-norms do not, due to the way in which they are implementated. The result of not enforcing congruence, however, is to systematically underestimate true unwrapped phase gradients [*Bamler et al.*, 1998; *Zebker and Lu*, 1998], so congruence is generally desirable.

In 2-D at least, L^0-norm solutions are seen empirically to give more accurate solutions than minimizing other L^p-norms [*Ghiglia and Pritt*, 1998; *Zebker and Lu*, 1998] and, hence, we might expect this to be the case in 3-D. However, finding the solution that minimizes the L^0-norm is a non-deterministic polynomial-time hard (NP-hard) problem even in two dimensions *Chen* [2001]. Thus , for all practical purposes, it is impossible to determine the exact solution, although various methods have been implemented in two dimensions that find an approximate solution, e.g., using network-flow theory [*Costantini*, 1998; *Chen and Zebker*, 2000]. Here, we do not attempt to find the L^0-norm solution for the general case but, instead, we consider higher order norms.

If congruence is enforced, the only difference in going from an L^0-norm to an L^1-norm is to penalize multiple-cycle discontinuities over single-cycle discontinuities [*Chen*, 2001]. Further increase of p further penalizes multiple-cycle discontinuities and in the limit as $p \to \infty$ single-cycle discontinuities are always favored over multiple-cycle discontinuities. Clearly then, if there are multiple-cycle discontinuities present in the data the L^∞-norm solution will not be correct, but in the case where only single-cycle discontinuities exist it will be identical to the L^0-norm solution. In other words, in the case where the data and sampling are such that there are no multiple-cycle discontinuities, the L^∞-norm solution is also the best solution under this framework. Most interferograms that include the topographic signature do contain multiple-cycle

discontinuities due to the presence of layover, and the L^∞-norm is therefore not suitable. However, for interferograms where the topographic signature has been mostly subtracted, e.g., when interested in the deformation signal, the L^∞-norm solution may be useful.

Fitting a minimal surface to every residue loop gives a solution with no multiple-cycle discontinuities, i.e, the congruent minimum L^∞-norm solution. Strictly speaking the solution that minimizes the L^∞-norm could include single-cycle discontinuity surfaces that are bounded by multiple loops, which result in closed-loop discontinuities in 2-D. Although we expect these surfaces to be rare in well-sampled data sets, fitting a minimal surface to every loop does not allow for this type of surface, hence we refer to it as a quasi-L^∞ approach. The *Huntley* [2001] algorithm falls in this class, although the way in which it deals with truncated residue loops is not a true L^∞-norm minimization.

In the following section we describe an algorithm to implement the quasi-L^∞ approach. This is our 3-D solution. In the case where the data are sampled sufficiently well that there are no closed-loop nor multiple-cycle discontinuites, and the underlying nature of the data is such that these discontinuity types do not arise, we expect this solution to be identical to the L^0-norm solution. For more general applications, a true L^0-norm solver should be developed. Optimization using generalized, nonlinear cost functions, as done in two dimensions by *Chen and Zebker* [2000], could lead to a more accurate solution still, particularly in the case of InSAR as we might expect cost functions in the space-time domain to be quite different to those purely in the spatial domain.

A residue naturally has sign and in 2-D, the sum of all residues on a phase discontinuity network must be zero, assuming no truncation by the data set boundary [*Goldstein et al.*, 1988]. That is to say, for any 2-D slice through a 3-D discontinuity surface the residues must sum to zero. If residues are only calculated in distinct 2-D planes then, as is the case for a regular 3-D grid, all residues in a closed residue loop will sum to zero. If however residues are calculated on arbitrary planes, as in the algorithm we present here for sparse data, the sum need not be zero.

5.3 Quasi-L^∞-norm 3-D Algorithm

In order to unwrap InSAR persistent scatterer time series, which are distributed irregularly in space, we have developed an algorithm to unwrap 3-D data that is irregularly sampled in two dimensions. The algorithm allows for residue loops to be terminated any number of times at any number of data volume boundaries. As a default, for each loop, the algorithm selects a phase discontinuity surface that is a minimal surface, equivalent to the surface formed by an equilibrium soap film in zero-gravity. In this algorithm we assume that each discontinuity surface is bounded by only one loop, as discussed in Section 5.2.3.

5.3.1 Residue Identification

Residues are identified by dividing the 3-D data into a number of faces with a data point at each vertex, calculating the difference in phase along arcs between adjacent vertices, wrapping the difference into the interval $-\pi$ to π, and integrating the differences around the face. A non-zero sum indicates a residue. In 2-D, if the data are regularly sampled, the simplest approach is to divide the data into rectangular faces and if the data are irregularly sampled (sparse), Delaunay triangulation can be used to divide the data into triangular faces [*Costantini and Rosen*, 1999]. Similarly, in 3-D, if the data are regularly sampled, the simplest approach is to divide the data into rectangular faces in three orthogonal orientations. However, to be applicable to InSAR data sets that are sparse in the two spatial dimensions, we use Delaunay triangulation to define arcs connecting the data points within the two spatial dimensions and integrate around each triangle. In the time dimension, we assume that the data are regularly sampled, in the sense that for every sample in time the phase is sampled at every point in the two spatial dimensions. Therefore, we can define arcs that divide the data into rectangular faces and integrate around the rectangles. The faces in this irregular grid outline a series of wedge-shaped elements, each with two triangular faces and three rectangular faces (see Figure 5-4).

The algorithm could be extended to the case where data are irregular in all three dimensions by connecting the data points through Delaunay tetrahedrization to form

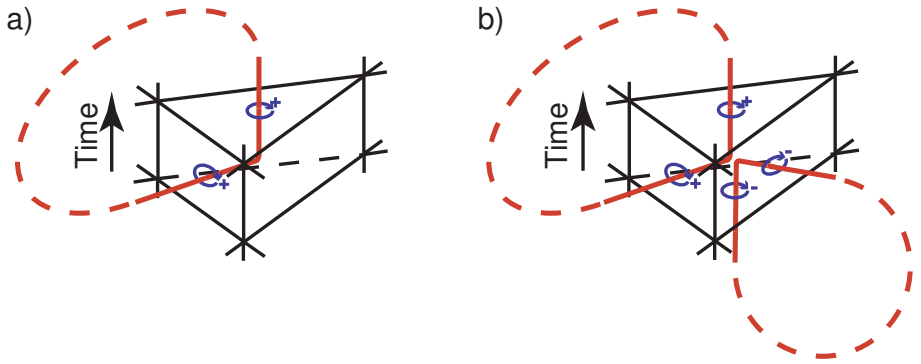

Figure 5-4: Residue identification and connection. Each apex represents a data point and the black lines represent the arcs along which phase differences are calculated. Residues, shown in blue, are identified by integrating arc phase differences around each triangular or rectangular face. (a) shows an element with residues on two faces. A residue loop, shown in red, enters the element through one face and exits through the other. (b) shows an element with residues on four faces. The four residues could be linked to form either two separate loops (as shown) or one twisted figure-eight loop.

tetrahedron-shaped elements.

5.3.2 Linking Residues

Residues must be linked to form loops. As argued in Section 5.2, residues form loops in 3-D space, that are detectable wherever they intersect a face. This implies that any loop entering a wedge element through one face must exit the wedge element through another face (see Figure 5-4a). Residues can be linked, therefore, by tracing the loops through each wedge element in turn, until the loop either closes on itself or a data volume boundary is reached. As each wedge element has five faces, it is possible for two residue loops to pass through the same element, intersecting four faces in total (see Figure 5-4b). The residues on the intersected faces could then be linked in two different ways, one way forming two distinct loops, and the other way forming only one loop in the form of a twisted figure-eight, with the cross-over point placed at the center of the element. However, the discontinuity surfaces found by a later step of the algorithm would be identical for both scenarios, so it is not necessary to distinguish between them.

5.3.3 Processing Closed Residue Loops

As discussed in Section 5.2.3, we assume that each residue loop bounds a single-cycle phase discontinuity, which is equivalent to finding the quasi-L^∞-norm solution. Any given closed residue loop bounds an infinite number of surfaces, but minimizing the L^∞-norm corresponds to finding the minimal surface. This is equivalent to the surface that would be formed by an equilibrium soap film in zero-gravity. We use an iterative program called Surface Evolver[*Brakke*, 1992] to find an approximation to this surface for each closed residue loop.

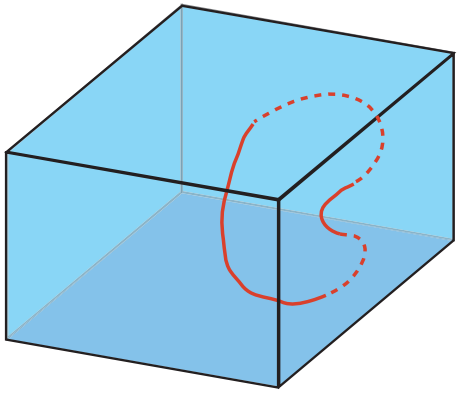

Figure 5-5: A residue loop, shown in red, that is truncated at the data volume boundaries, shown in blue. The continuous parts of the loop are contained within the data volume, while the dashed parts lie outside. The loop is truncated four times, once at the top boundary and three times at the right boundary.

5.3.4 Processing Truncated Residue Loops

In practice, some residue loops may lie partially outside our data volume, causing truncation of the associated residue loops at the data volume boundary. Loops can pass through the boundary any even number of times, resulting in any number of truncated residue loops (see Figure 5-5 for an example). The assumption that every truncated loop closes on itself [*Huntley*, 2001] is, therefore, not necessarily correct and a more complex algorithm is needed to close all the truncated loops. We allow for the linking of multiple loops to minimize the total surface area of the surfaces formed. We also allow for the linking of ends that are truncated by different volume

boundaries. Up to now, surface area has had only relative meaning, as the units are not the same in all dimensions (two are in space and one is in time). This does not matter when fitting a minimal surface to a predefined closed loop in the section above, as scaling in any dimension simply scales the minimal surface but does not alter its position. With the option of closing loops across differing dimensions, however, the dimension scaling does matter. We therefore scale the time dimension to be consistent with the two spatial dimensions. We assume that the probability of a residue being present within any face is related to the length of the bounding arcs. Empirically we find that the data are reasonably well-fit by the logarithmic model

$$\frac{N_{res}}{N_{arc}} = k\ log L_{arc} + c \tag{5.3}$$

where L_{arc} is the length of an arc, N_{res} is the number of arcs of length L_{arc} bounding a residue, N_{arc} is the total number of arcs of length L_{arc} and k and c are constants (see Figure 5-6). We invert the data from the two spatial dimensions to estimate k and c, in a least-squares sense, and use these values in the time dimension to calculate an equivalent L_{arc} between each interferogram.

We seek the combination of closed loops that minimizes the total surface area of the surfaces formed. Given n partial loops, the number of ways of forming closed loops is equal to the number of ways of connecting $2n$ points, with each connected to exactly one other point, which is $(2n-1)!$. The number of solutions increases, therefore, in a non-polynomial fashion and a brute force search of all combinations is not possible. Instead, we implement a Monte Carlo algorithm to search for the minimum solution. Connecting two close ends is more likely to lead to a minimal surface than two distant ends, as the connection between the two ends itself forms one of the boundaries of the resulting surface. Our approach, then, is to start with a solution where all partial loops are self-closing. We calculate the total surface area of this solution to find an initial minimum solution. We then select one of the loop connections, the probability of being chosen being proportional to its length, and break it. This leads to two free ends, A and B. For free end A, the next nearest end, C, is found, which is currently connected to D. There is a probability that we break

the connection of C to D and make a new connection A to C. The probability is calculated as

$$P = \frac{AB}{AB + AC} \tag{5.4}$$

where AB is the distance between A and B and AC is the distance between A and C. In other words, if the change leads to a reduction in length, it is favored. If the connection is not broken, we find the next-nearest end and go through the same exercise, repeating until a new free end is formed. The same procedure is executed for the other free end, B. This process of breaking and forming connections proceeds until the two free ends connect to each other at which point we have a new solution. If the total surface area of the new solution is less than the current minimum solution, it becomes the new minimum solution. We continue to seek new solutions until a specified number of consecutive new solutions are found without finding a new minimum solution. The number is arbitrary and typically we use 100.

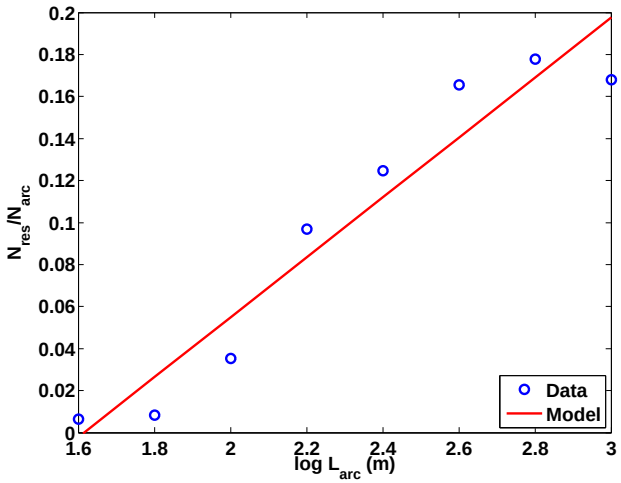

Figure 5-6: Relationship between the length of the the arcs connecting data points, L_{arc}, and the fraction of arcs bounding residues, N_{res}/N_{arc}. These data are from the Lost Hills example (Section 5.5.2). The model we fit assumes an exponential relationship.

5.3.5 Integration of Phase

We next identify the arcs that are intersected by discontinuity surfaces. We use a flood-fill algorithm to integrate the phase, with the intersected arcs being barriers to flow. Specifically, we start from an arbitrary data point and integrate the phase along un-intersected arcs to the neighboring data points. Starting from these points we then integrate the phase again along un-intersected arcs to neighboring data points not yet reached. This continues until no further data points can be reached.

5.3.6 Application to InSAR Time Series

As for 2-D unwrapping algorithms, the 3-D algorithm described above is applicable if the sampling rate is high enough over most of the data set that aliasing is avoided. In InSAR time series, however, the phase is undersampled in time for every point in space, due to the change in atmospheric retardation, which can vary by greater than π in much less than the time between acquisitions for all existing SAR data sets. There is also a phase term due to error in orbital estimation which approximates a ramp in space. Though often small, this term can also be greater than π in magnitude. We reduce these terms to less than π over most of the image by estimating the longer wavelength components of the phase variation between each interferogram, which include most of the atmospheric and orbital error signal [*Hanssen*, 2001]. We subtract this phase and unwrap it separately, as described in detail below. There remains a component of the atmospheric phase between each interferogram, which is an integer number of 2π, and which we are not able to estimate. However, we are not interested in the absolute value of the atmospheric phase and a constant integer number of 2π offset has no effect on unwrapping.

For each pair of interferograms in time, we estimate the highest frequency component of spatially correlated phase that is possible given our sampling density, i.e., we avoid aliasing. We transform the complex phase difference between the interferogram pair to the frequency domain and iteratively low-pass filter, starting with a broad frequency response and decreasing the width until the filtered phase contains no residues. Unwrapping of the filtered phase is therefore unambiguous. To enable

use of the fast Fourier transform the complex phase difference is first transformed to a grid, using a grid spacing over which little variation in phase is expected (typically 40 to 100 m). Where multiple pixels fall in the same grid cell, the complex phase is summed. Long-wavelength deformation may be included in the low-pass filtered phase that is subtracted, but this is of no concern as the filtered phase is only subtracted temporarily and, after unwrapping, is added back.

5.3.7 Optional Pre-Filtering

Optionally, if the data are very noisy, a pre-filtering step can be run to filter the data spatially before unwrapping, as is common in 2-D [*Goldstein and Werner*, 1998]. For each time step, the complex phase data are first sampled to a grid using a grid spacing over which little variation in phase is expected (typically 40 to 100 m). Where multiple pixels fall in the same grid cell, the complex phase is summed. The gridded phase is then transformed using the fast Fourier transform and filtered in the frequency domain using an adaptive phase filter [*Goldstein and Werner*, 1998]. This preserves the dominant frequencies which are present in the data. After inverse transformation, the grid cells containing data are treated as the new data points for input into the unwrapping algorithm.

5.4 Pseudo-3-D Algorithm

As discussed in Section, the quasi-L^∞-norm solution is only applicable when there are no multiple-loop discontinuity surfaces in a data set. In the future we hope to implement an L^0-norm algorithm for these cases. In the absence, as yet, of an efficient algorithm to find the L^0-norm solution, we describe here an alternate approach that uses all three dimensions.

The algorithm first unwraps the data in one dimension, time in the case of InSAR time series, then uses the results as an initial solution for optimization in the other two dimensions. Although not strictly 3-D, this approach is applicable when

multiple-loop discontinuity surfaces are present in the data, unlike the quasi-L^∞ approach. Furthermore, several efficient unwrapping routines already exist in 2-D, e.g., minimum-cost-flow [*Costantini*, 1998], statistical-cost network-flow [*Chen and Zebker*, 2001] and iterative least-squares, which is described in this section.

As discussed in Section 5.3.6, changes in atmospheric delay between passes can lead to total decorrelation in the time dimension, so it is not possible to unwrap the phase of individual pixels in time. However, by calculating the phase difference between nearby pixels, the atmospheric contribution is largely canceled. Our approach is to use Delaunay triangulation to define arcs connecting pixels, and for each arc, to calculate the phase difference in each interferogram. For each arc we unwrap these phase differences in time. The unwrapping step consists first of low-pass filtering the complex phase difference time series in the frequency domain using a Gaussian window. The phase difference between each filtered data point is then calculated, wrapped to be between $-\pi$ and π, and integrated. The original arc time series is unwrapped on the basis that the absolute difference between it and the unwrapped filtered time series must be less than π.

If the data were regularly gridded, an algorithm such as snaphu [*Chen and Zebker*, 2001] could be used to unwrap the data in the spatial domain. A version of snaphu for sparse data has not yet been developed, however, so our algorithm is implemented using an iterative weighted least-squares approach instead, which we describe here. For each interferogram, the unwrapped arc phase differences from the first step are inverted to give the phase at each pixel using weighted least-squares. For weighting we use the inverse of the standard deviation of the difference between the arc time series and the filtered arc time series. We then calculate the residuals between the arc phase differences from the first step and the arc phase differences predicted by the model, and the arcs with the largest residuals are dropped. The process is repeated until all residuals are zero. The optimal solution using this approach would be achieved by dropping only one arc per iteration. Computationally this is expensive, however, so typically we initially drop a maximum of 0.1% of the arcs per iteration. If dropping multiple arcs will lead to the inversion becoming rank deficient we reduce the maximum number to be dropped by a factor of 10. This continues until the

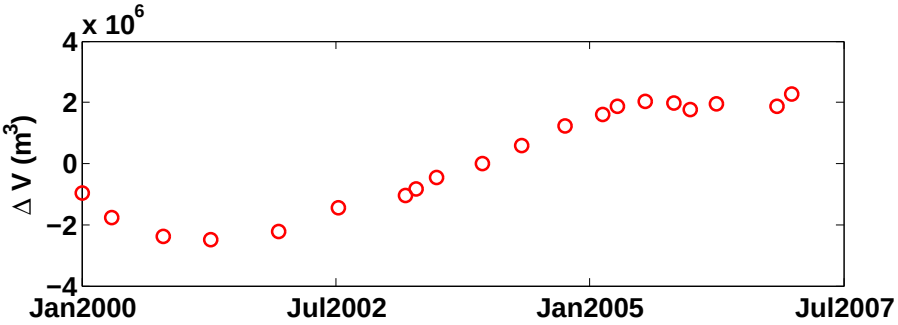

Figure 5-7: The simulated change in volume of a center of dilation that is used to calculate the deformation phase contribution to the simulated phase data in Figure 5-8.

maximum becomes one, or a zero residual solution is reached.

As in the case of the quasi-L^∞ 3-D algorithm, if the data are very noisy, an optional pre-filtering step can be run to filter the data spatially before unwrapping [see Section 5.3.7].

5.5 Experimental Results

5.5.1 Simulated Data Example

We begin to assess our phase unwrapping algorithms by examining a set of simulated interferograms.

We simulated a center of dilation within a homogeneous elastic half space [*Mogi*, 1958] at 2 km depth, with volume changing at a rate defined by a random walk (see Fig 5-7). We selected 4000 points randomly within a 20 by 20 km area above the point source. The surface deformation was calculated at these points for 20 randomly spaced satellite passes, assuming a satellite repeat period of 35 days, and converted into line-of-sight phase difference with respect to the 10th pass. We added a random atmospheric phase signal for each scene with the spectral power following a -5/3 power law for wavelengths larger than 2 km and -8/3 for wavelengths less than 2 km [*Hanssen*, 2001]. The maximum variation of the atmospheric signal simulated for each interferogram has a mean of 2.9 radians. We also added white noise, with

a standard deviation of 50°, to every scene. Finally we differenced every scene with respect to the 10th scene as our "master" scene, and wrapped the data (Fig 5-8).

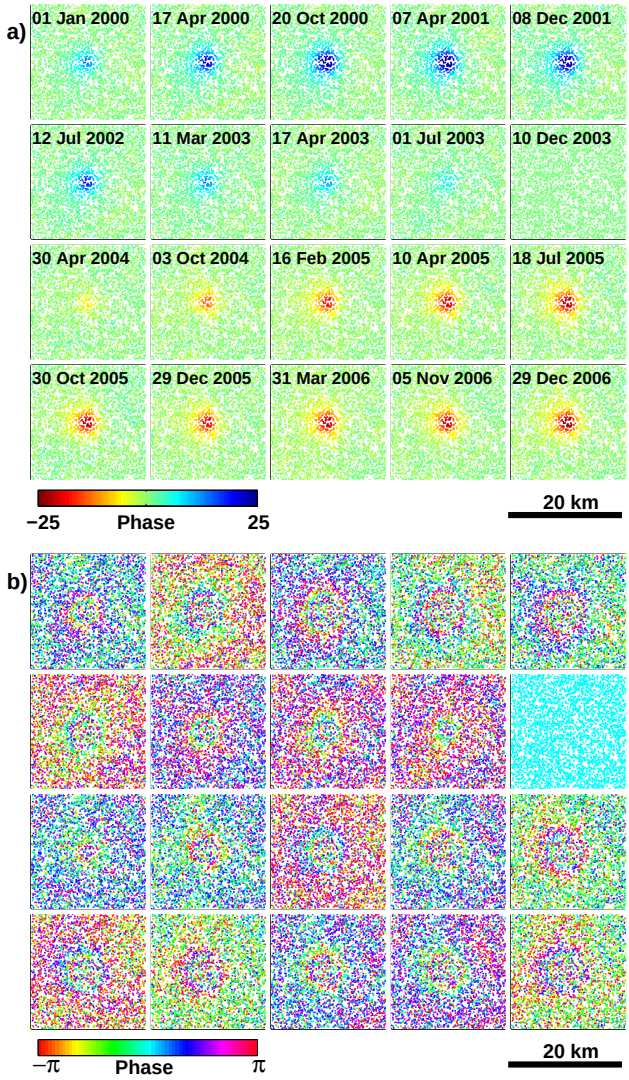

Figure 5-8: Simulated phase data, (a) unwrapped and (b) wrapped, including deformation phase, atmospheric phase delay and noise. The unwrapped phase is referenced to the north-east corner to enable comparison with Figure 5-9.

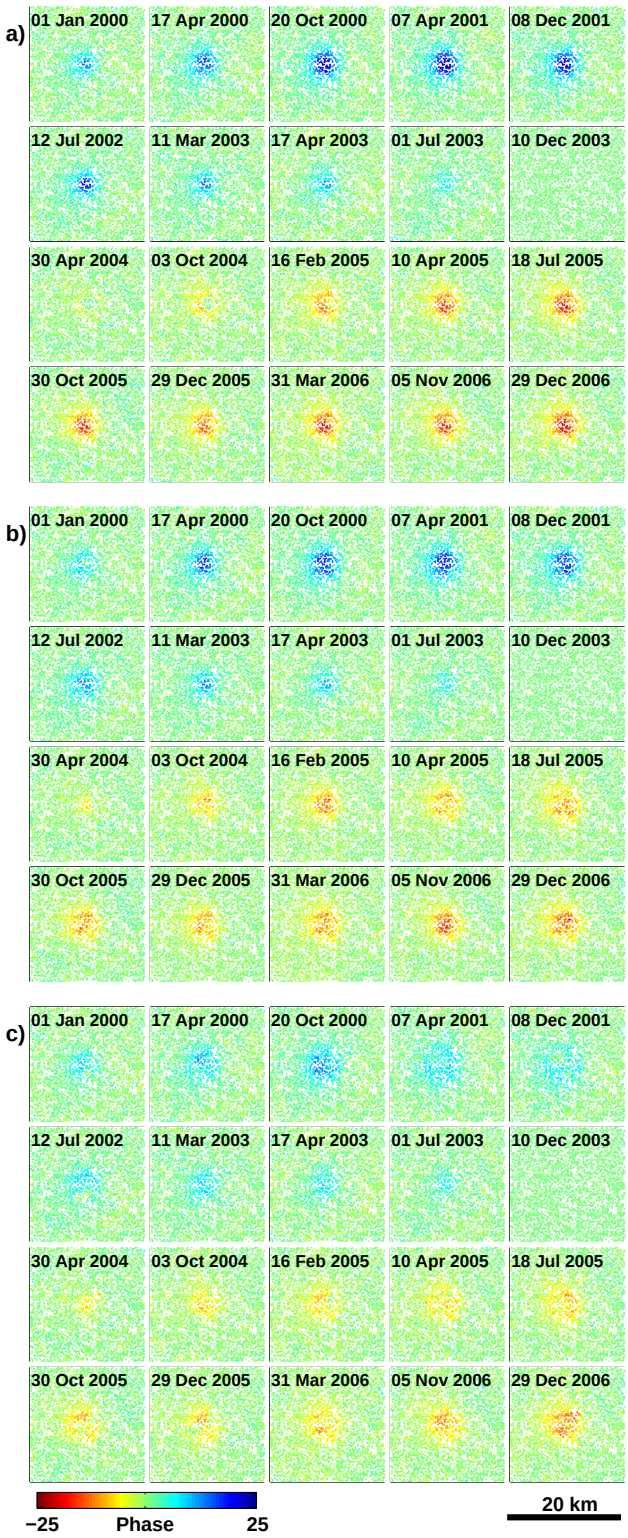

Figure 5-9: Simulated data unwrapped using (a) the quasi-L^∞ 3-D algorithm, (b) the pseudo-3-D algorithm and (c) an iterative least-squares 2-D algorithm. In all cases the phase is referenced to the north-east corner.

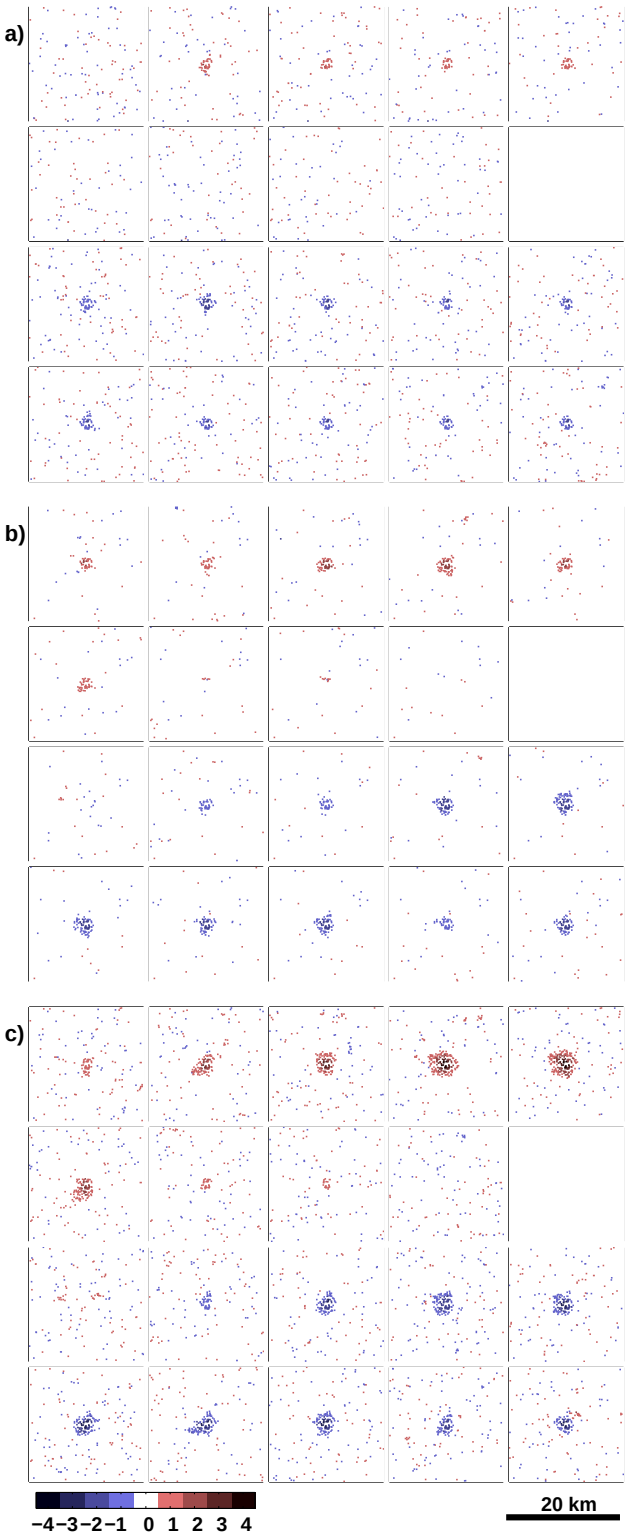

Figure 5-10: Difference in cycles between the simulated unwrapped phase and that estimated by the three algorithms, (a) the quasi-L^∞ 3-D algorithm, (b) the pseudo-3-D algorithm and (c) an iterative least-squares 2-D algorithm.

The results of unwrapping using the quasi-L^∞-norm 3-D algorithm and the pseudo-3-D algorithm are shown in Figure 5-9. Also shown for comparison are the results of unwrapping each interferogram separately using a 2-D iterative least-squares algorithm. No pre-filtering of the phase in the spatial domain was applied prior to running any of the algorithms. The problem becomes progressively undersampled as the deformation gradient increases so that even the 3-D algorithm is unable to unwrap accurately the peak deformation signal in every interferogram. The 3-D algorithm does unwrap the peak deformation signal more accurately than the pseudo-3-D algorithm, however, which in turn does better than the 2-D algorithm. Figure 5-10 shows the residuals between the unwrapped values and the true values. While the spatial pattern of deformation is better retrieved by the 3-D algorithm than the pseudo-3-D algorithm, there are more local, single-cycle errors. This is also apparent in Figure 5-11, a comparison of unwrapping accuracy for the different algorithms. The 3-D algorithm performs better than the pseudo-3-D in terms of multiple-cycle errors, but worse in terms of single-cycle errors. However, when recovering the deformation field we are more concerned with avoiding the systematic errors around the peak deformation than these randomly distributed errors. For our purposes, therefore, the 3-D algorithm gives the best results.

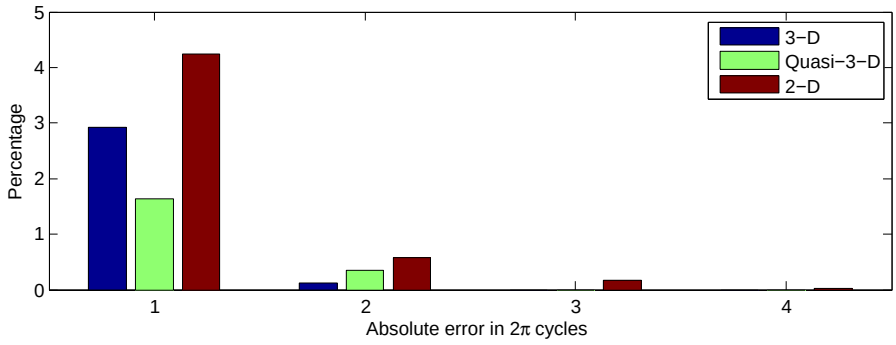

Figure 5-11: Comparison of unwrapping accuracy for the simulated data for the three different algorithms.

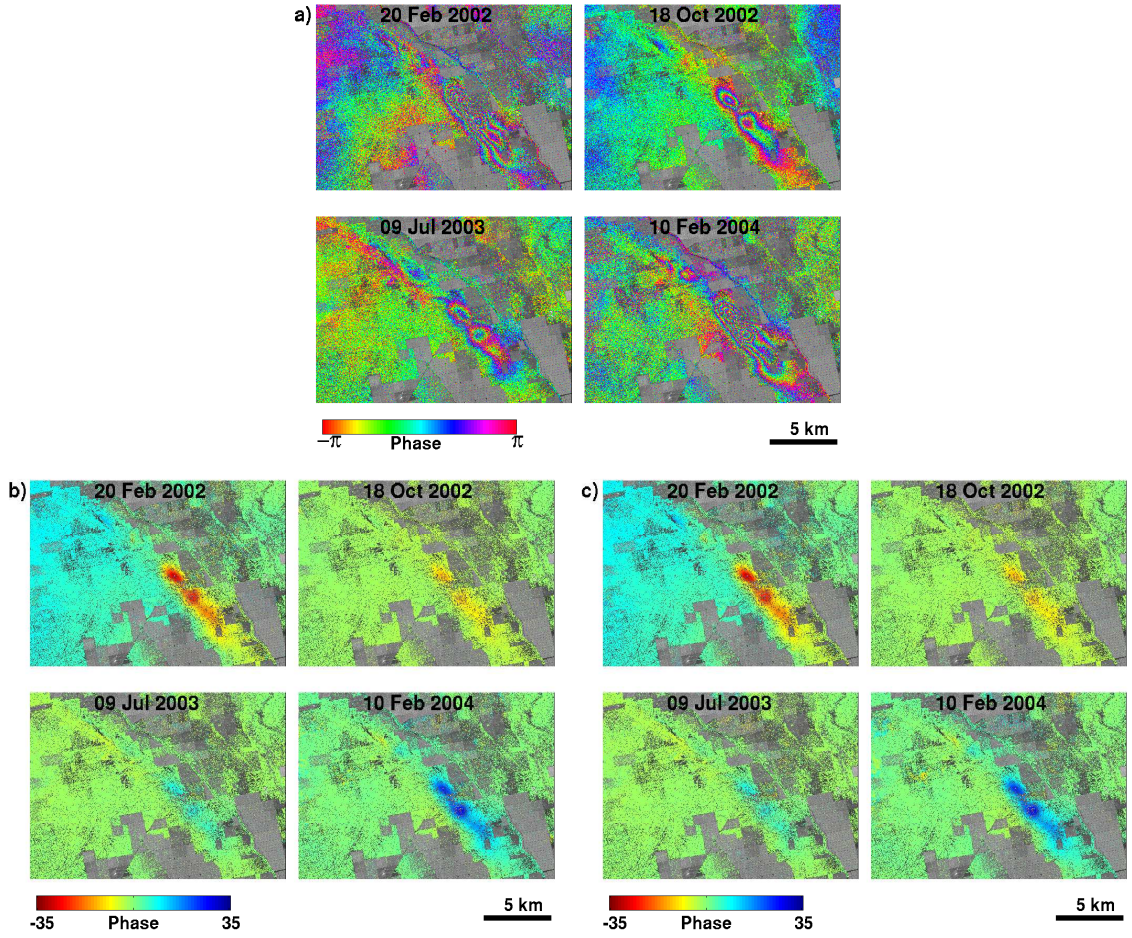

Figure 5-12: Lost Hills region persistent scatterer interferograms, (a) wrapped phase, (b) phase unwrapped using the quasi-L^∞ 3-D algorithm and (c) phase unwrapped using the pseudo-3-D algorithm. The date of the master acquisition is 22 Feb 2003 and only every 9th interferogram is shown. The background image in gray is the mean SAR amplitude of all 28 passes and the points represent the persistent scatters, with the color indicating the relative phase difference with respect to the northeast corner.

5.5.2 Lost Hills InSAR Persistent Scatterer Example

We now present 3-D phase unwrapping of two real data sets. The first was acquired over Lost Hills oil field in California. We processed 28 interferograms formed from 29 RADARSAT-1 F1 fine mode scenes acquired every 24 days between February 20th, 2002 and February 10th, 2004. We formed all interferograms with respect to the same "master" scene acquired on March 11th, 2003. This is an actively subsiding area due

to oil extraction. We used the method described in Chapter 4 to identify persistent scatterers and estimate and remove the look angle error terms, including those due to errors in the digital elevation model. We pre-filtered the data as described in Section 5.3.7 and unwrapped the phase using both the 3-D and pseudo-3-D algorithms. The results are shown in Figure 5-12. Despite the difference in approach, the results are identical for 99% of the unwrapped phase values and no systematic differences are evident, indicating that both algorithms appear feasible for this case.

5.5.3 Long Valley InSAR Persistent Scatterer Example

We also applied the two algorithms to data acquired Long Valley caldera in California. We processed 21 interferograms formed from 22 ERS-1/ERS-2 scenes acquired between 4th June 1992 and August 20th, 2000. All interferograms were formed with respect to the same "master" scene acquired on June 22nd, 1997. Within the caldera is a resurgent dome which is known to have both inflated and deflated during this period. We used the method described in Chapter 4 to identify persistent scatterers and estimate and remove the look angle error terms. We pre-filtered the data and unwrapped the phase using the pseudo-3-D unwrapping algorithm. The results are shown in Figure 5-13.

The quasi-L^∞ 3-D algorithm does not work well in this region, producing discontinuities in the unwrapped phase where none are expected. We expect this algorithm to be accurate only when the sampling is such that no multiple-loop discontinuities are present. Presumably, for these data, this is not the case. There is, however, ground truth for validation of our results. We compared relative vertical motion calculated from the unwrapped phase to that measured by leveling and GPS, and inferred from electronic distance meter (EDM) measurements. The results are shown in Figure 5-14. Horizontal motion measured by the EDM line between CASA and KRAK is almost parallel to the satellite track and hence not present in our interferograms. However, this horizontal motion is almost proportional to the vertical motion of the resurgent dome [*Battaglia et al.*, 2003] and, once scaled using less frequent leveling and GPS measurements, provides a proxy for relative vertical motion. We estimated

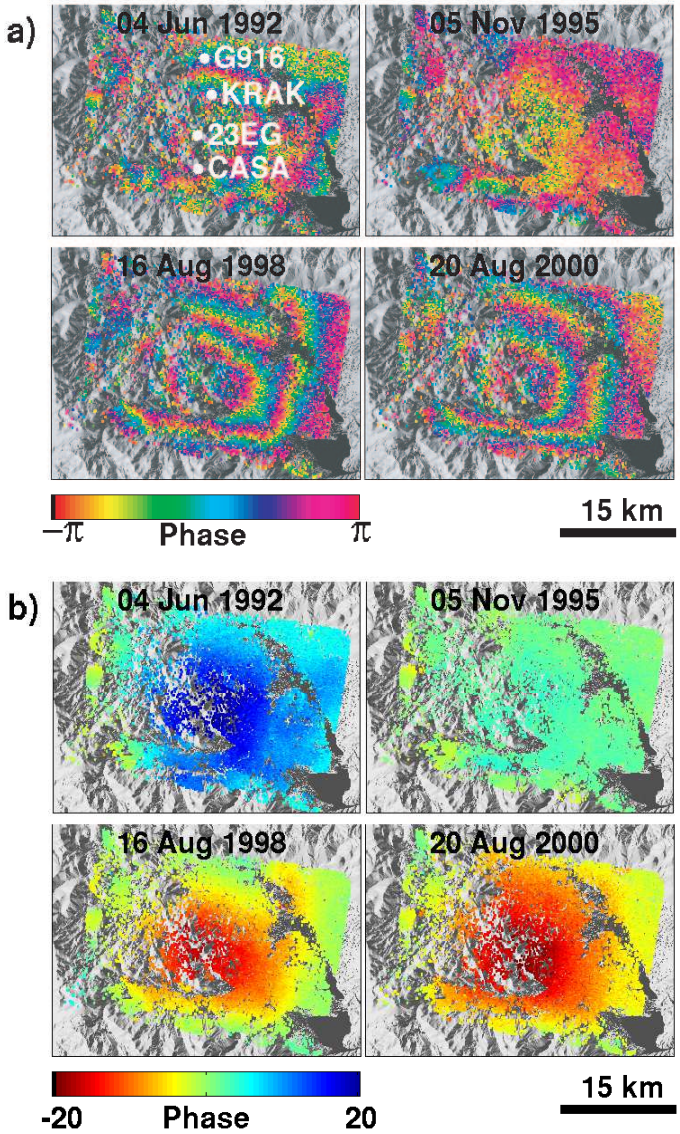

Figure 5-13: Long Valley persistent scatterer interferograms, (a) wrapped phase and (b) phase unwrapped using the pseudo-3-D algorithm. The date of the master acquisition is 22 Jun 1997 and only every 7th interferogram is shown. The background image in gray is the topography in shaded relief and the points represent the persistent scatters with the color indicating the relative phase difference with respect to the northwest corner.

the phase at each benchmark as the mean phase of all persistent scatters within 500 m and the error bars show the standard deviation of these phases. In (a) we converted the phase values to relative vertical displacement by assuming that all the motion

contributing to the change in phase was due to vertical motion only. In (b) we relaxed that assumption and solved for a component of horizontal displacement that is proportional to the vertical component. We found the constant of proportionality through a least-squares inversion that minimized the difference between the vertical displacement and the scaled EDM measurements. Our results indicate that the unwrapping between the two benchmarks was reliable. In Chapter 3, we unwrapped PS time series over Long Valley using a 2-D algorithm and also found the unwrapping between the two benchmarks to be reasonable. However, the overall pattern of the displacements found in that case, especially on the west side of the caldera where there appears to be a discontinuity, differs to that seen by *Fialko et al.* [2001]. The overall pattern using the pseudo-3-D algorithm, however, matches well.

5.6 Conclusions

We framed the problem of 3-D unwrapping in terms of an optimization problem, and developed an algorithm to find the L^∞-norm solution. For a subset of cases, those with no multiple-cycle phase discontinuities and no 2-D closed-loop discontinuities, the L^∞-norm solution is identical to the L^0-norm solution which we expect to be the best solution within this optimization framework. We demonstrated the accuracy of the algorithm on simulated and real data sets. We also developed a pseudo-3-D algorithm that is ad hoc, and relies on first unwrapping in 1-D, then iteratively improving this solution in the other two dimensions. This algorithm may be applicable in the general case, although we would not expect it to be as accurate as the fully 3-D algorithm in certain cases. We demonstrated the accuracy of this algorithm on simulated and real data sets also.

The next step is to develop an efficient algorithm to find the L^0 solution to the general case, allowing application of the fully 3-D approach in all cases. A further improvement still would be to formulate the optimization in terms of generalized, nonlinear cost functions, as done in two dimensions by *Chen and Zebker* [2000].

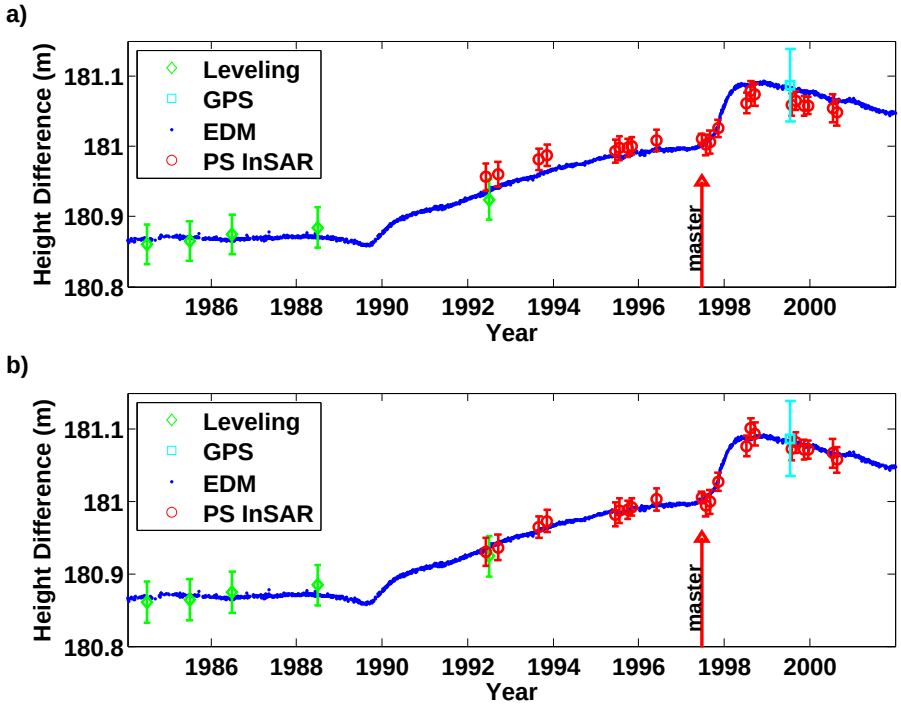

Figure 5-14: Comparison of relative vertical motion between benchmarks 23EG and G916 (see Figure 5-13 for locations) from leveling and GPS to that calculated from the unwrapped persistent scatterer phase, (a) assuming phase changes are due to vertical displacement only and (b) assuming there is also a horizontal component of displacement proportional to the vertical. The error bars represent 68% confidence bounds. Also shown is the scaled line length change between CASA and KRAK as measured by EDM, which is a proxy for vertical deformation.

Chapter 6

Reconciling seismic and geodetic models of the 1989 Kilauea south flank earthquake

This earthquake predates the acquisition of SAR data over Kilauea, hence we cannot use InSAR to help constrain the deformation and the persistent scatterer method is not applicable. We are, however, able to estimate the deformation field from other geodetic measurements that were made.

The inconsistency between the hypocentral depth, as determined by seismic models, and the fault depth, as determined by geodetic models, of the 1989 Kilauea earthquake has long been puzzling. Previous attempts to incorporate elastic heterogeneity in geodetic models of the 1989 earthquake have increased the fault depth substantially, bringing it closer to the hypocentral depth. However, recent studies on earthquakes elsewhere, that have included heterogeneity, indicate that the effect on fault depth of including heterogeneity for the 1989 earthquake should not be so great and, indeed, we show here that the effect is actually relatively minor. However, by combining three different sets of geodetic data, we are able to get a more accurate estimate of the fault depth, which does in fact coincide with the hypocentral depth at the 95% confidence level. When we take into consideration that static elastic parameter values are commonly lower than dynamic values, the agreement is even better. Furthermore, the fault depth is consistent with the earthquake having occurred at

the interface between the volcanic pile and the pre-volcanic seafloor.

6.1 Introduction

At 0327 UTC on June 26th, 1989 a magnitude M6.1 earthquake struck the south flank of Kilauea Volcano on the island of Hawaii. The hypocentral depth was determined from short-period seismic data to be at 9.2 ± 2.0 km [*Bryan*, 1992], and from teleseismic data to be at 13 km [*Chen and Nábělek*, 1990]. However, estimates from geodetic data using a homogeneous Earth model gave a sub-horizontal fault at an average depth of 4 ± 1 km [*Arnadottir et al.*, 1991] and 6 ± 2 km [*Dvorak et al.*, 1994] (see Table 6.1). *Arnadottir et al.* [1991] determined that adding elastic heterogeneity to the model would deepen the fault and, adopting this approach, *Du et al.* [1997] concluded that the depth of the fault could be as deep as 7 ± 0.5 km. However, the results of other recent studies suggest that heterogeneity is unlikely to have so large an effect [e.g., *Cattin et al.*, 1999; *Johnson et al.*, 2001; *Cervelli et al.*, 2002]. In this chapter, we firstly re-evaluate the model of *Du et al.* [1997], and then introduce a more realistic model of elastic heterogeneity. In an attempt to reconcile seismic and geodetic models we also use all the geodetic data available to us, including electronic distance meter (EDM) data that have not been used in any published modeling of the earthquake.

Knowing the actual depth of the earthquake is important in our understanding of the mechanics of Kilauea. The south flank of Kilauea is moving south-southeast relative to the Pacific Plate by about 8 cm/yr [*Owen et al.*, 2000]. Many authors believe that this movement is accommodated by sliding along a basal decollement at the interface of the volcanic pile and the pre-volcanic sea floor [e.g., *Nakamura*, 1980; *Dieterich*, 1988; *Thurber and Gripp*, 1988; *Delaney et al.*, 1993; *Owen et al.*, 2000] at a depth of about 7 to 8 km. However, *Cervelli et al.* [2002] suggested that some slip, at least, does occur at a shallower depth.

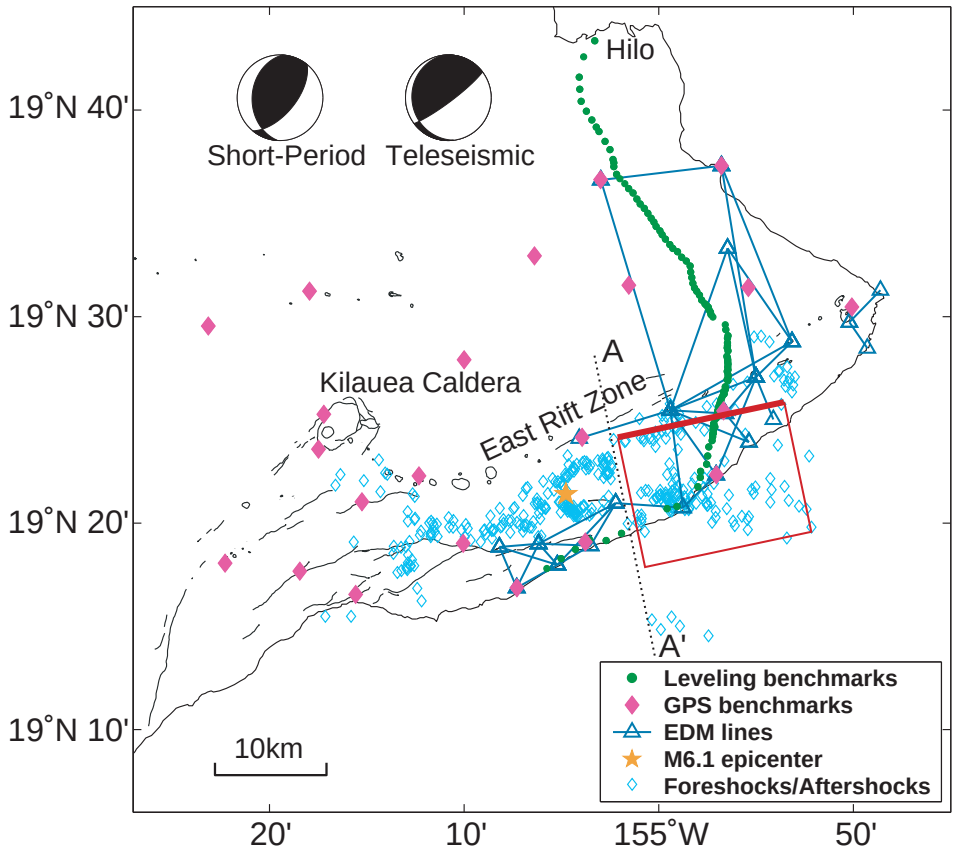

Figure 6-1: Map of southeastern Hawaii, showing geodetic benchmarks and earthquake epicenters for June and July 1989. The focal mechanism is given for the main shock, as calculated from short-period data [*Bryan*, 1992] and teleseismic data [*Chen and Nábělek*, 1990]. The rectangle shows the surface projection of the best-fitting fault plane solution, using all the available geodetic data and assuming layered heterogeneity in elastic parameters, as in Figure 6-3b. The thicker line represents the up-dip end.

6.2 Hypocenter Relocation

We used the double-difference travel-time method of *Waldhauser and Ellsworth* [2000] to obtain more accurate locations for all the earthquakes within the eastern rift zone during the months of June and July of 1989 (see Figures 6-1 and 6-2). The velocity model consisted of 5 horizontal layers with the average velocity of each layer derived from *Okubo et al.* [1997]. Using this approach the uncertainty in the locations of the events was reduced by 84% relative to undifferenced locations.

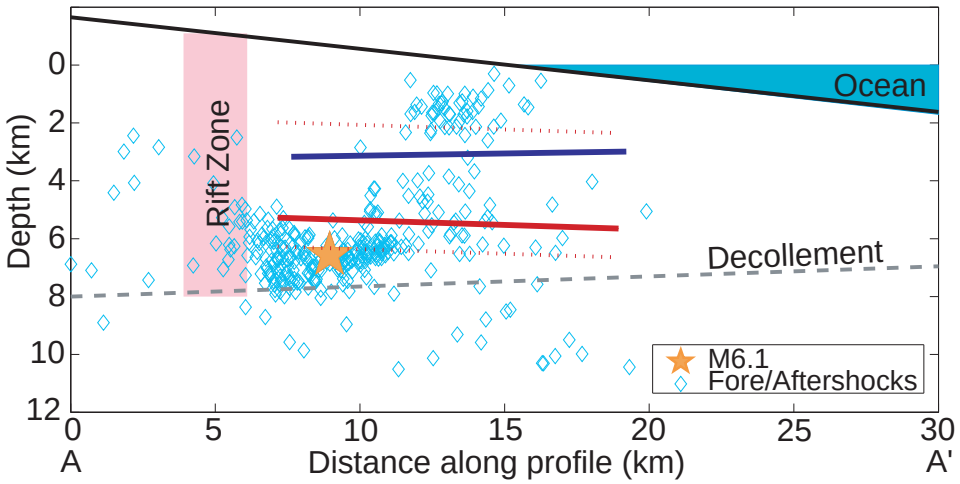

Figure 6-2: Earthquake hypocenters for June and July 1989 projected on to line A-A0 in Figure 6-1. The blue subhorizontal line is the projection of the best-fitting fault plane solution using leveling data only and modeled in a homogeneous halfspace as per *Arnadottir et al.* [1991]. The dark line represents the best-fitting solution using all the geodetic data and assuming layered heterogeneity, as in Figure 6-3 (b). The dotted lines represent the 95% confidence bounds for this solution (derived from the 95% confidence bounds for the solution using all the data modeled in a homogeneous halfspace).

6.3 Du et al., [1997] Model of Heterogeneity

Du et al. [1997] used leveling data collected in early 1988 and after the earthquake in 1989 (see Figure 6-1 for benchmark locations) to solve for the best-fitting fault geometry, using a moduli perturbation method to include the lateral and vertical heterogeneity in elastic properties, as shown in Figure 6-3 (a). We essentially repeated this inversion, using the same leveling data and the same model of heterogeneity. We set up the problem to solve for the change with time in the height difference between each pair of leveling benchmarks. This is equivalent to solving for the change with time in the height of each benchmark, but has the advantage of making each data point independent and the covariance matrix is therefore purely diagonal. The standard error of each measurement was assumed to be 2.83 mm $km^{-1/2}$ as per *Arnadottir et al.* [1991]. Using the *Arnadottir et al.* [1991]homogeneous optimal model as our prior, we solved for 9 model parameters (length, width, depth, strike, dip, longitude, latitude, along-strike slip and down-dip slip) using the trust-region reflective Newton

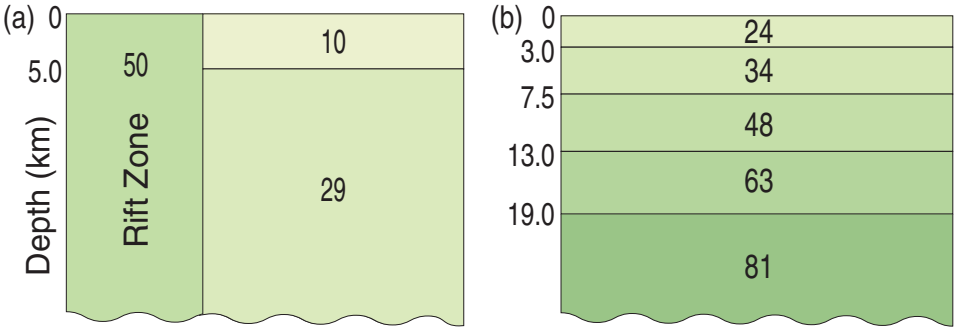

Figure 6-3: Models of shear modulus heterogeneity in GPa.
(a) After *Du et al.* [1997]. (b) Derived from seismic P-wave velocities from *Okubo et al.* [1997].

nonlinear algorithm [*Coleman and Li*, 1994].

We ran the inversion twice, once including the heterogeneity, and once without for comparison. In the homogeneous case, our result differed slightly from that of *Arnadottir et al.* [1991], giving the average depth of the best-fitting fault plane to be at 3.5 km. In the heterogeneous case, the average depth increased by only 0.8 km to 4.3 km (model (a), Table 6.2). This is significantly different to the result of *Du et al.* [1997], whose best-fitting fault plane lay at 7.0 km. The minimum in the misfit with depth curve is not sharply defined in the homogeneous case and the introduction of a change in elastic properties at approximately the same depth as the fault adds numerical noise to the curve. Combined with the fact that computing efficiency restrictions at that time only allowed for one Newton step, makes it likely that the *Du et al.* [1997] solution is in fact a local minimum.

Model	*Arnadottir et al.* [1991]	*Dvorak et al.* [1994]	*Du et al.* [1997]
Elastic Properties	Homogeneous halfspace	Homogeneous halfspace	Lateral and vertical heterogeneity
Data Used	Leveling	GPS	Leveling
Depth (km)	4 ± 1	6 ± 2	7 ± 0.5

Table 6.1: Properties of earlier geodetic models.

Table 6.2: Properties of new geodetic models.

Model	(a)	(b)	(c)
Elastic Properties	Lateral and vertical heterogeneity[1]	Vertical heterogeneity	Vertical heterogeneity (top layer varies)
Data Used	Leveling	All	All
Heterogeneity Method	Perturbation	Propagator Matrix	Propagator Matrix
Depth (km)	4.3	6.0	7.4
Misfitb[2] (mm)	2.7	3.8	3.8

[1]Du et al., [1997] model of heterogeneity.
[2]The weighted root mean square (rms) misfit [*Segall and Harris*, 1986].

6.4 Extra Geodetic Data

The leveling data provide only the vertical gradient along one line, which is not enough to constrain the fault geometry well on its own. We therefore added the following data to our subsequent inversions:

6.4.1 GPS Data

GPS surveys were carried out by HVO in August of 1988 and 1989 (see Figure 6-1 for benchmark locations) and we used the displacement solutions from *Dvorak et al.* [1994]. The covariance matrix was not available, so we scaled the NS and EW variances by the repeatability values given in *Dvorak et al.* [1994] and used these to construct a diagonal covariance matrix. We assumed that secular displacement was constant over this period and removed it using the model of *Owen et al.* [2000], which we also used to remove secular displacement from the leveling data.

Hawaii lies outside the network of GPS-tracking stations in North America that were used to compute satellite orbits at this time. Additionally a key satellite was missing for much of both the 1988 and 1989 surveys, which meant that 4 satellites could only be tracked simultaneously for 20 minutes per observing session. For these reasons, the uncertainties are very high (see Figure 6-4) and therefore the GPS data contribute little to our geodetic fault solutions. However, the general pattern of

displacement is useful in ruling out some solutions.

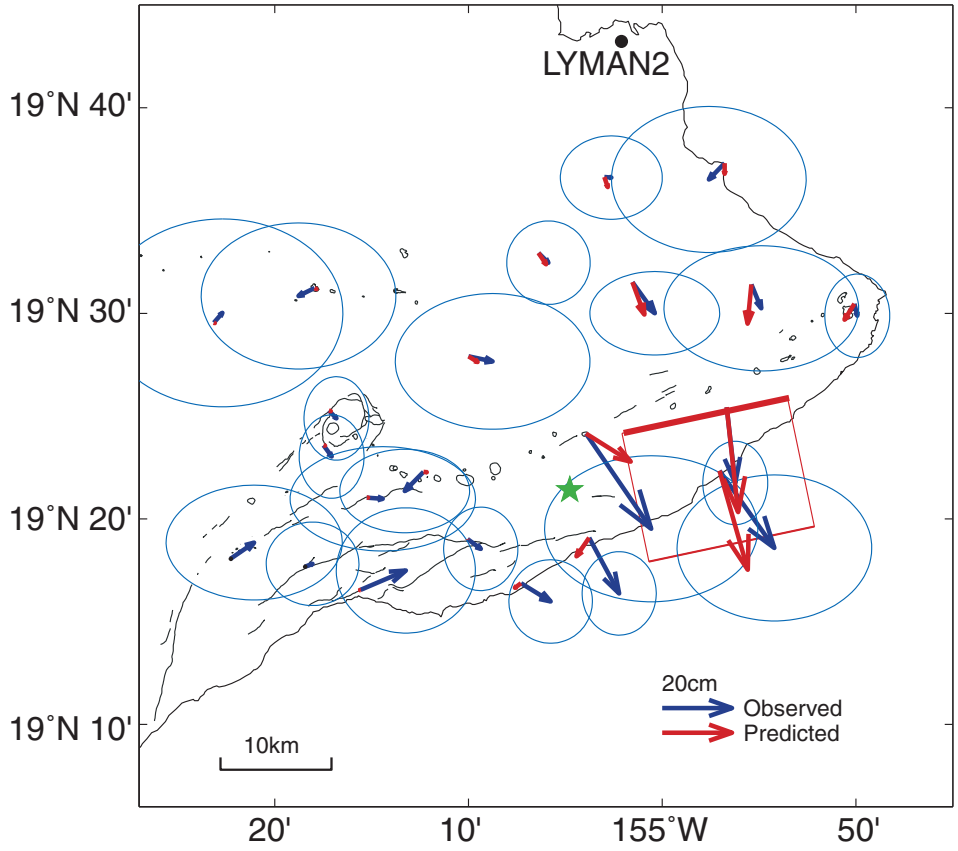

Figure 6-4: Predicted and observed GPS benchmark displacements relative to LYMAN2, with 95% confidence ellipses. The predicted values are for the best-fitting solution using all the available geodetic data and assuming layered heterogeneity in elastic parameters, as in Figure 6-3 (b). The surface projection of the fault solution is also shown, with the thicker line representing the up-dip end.

6.4.2 EDM Data

We used EDM data that were collected by HVO on and around Kilauea from 1970 to 1995. To avoid deformation associated with the caldera biasing our results, we only included lines that were wholly east of longitude 155° west. We further discarded lines that did not span the 1989 earthquake and those surveyed less than 8 times, to allow reasonable error estimation (see Figure 6-1 for the lines used). For each line

we assumed a constant secular rate of change in line length over the entire period, with offsets at known events. We inverted for this rate of change and the offsets, and used a bootstrap percentile method [*Efron and Tibshirani*, 1986] to estimate the 95% confidence limits and standard error of the offset at the 1989 event for each line. Errors for each line were assumed to be uncorrelated and our covariance matrix was therefore simply a diagonal matrix of variances.

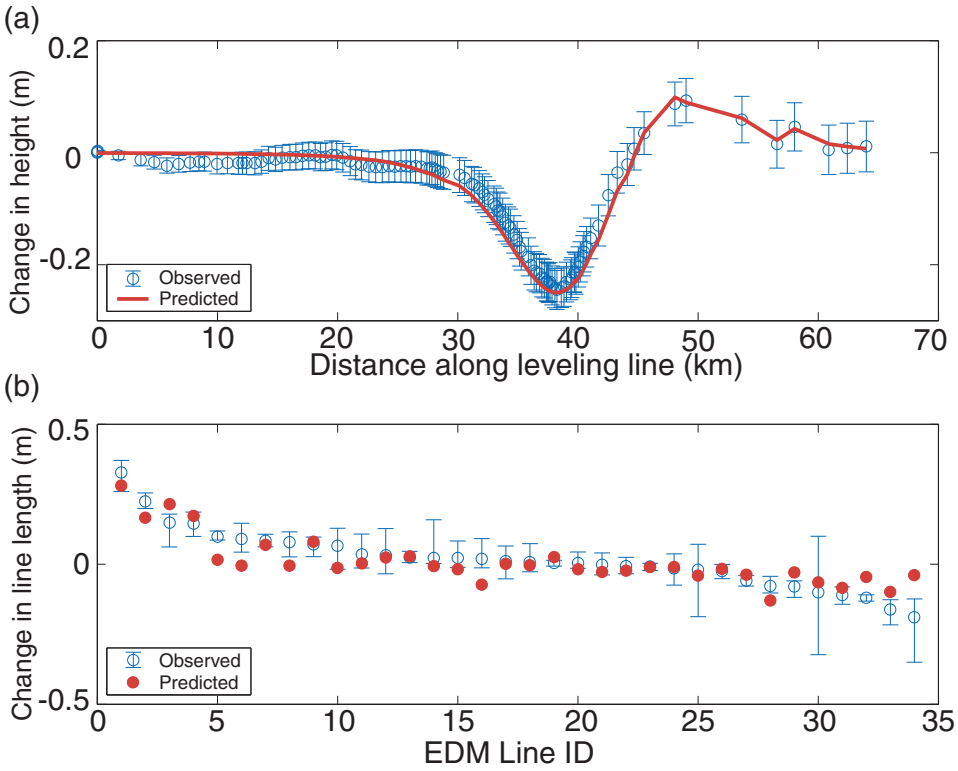

Figure 6-5: Predicted and observed values of (a) leveling and (b) EDM data. The predicted values are for the best-fitting solution using all the available geodetic data and assuming layered heterogeneity, as in Figure 6-3b. In (a), distances along the line are from the Hilo tide gauge. In (b) the EDM lines are numbered in order of decreasing line length change.

6.5 Layered Heterogeneity

The P-wave velocity distribution derived by *Okubo et al.* [1997] from a tomographic inversion suggests that the model of heterogeneity used by *Du et al.* [1997] overemphasizes the difference in elastic parameters between the rift zone and the adjacent crust. In fact, the lateral variation in velocity appears to be 2nd order when compared to the vertical variation. We therefore ignored lateral contrasts and divided the crust into 5 horizontal layers of constant shear modulus derived from the average velocity of each layer (see Figure 6-3b), assuming the crust to be a Poisson solid (in fact *Cattin et al.* [1999] demonstrated that varying Poisson's ratio does not significantly alter the model depth).

We included the heterogeneity using a propagator matrix method [*Ward*, 1985; *Johnson et al.*, 2001] and, combining the leveling, GPS and EDM data, we solved for the 9 model parameters using the Nelder-Mead simplex non-linear algorithm [*Nelder and Mead*, 1965] (the more efficient trust-region reflective Newton tended to converge on local minima). We approximated the 1st order effect of topography by fitting a plane to the surface of Kilauea and rotating our model and solution into this plane.

The best-fitting solution (model (b), Table 6.2) is a sub-horizontal fault with an average depth of 6.0 km below the surface, striking 078° and dipping 2° SSE (see Figures 1 and 2). The slip on the fault has a 1.4 m normal dip-slip component and a 0.09 m left-lateral strike-slip component.

The fit to the data is shown in Figures 6-4 and 6-5. Some of the EDM data points are not fit at the 95% confidence level and this may be partly because these measurements include a certain amount of inelastic deformation. Surface ground cracks around Kalapana [*Arnadottir et al.*, 1991] indicate that inelastic deformation did occur. The weighted root mean square misfit [*Segall and Harris*, 1986] is 3.8 mm as compared to 2.7 mm for the *Du et al.* [1997] model of heterogeneity using leveling data only, but the addition of the EDM and GPS data also increases the measurement uncertainty (average standard error of the data increases from 1.2 mm to 1.6 mm).

Using a bootstrap percentile method with 1000 iterations we constrained the 95% confidence bounds on the average depth when modeled in a homogeneous halfspace. If

we assume that the model variance of the heterogeneous model is reasonably approximated by the variance of the homogeneous model, we can apply the same confidence range to the heterogeneous model. This gives 95% confidence bounds of 3.2 and 7.5 km and the hypocentral depth lies within this interval.

We note that the epicenter does not lie within the surface projection of our best-fitting fault plane (see Figure 6-1). This is likely an artifact of modeling the fault with uniform slip, which forces the slip to go to zero discontinuously. When we solved for the fault geometry in a homogeneous halfspace assuming distributed-slip, the slip went to zero gradually over a larger projected area, which included the epicenter.

The strike and dip of our geodetic model is inconsistent with the focal mechanism determined from short-period seismic data [*Bryan*, 1992], but is consistent with that determined from long-period data [*Chen and Nábělek*, 1990] (see Figure 6-1). The total moment of our model is 7.7 10^{18} Nm which is in reasonable agreement with the double-couple moment of 5.2 10^{18} Nm estimated from the CMT solution [National Earthquake Information Center, 1989].

6.6 Static and Dynamic Elastic Parameters

Static elastic parameter values are commonly less than dynamic values [*Simmons and Brace*, 1965; *King*, 1970; *Cheng and Johnston*, 1981]. This is thought to be due to differences in both strain amplitude and frequency. For rocks containing cracks, the effect is more pronounced at lower pressures, i.e. closer to the surface [*Jizba*, 1991]. The upper few km of Hawaiian crust likely contains many fractures and so would probably behave less stiffly in response to static displacement on a fault than would be predicted from the elastic parameters determined at seismic frequencies.

To see how large this difference in elastic parameters would need to be to explain the difference in depth between our best-fitting fault plane and the hypocenter, we performed another inversion. This time we fixed the depth of the fault plane to be at our best estimate of the hypocentral depth (7.4 km) and allowed the shear modulus and depth of the upper layer to vary, as well as the other 8 fault parameters (model (c). Table 6.2). Our optimal solution is a 2.7 km thick layer with a shear modulus of

4.5 GPa, which is a factor of 5 lower than the value derived from the P-wave velocity. There is no laboratory data available for fractured basalts to compare this ratio to, but it lies at the upper end of the range determined for sandstones by *Jizba* [1991]. Considering that the sandstone samples did not contain any macroscopic fractures which would likely increase further the difference between static and dynamic values, a factor of 5 for Hawaiian crust certainly seems plausible.

6.7 Conclusions

Adding heterogeneity to the fault model does not have as great an influence on the depth as previously concluded by *Du et al.* [1997]. Depth is only increased by 0.7 to 0.8 km, depending on model of heterogeneity, as opposed to 3 km.

Including measurements of displacement in the horizontal does deepen the best-fitting solution considerably. When combined with the effects of heterogeneity, the geodetic model depth is indistinguishable at the 95% confidence level from the hypocentral depth determined from short-period seismicity. These depths permit that the fault plane does in fact coincide with the decollement at the interface between the volcanic pile and the pre-volcano seafloor.

If we assume that the fault plane actually lies at the hypocentral depth, we estimate that the upper 2.7 km behaves five times less stiffly in response to static displacement than in response to the passage of seismic waves.

Chapter 7

Summary

Conventional interferometric synthetic aperture radar (InSAR) has proven to be a very effective technique for measuring crustal deformation. However, almost any interferogram includes large areas where the signals decorrelate and no measurement is possible. Persistent scatterer (PS) InSAR overcomes the decorrelation problem by identifying resolution elements whose echo is dominated by a single scatterer in a series of interferograms. Existing PS methods have been very successful in analysis of urban areas, where stable angular structures produce efficient reflectors that dominate background scattering. However, man-made structures are absent from most of the Earth's surface. Furthermore, existing methods identify PS pixels based on the similarity of their phase history to an assumed model for how deformation varies with time, whereas characterizing the temporal pattern of deformation is commonly one of the aims of any deformation study.

We describe in this dissertation a new persistent scatterer method (StaMPS) that uses spatial correlation of interferogram phase to find PS pixels in all terrains, with or without buildings. Prior knowledge of temporal variations in the deformation rate is also not required. The first implementation, in Chapter 3, has two main limitations:

1. The step to estimate spatially correlated terms depends on the assumed length scale of the correlation, which is fixed. However, in most cases we expect this length scale to vary both in time and space.

2. Phase unwrapping is implemented as a series of two-dimensional (2-D) problems,

leading to artifacts in the unwrapped phase.

The first limitation is addressed in Chapter 4, where we describe a band-pass filtering method that adapts to any phase gradient present in the data itself. We also describe in detail the extra steps needed in forming interferograms suitable for StaMPS and some refinements to the method itself.

The second limitation of Chapter 3 is addressed in Chapter 5, where we frame the phase unwrapping problem as one in three dimensions. We develop two algorithms to solve the problem, the first being a true three-dimensional (3-D) algorithm and the second being a pseudo-3-D algorithm. The 3-D algorithm, being a quasi-L^∞-norm solution, is only applicable where there are no multiple-cycle phase discontinuities and no 2-D closed-loop discontinuities, in which case it gives the most accurate solution. For other cases, the pseudo-3-D algorithm that unwraps first in 1-D, then iteratively improves this solution in the other two dimensions, is applicable.

7.1 Future Directions

PS selection criteria in StaMPS are based on empirically derived probability distributions. While we demonstrate the effectiveness of this method, our expectation is that not all PS pixels are selected and that a small percentage of pixels that are selected contain no useful signal. The selection criteria could be improved upon by modeling the scattering characteristics of PS pixels. To do this, we need to better understand the physical characteristics of the ground that lead to pixels with good phase stability, particularly outside of urban areas.

Atmospheric signal is currently estimated by filtering only. As we know something about the statistics of atmospheric signal in terms of the power spectrum and the variability with surface elevation, we can improve the estimates by including a specific modeling step. In some cases the atmospheric signal can be estimated by other means, such as GPS, and these estimates can also be incorporated into StaMPS processing. As well as improving displacement estimates by reducing the error in the atmospheric term, this would reduce the aliasing in time caused by the undersampling of the atmospheric signal, leading to improved accuracy in phase unwrapping.

The next step in terms of 3-D phase unwrapping is to develop an efficient algorithm to find the L^0 solution for the general case, allowing application of the fully 3-D approach in all cases. A further improvement still would be to formulate the optimization in terms of generalized, nonlinear cost functions, as done in two dimensions by *Chen and Zebker* [2000].

The applicability of StaMPS in quantifying deformation due to volcanic processes is demonstrated in both Chapters 3 and 4. Also demonstrated is the ability to detect deformation due to landsliding (Chapter 4) and ground subsidence related to oil-extraction (Chapter 5). We believe that StaMPS is equally applicable in tectonic settings to detect coseismic, postseismic and interseismic deformation. Some modification may be required in the spatial filtering steps, however, for PS that are close to any surface rupture of associated faults.

Bibliography

Adam, N., B. Kampes, M. Eineder, J. Worawattanamateekul, and M. Kircher, The development of a scientific permanent scatterer system, *ISPRS Hannover Workshop Proceedings*, 2003.

Adam, N., B. Kampes, and M. Eineder, Development of a scientific permanent scatterer system: Modifications for mixed ERS/ENVISAT time series, *European Space Agency, (Special Publication) ESA SP*, (572), 457 – 465, 2005.

Amelung, F., S. Jónsson, H. Zebker, and P. Segall, Widespread uplift and 'trapdoor' faulting on Galapagos volcanoes observed with radar interferometry, *Nature*, *407*(6807), 993 – 996, 2000.

Arnadottir, T., P. Segall, and P. Delaney, A fault model for the 1989 Kilauea south flank earthquake from level and seismic data, *Geophysical Research Letters*, *18*(12), 2217 – 20, 1991.

Arnaud, A., J. Closa, R. Hanssen, N. Adam, M. Eineder, J. Inglada, G. Fitoussi, and B. Kampes, Development of algorithms for the exploitation of ERS-Envisat using the stable points network, *Tech. Rep. ESA Contract 16702/02/I-LG*, Altamira Information, Barcelona, Spain, 2004.

Arrigoni, M., C. Colesanti, A. Ferretti, D. Perissin, C. Prati, and F. Rocca, Identification of the location phase screen of ERS-ENVISAT permanent scatterers, *European Space Agency, (Special Publication) ESA SP*, (550), 181 – 186, 2004.

Bamler, R., Interferometric stereo radargrammetry: Absolute height determination

from ERS-ENVISAT interferograms, *International Geoscience and Remote Sensing Symposium (IGARSS)*, *2*, 742 – 745, 2000.

Bamler, R., and P. Hartl, Synthetic aperture radar interferometry., *Inverse Problems*, *14*(4), R1 – 54, 1998.

Bamler, R., N. Adam, G. W. Davidson, and D. Just, Noise-induced slope distortion in 2-d phase unwrapping by linear estimators with application to SAR interferometry, *IEEE Transactions on Geoscience and Remote Sensing*, *36*(3), 913 – 21, 1998.

Battaglia, M., P. Segall, J. Murray, P. Cervell, and J. Langbein, The mechanics of unrest at Long Valley caldera, California: 1. Modeling the geometry of the source using GPS, leveling and two-color EDM data, *J. Volcanol. Geotherm. Res.*, *127*(3-4), 195 – 217, 2003.

Berardino, P., G. Fornaro, R. Lanari, and E. Sansosti, A new algorithm for surface deformation monitoring based on small baseline differential SAR interferograms, *IEEE Transactions on Geoscience and Remote Sensing*, *40*(11), 2375 – 83, 2002.

Brakke, K., The surface evolver, *Experimental Mathematics*, *1*(2), 141 – 165, 1992.

Bryan, C. J., A possible triggering mechanism for large Hawaiian earthquakes derived from analysis of the 26 June 1989 Kilauea south flank sequence, *Bulletin of the Seismological Society of America*, *82*(6), 2368 – 90, 1992.

Cattin, R., P. Briole, H. Lyon-Caen, P. Bernard, and P. Pinettes, Effects of superficial layers on coseismic displacements for a dip-slip fault and geophysical implications, *Geophysical Journal International*, *137*(1), 149 – 58, 1999.

Cervelli, P., P. Segall, K. Johnson, M. Lisowski, and A. Miklius, Sudden aseismic fault slip on the south flank of Kilauea Volcano, *Nature*, *415*(6875), 1014 – 1018, 2002.

Chadwick, W. W., D. J. Geist, S. Jónsson, M. Poland, D. J. Johnson, and C. M. Meertens, A volcano bursting at the seams: Inflation, faulting, and eruption at Sierra Negra Volcano, Galápagos, *submitted to Geology*, 2006.

Chen, C. W., Statistical-cost network-flow approaches to two-dimensional phase unwrapping for radar interferometry, Ph.D. thesis, Stanford University, 2001.

Chen, C. W., and H. A. Zebker, Network approaches to two-dimensional phase unwrapping: intractability and two new algorithms, *Journal of the Optical Society of America A (Optics, Image Science and Vision)*, *17*(3), 401 – 14, 2000.

Chen, C. W., and H. A. Zebker, Two-dimensional phase unwrapping with use of statistical models for cost functions in nonlinear optimization, *Journal of the Optical Society of America A (Optics, Image Science and Vision)*, *18*(2), 338 – 51, 2001.

Chen, W., and J. Nábělek, Source parameters of the June 26, 1989 Hawaiian earthquake, *Eos Trans. AGU, Fall Meet. Suppl.*, *71*, 562, 1990.

Cheng, C. H., and D. H. Johnston, Dynamic and static moduli, *Geophysical Research Letters*, *8*(1), 39 – 42, 1981.

Coleman, T. F., and Y. Li, On the convergence of reflective Newton methods for large-scale nonlinear minimization subject to bounds, *Mathematical Programming*, *67*, 189, 1994.

Colesanti, C., A. Ferretti, F. Novali, C. Prati, and F. Rocca, SAR monitoring of progressive and seasonal ground deformation using the permanent scatterers technique, *IEEE Transactions on Geoscience and Remote Sensing*, *41*(7), 1685 – 701, 2003a.

Colesanti, C., A. Ferretti, C. Prati, and F. Rocca, Monitoring landslides and tectonic motions with the permanent scatterers technique, *Eng. Geol*, *68*(1-2), 3 – 14, 2003b.

Costantini, M., A novel phase unwrapping method based on network programming, *IEEE Transactions on Geoscience and Remote Sensing*, *36*(3), 813 – 21, 1998.

Costantini, M., and P. A. Rosen, Generalized phase unwrapping approach for sparse data, *International Geoscience and Remote Sensing Symposium (IGARSS)*, *1*, 267 – 269, 1999.

Crosetto, M., A. Arnaud, J. Duro, E. Biescas, and M. Agudo, Deformation monitoring using remotely sensed radar interferometric data, *Proc., 11th FIG Symposium on Deformation Measurements, Santorini*, 2003.

Cusack, R., and N. Papadakis, New robust 3D phase unwrapping algorithm: Application to magnetic field mapping and undistorting echo-planar images, *NeuroImage*, *16*, 754 – 764, 2002.

Dehls, J. F., M. Basilico, and C. Colesanti, Ground deformation monitoring in the Ranafjord area of Norway by means of the permanent scatterers technique, *IEEE Int. Geosci and Remote Sensing Symposium. IGARSS 2002*, *1*, 203 – 207, 2002.

Delaney, P. T., A. Miklius, T. Árnadóttir, A. T. Okamura, and M. K. Sako, Motion of Kilauea volcano during sustained eruption from the Puu Oo and Kupaianaha vents, 1983-1991, *Journal of Geophysical Research*, *98*(B10), 17,801 – 20, 1993.

Dieterich, J. H., Growth and persistence of Hawaiian volcanic rift zones, *Journal of Geophysical Research*, *93*(B5), 4258 – 70, 1988.

Du, Y. J., P. Segall, and H. J. Gao, Quasi-static dislocations in three dimensional inhomogeneous media, *Geophysical Research Letters*, *24*(18), 2347 – 2350, 1997.

Dvorak, J., A. T. Okamura, M. Lisowski, W. H. Prescott, and J. L. Svarc, Global positioning system measurements on the island of Hawaii from 1987 to 1990, *U.S. Geol. Surv. Bull*, *2092*, 33, 1994.

Efron, B., and R. Tibshirani, Bootstrap methods for standard errors, confidence intervals, and other measures of sta- tistical accuracy, *Statistical Science*, *1*(1), 54 – 77, 1986.

Ferretti, A., C. Prati, and F. Rocca, Nonlinear subsidence rate estimation using permanent scatterers in differential SAR interferometry, *IEEE Trans. on Geosci. and Remote Sensing*, *38*(5), 2202 – 2212, 2000.

Ferretti, A., C. Prati, and F. Rocca, Permanent scatterers in SAR interferometry, *IEEE Trans. on Geosci. and Remote Sensing*, *39*(1), 8 – 20, 2001.

Ferretti, A., F. Novali, R. Bürgmann, G. Hilley, and C. Prati, InSAR permanent scatterer analysis reveals ups and downs in the San Francisco Bay Area, *Eos*, *85*(34), 317,324, 2004.

Fialko, Y., M. Simons, and Y. Khazan, Finite source modelling of magmatic unrest in Socorro, New Mexico, and Long Valley, california, *Geophys Journal International*, *146*(1), 191 – 200, 2001.

Gabriel, A. K., and R. M. Goldstein, Crossed orbit interferometry, *Dig Int Geosci Remote Sens Symp (IGARSS)*, *1*, 611 – 611, 1988.

Gabriel, A. K., R. M. Goldstein, and H. A. Zebker, Mapping small elevation changes over large areas: differential radar interferometry., *Journal of Geophysical Research*, *94*(B7), 9183 – 91, 1989.

Geist, D., K. A. Howard, A. M. Jellinek, and S. Rayder, The volcanic history of volcan-alcedo, Galapagos Archipelago - a case-study of rhyolitic oceanic volcanism, *Bulletin of Volcanology*, *56*(4), 243 – 260, 1994.

Ghiglia, D. C., and M. D. Pritt, *Two-dimensional phase unwrapping: Theory, Algorithms and Software*, Wiley, New York, 1998.

Ghiglia, D. C., and L. A. Romero, Minimum L^p-norm two-dimensional phase unwrapping, *Journal of the Optical Society of America A (Optics, Image Science and Vision)*, *13*(10), 1999 – 2013, 1996.

Goldstein, R. M., and C. L. Werner, Radar interferogram filtering for geophysical applications, *Geophysical Research Letters*, *25*(21), 4035 – 8, 1998.

Goldstein, R. M., and H. A. Zebker, Interferometric radar measurement of ocean surface currents., *Nature*, *328*(6132), 707 – 9, 1987.

Goldstein, R. M., H. A. Zebker, and C. L. Werner, Satellite radar interferometry: two-dimensional phase unwrapping, *Radio Science*, *23*(4), 713 – 20, 1988.

Green, J., Recent activity in Alcedo volcano, Isabela island, *Noticias de Galápagos*, (54), 11–13, 1994.

Hanssen, R. F., *Radar Interferometry Data Interpretation and Error Analysis*, 328 pp., Springer, 2001.

Hilley, G. E., R. Burgmann, A. Ferretti, F. Novali, and F. Rocca, Dynamics of slow-moving landslides from permanent scatterer analysis., *Science*, *304*(5679), 1952 – 5, 2004.

Hoffmann, J., The application of satellite radar interferometry to the study of land subsidence over developed aquifer systems, Ph.D. thesis, Stanford University, 2003.

Hoffmann, J., H. A. Zebker, D. L. Galloway, and F. Amelung, Seasonal subsidence and rebound in Las Vegas Valley, Nevada, observed by synthetic aperture radar interferometry, *Water Resources Research*, *37*(6), 1551 – 1566, 2001.

Hole, J. K., A. Hooper, G. Wadge, and N. F. Stevens, Measuring contemporary deformation in the Taupo volcanic zone, New Zealand, using SAR interferometry, *European Space Agency, (Special Publication) ESA SP*, 2006.

Hooper, A., P. Segall, K. Johnson, and J. Rubinstein, Reconciling seismic and geodetic models of the 1989 Kilauea south flank earthquake, *Geophysical Research Letters*, *29*(22), 2062 – 2062, doi:10.1029/2002GL016156, 2002.

Hooper, A., H. Zebker, P. Segall, and B. Kampes, A new method for measuring deformation on volcanoes and other natural terrains using InSAR persistent scatterers, *Geophysical Research Letters*, *31*(23), 5, doi:10.1029/2004GL021737, 2004.

Huntley, J. M., Three-dimensional noise-immune phase unwrapping algorithm, *Applied Optics*, *40*(23), 3901 – 8, 2001.

Jizba, D. L., Mechanical and acoustical properties of sandstones and shales, Ph.D. thesis, Stanford University, 1991.

Johanson, I., and R. Bürgmann, Using point measurements from InSAR to detect transient deformation, *Eos Trans. AGU, Fall Meet. Suppl.*, *82*(47), 266, 2001.

Johnson, K. M., P. Segall, and P. Cervelli, Analytical methods for including vertical and horizontal heterogeneity of elastic properties in dislocation models and applications to two coseismic GPS datasets, *Eos Trans. AGU, Fall Meet. Suppl.*, *82*, 296–297, 2001.

Jónsson, S., Modeling volcano and earthquake deformation from satellite radar interferometric observations, Ph.D. thesis, Stanford University, 2002.

Jónsson, S., H. Zebker, P. Segall, and F. Amelung, Fault slip distribution of the 1999 M_w 7.1 Hector Mine, California, earthquake, estimated from satellite radar and GPS measurements, *Bulletin of the Seismological Society of America*, *92*(4), 1377 – 89, 2002.

Kampes, B. M., Displacement parameter estimation using permanent scatterer interferometry, Ph.D. thesis, Delft University of Technology, 2005.

King, M. S., Static and dynamic elastic moduli of rocks under pressure, in *Rocks Mechanics - Theory and Practice, Proc. 11th Symp. Rock Mech., Univ. of Calif.*, edited by W. H. Somerton, 1970.

Li, F. K., and R. M. Goldstein, Studies of multibaseline spaceborne interferometric synthetic aperture radars, *IEEE Transactions on Geoscience and Remote Sensing*, *28*(1), 88 – 97, 1990.

Lyons, S., and D. Sandwell, Fault creep along the southern San Andreas from interferometric synthetic aperture radar, permanent scatterers, and stacking, *Journal of Geophysical Research*, *108*(B1), 2047 – 2070, 2003.

Massonnet, D., M. Rossi, C. Carmona, F. Adragna, G. Peltzer, K. Fiegl, and T. Rabaute, The displacement field of the Landers earthquake mapped by radar interferometry, *Nature*, *364*, 138 – 142, 1993.

Massonnet, D., P. Briole, and A. Arnaud, Etna monitored by spaceborne radar interferometry, *Nature*, *375*, 567 – 570, 1995.

Mogi, K., Relations between the eruptions of various volcanoes and the deformations of the ground surfaces around them, *Bull. Earthquake Res. Inst. Univ. Tokyo*, *36*, 111 – 123, 1958.

Mosegaard, K., and A. Tarantola, Monte Carlo sampling of solutions to inverse problems, *Journal of Geophysical Research*, *100*(B7), 12,431 – 47, 1995.

Nakamura, K., Why do long rift zones develop in Hawaiian volcanoes - a possible role of thick oceanic sediments (in Japanese), *Bull. Volcanol. Soc. Jpn*, *25*, 255 – 267, 1980.

Nelder, J. A., and R. Mead, Simplex method for function minimization, *Computer Journal*, *7*(4), 308 – 313, 1965.

Okubo, P. G., H. M. Benz, and B. A. Chouet, Imaging the crustal magma sources beneath Mauna Loa and Kilauea volcanoes, hawaii, *Geology*, *25*(10), 867 – 870, 1997.

Owen, S., P. Segall, M. Lisowski, A. Miklius, R. Denlinger, and M. Sako, Rapid deformation of Kilauea Volcano: Global positioning system measurements between 1990 and 1996, *Journal of Geophysical Research*, *105*(B8), 18,983 – 18,998, 2000.

Pritchard, M. E., and M. Simons, A satellite geodetic survey of large-scale deformation of volcanic centres in the central Andes, *Nature*, *418*(6894), 167 – 171, 2002.

Richman, D., Three dimensional azimuth-correcting mapping radar, *Tech. rep.*, USA: United Technologies Corporation, 1971.

Rodriguez, E., and J. M. Martin, Theory and design of interferometric synthetic aperture radars., *IEE Proceedings F (Radar and Signal Processing)*, *139*(2), 147 – 59, 1992.

Schmidt, D. A., and R. Bürgmann, Time-dependent land uplift and subsidence in the santa clara valley, california, from a large interferometric synthetic aperture radar data set, *Journal of Geophysical Research*, *108*(B9), ETG4 – 1, 2003.

Segall, P., and R. Harris, Slip deficit on the San Andreas Fault at Parkfield, California, as revealed by inversion of geodetic data, *Science*, *233*(4771), 1409 – 13, 1986.

Sigmundsson, F., H. Vadon, and D. Massonnet, Readjustment of the Krafla spreading segment to crustal rifting measured by satellite radar interferometry, *Geophysical Research Letters*, *24*(15), 1843 – 6, 1997.

Simmons, G., and W. F. Brace, Comparison of static and dynamic measurements of compressibility of rocks, *Journal of Geophysical Research*, *70*(22), 5649, 1965.

Teunissen, P. J. G., The least-squares ambiguity decorrelation adjustment: a method for fast GPS integer ambiguity estimation, *Journal of Geodesy*, *70*(1/2), 65 – 82, 1995.

Thurber, C. H., and A. E. Gripp, Flexure and seismicity beneath the south flank of Kilauea Volcano and tectonic implications, *Journal of Geophysical Research*, *93*(B5), 4271 – 8, 1988.

Waldhauser, F., and W. L. Ellsworth, A double-difference earthquake location algorithm: method and application to the northern Hayward fault, California, *Bulletin of the Seismological Society of America*, *90*(6), 1353 – 68, 2000.

Ward, S. N., Quasi-static propagator matrices: creep on strike-slip faults, *Tectonophysics*, *120*(1/2), 83 – 106, 1985.

Werner, C., U. Wegmüller, T. Strozzi, and A. Wiesmann, Interferometric point target analysis for deformation mapping, *Geosci. and Remote Sensing Symposium, IGARSS*, 2003.

Wicks, C. W., W. Thatcher, D. Dzurisin, and J. Svarc, Uplift, thermal unrest and magma intrusion at Yellowstone caldera, *Nature*, *440*(7080), 72 – 75, 2006.

Wright, T., E. Fielding, and B. Parsons, Triggered slip: observations of the 17 August 1999 Izmit (Turkey) earthquake using radar interferometry, *Geophysical Research Letters*, *28*(6), 1079 – 82, 2001.

Yang, X. M., P. M. Davis, and J. H. Dieterich, Deformation from inflation of a dipping finite prolate spheroid in an elastic half-space as a model for volcanic stressing, *Journal of Geophysical Research*, *93*(B5), 4249 – 4257, 1988.

Yun, S., P. Segall, and H. Zebker, Constraints on magma chamber geometry at Sierra Negra Volcano, Galapagos islands, based on InSAR observations, *Journal of Volcanology and Geothermal Research*, *150*(1-3), 232 – 243, 2006.

Zebker, H. A., and R. M. Goldstein, Topographic mapping from interferometric synthetic aperture radar observations., *Journal of Geophysical Research*, *91*(B5), 4993 – 9, 1986.

Zebker, H. A., and Y. P. Lu, Phase unwrapping algorithms for radar interferometry: residue-cut, least-squares, and synthesis algorithms, *Journal of the Optical Society of America A (Optics, Image Science and Vision)*, *15*(3), 586 – 98, 1998.

Zebker, H. A., and J. Villasenor, Decorrelation in interferometric radar echoes, *IEEE Transactions on Geoscience and Remote Sensing*, *30*(5), 950 – 9, 1992.

Zebker, H. A., P. A. Rosen, R. M. Goldstein, A. Gabriel, and C. L. Werner, On the derivation of coseismic displacement-fields using differential radar interferometry - the Landers earthquake, *Journal of Geophysical Research*, *99*(B10), 19,617 – 19,634, 1994.

Zisk, S. H., A new, Earth-based radar technique for the measurement of lunar topography., *Moon*, *4*(3/4), 296 – 306, 1972.